

1 **Formation of retinal direction-selective circuitry initiated by starburst**  
2 **amacrine cell homotypic contact**

3

4 Thomas A. Ray<sup>1,2</sup>, Suva Roy<sup>1</sup>, Christopher Kozlowski<sup>1,2</sup>, Jingjing Wang<sup>1,2</sup>, Jon Cafaro<sup>1</sup>, Samuel  
5 W. Hulbert<sup>1</sup>, Christopher V. Wright<sup>3</sup>, Greg D. Field<sup>1</sup>, and Jeremy N. Kay<sup>1,2</sup>

6

7 1) Department of Neurobiology; 2) Department of Ophthalmology, Duke University School of  
8 Medicine, Durham, NC 27710 USA

9

10 3) Department of Cell and Developmental Biology, Vanderbilt University School of Medicine,  
11 Nashville, TN 37232 USA

12

13 Correspondence to: Jeremy Kay (jeremy.kay@duke.edu)

14

15 **Keywords:** Neural development; retinal ganglion cell; bipolar cell; mouse; radial migration;  
16 Ptf1a; IPL.

17

18 **Impact statement:** Selective synapse formation in a retinal motion-sensitive circuit is  
19 orchestrated by starburst amacrine cells, which use homotypic interactions to initiate formation  
20 of a dendritic scaffold that recruits projections from circuit partners.

**21 SUMMARY**

22 A common strategy by which developing neurons locate their synaptic partners is through  
23 projections to circuit-specific neuropil sublayers. Once established, sublayers serve as a substrate  
24 for selective synapse formation, but how sublayers arise during neurodevelopment remains  
25 unknown. Here we identify the earliest events that initiate formation of the direction-selective  
26 circuit in the inner plexiform layer of mouse retina. We demonstrate that radially-migrating  
27 newborn starburst amacrine cells establish homotypic contacts on arrival at the inner retina.  
28 These contacts, mediated by the cell-surface protein MEGF10, trigger neuropil innervation  
29 resulting in generation of two sublayers comprising starburst-cell dendrites. This dendritic  
30 scaffold then recruits projections from circuit partners. Abolishing MEGF10-mediated contacts  
31 profoundly delays and ultimately disrupts sublayer formation, leading to broader direction tuning  
32 and weaker direction-selectivity in retinal ganglion cells. Our findings reveal a mechanism by  
33 which differentiating neurons transition from migratory to mature morphology, and highlight this  
34 mechanism's importance in forming circuit-specific sublayers.

## 35 INTRODUCTION

36 In the developing nervous system, neurons form selective synapses to generate circuits  
37 comprised of cell-type-specific connections. This selectivity is important for circuit function  
38 because it ensures connectivity between neurons specialized for particular information-  
39 processing tasks. Despite its importance, basic questions about selective synapse formation  
40 remain unanswered. For example, we do not know how cell types fated to form synapses  
41 coordinate their growth to establish contact with each other. This is a significant cell biological  
42 challenge, because the neurons that comprise a single circuit are often born at disparate times and  
43 physical locations.

44 In many tissues, notably the insect and vertebrate visual systems, synaptic specificity is  
45 facilitated by laminar specificity, the phenomenon whereby circuit partners project their axons  
46 and dendrites to narrow strata within a laminated neuropil (Sanes and Zipursky, 2010). The inner  
47 plexiform layer (IPL) of the vertebrate retina comprises at least 10 distinct sublayers built from  
48 the axons and dendrites of different amacrine, bipolar, and retinal ganglion cell (RGC) types  
49 (Baier, 2013). By projecting to the same IPL sublayer, circuit partners can be assured of  
50 encountering each other. The developmental events that create sublayers and guide circuit  
51 partners to converge upon them are therefore essential for establishment of retinal circuitry. At  
52 later developmental stages, when rudimentary IPL sublayers have already formed, neurons rely  
53 on molecular cues localized to those sublayers for guidance to the appropriate IPL strata (Duan  
54 et al., 2014; Matsuoka et al., 2011; Sun et al., 2013; Yamagata and Sanes, 2008; Visser et al.,  
55 2015). However, a crucial question remains unresolved: How do sublayers form in the first  
56 place? Understanding the mechanisms that initiate creation of sublayers will provide significant  
57 insight into the earliest step in circuit formation.

58           To learn how members of a single circuit create layers and converge upon them to  
59 achieve synapse specificity, we studied the direction-selective (DS) circuit of mouse retina (Fig.  
60 1A). This circuit reports the direction of image motion to the brain through the spiking activity of  
61 distinct DS ganglion cell (DSGC) types that are tuned to prefer stimuli moving in particular  
62 directions (Demb, 2007; Vaney et al., 2012). The DS circuit comprises a limited number of well-  
63 described cell types amenable to genetic marking and manipulation (Kay et al., 2011; Huberman  
64 et al., 2009; Duan et al., 2014): 1) DSGCs; 2) GABAergic/cholinergic interneurons called  
65 starburst amacrine cells (SACs); and 3) four subtypes of glutamatergic bipolar cells (Chen et al.,  
66 2014; Duan et al., 2014; Greene et al., 2016; Kim et al., 2014). These DS-circuit cell types  
67 project to two IPL sublayers, ON and OFF, named for the light response profiles of the neurons  
68 that project to them. ON-OFF DSGCs (ooDSGCs) send dendrites to both sublayers, while SACs  
69 and bipolar cells project to one or the other, depending on their subtype (Fig. 1A). Several  
70 molecular perturbations have been described that influence ON vs. OFF laminar targeting in the  
71 mouse DS circuit (Sun et al., 2013; Duan et al., 2014), but in these cases IPL sublayers still form  
72 in the right place; errors are limited to choosing the wrong DS sublayer. Thus, neither the  
73 establishment of the DS circuit sublayers nor their positioning in the appropriate IPL region  
74 depends on molecules that have been studied to date.

75           Here we seek to understand the earliest events leading to formation of the DS circuit IPL  
76 sublayers. Two lines of evidence suggest that SACs may take the lead in assembling this circuit.  
77 First, SACs are among the first cells to stratify the IPL: Even though other neurons innervate it  
78 contemporaneously, SACs are precocious in restricting their arbors into sublayers (Stacy and  
79 Wong, 2003; Kay and Sanes, 2013). Second, in mutant mice that entirely lack RGCs or bipolar  
80 cells, SAC IPL projections are largely normal, indicating SACs can form sublayers in the

81 absence of their circuit partners (Moshiri et al., 2008; Green et al., 2003). Thus, we set out to test  
82 the hypothesis that SACs orchestrate assembly of the DS circuit sublayers. We find evidence  
83 supporting this hypothesis, and we identify a surprising cellular mechanism initiating SAC  
84 lamination: Rather than immediately innervating the IPL, newborn SACs first produce a  
85 transient homotypic arbor network outside the IPL. These early homotypic contacts serve as a  
86 cue promoting SAC dendrite development and circuit integration upon conclusion of their radial  
87 migration to the inner retina. When deprived of homotypic contacts, SAC IPL innervation – and  
88 consequent sublayer formation – is impaired. We identify the SAC cell-surface protein MEGF10  
89 as the molecular mediator of IPL innervation upon homotypic contact. In the absence of  
90 MEGF10, SACs persist in growing arbors outside the IPL, delaying IPL innervation. This in turn  
91 delays formation of the DS circuit sublayers and leads to SAC sublaminar targeting errors that  
92 persist to adulthood. We further show that impaired SAC sublayer formation has consequences  
93 for laminar targeting of their circuit partners: While partnering remains intact, lamination is  
94 disrupted, leading to spatial inhomogeneity in the DS circuit network. Finally, we show that  
95 these MEGF10-dependent anatomical changes both broaden and weaken direction tuning across  
96 the population of ooDSGCs. These results demonstrate that SACs orchestrate DS circuit  
97 assembly, first by initiating sublayer formation via homotypic contact, and then by using their  
98 laminated dendrites as a scaffold that guides projections of their circuit partners.

99

## 100 **RESULTS**

### 101 **Timing of DS circuit IPL sublayer formation**

102 To explore how the DS circuit creates its IPL sublayers, we began by determining when  
103 the sublayers first emerge in mouse. This analysis focused on SACs and ooDSGCs because

104 bipolar cells develop later (Morgan et al., 2006). Previous estimates of layer emergence vary  
105 widely (Stacy and Wong, 2003; Sun et al., 2013) due to the lack of adequate markers to study  
106 dendrite development in neonatal SACs. We therefore assembled a suite of mouse lines and  
107 antibody markers for this purpose, enabling anatomical studies of the full SAC population as  
108 well as individual cells (Fig. 1B-C; Fig. 1-Supplement 1; Fig. 2-Supplement 1). These markers  
109 revealed that SAC dendrites form two continuous well-defined laminae by P1 (Fig. 1B,E). Some  
110 dendrites were stratified already at P0, even though the P0 IPL neuropil is less than one cell  
111 diameter wide (Fig. 1B; Fig. 1-Supplement 1). Further supporting this timeline, individual P1  
112 SACs made lamina-specific projections (Fig. 1C): 96% of OFF SACs in the inner nuclear layer  
113 (INL), and 99% of ON SACs in the ganglion cell layer (GCL), stratified within the expected IPL  
114 sublayer ( $n = 49/51$  OFF;  $78/79$  ON; 4 mice). By contrast, ooDSGCs projected rudimentary and  
115 unstratified dendrites at P1 ( $n = 18$  cells, 3 mice, none were stratified; Fig. 1E; Fig. 1-  
116 Supplement 2; also see Peng et al., 2017). Even at P2, only 30% of ooDSGCs co-fasciculated  
117 with SAC arbors; the rest projected diffusely within the IPL ( $n = 23$  cells, 2 mice; Fig. 1D,E; Fig.  
118 1-Supplement 2). These results indicate that SACs form IPL sublayers at P0-P1, and are joined  
119 later by their synaptic partners.

## 120 **Early SAC projections target neighboring SAC somata**

121 To gain insight into how SACs form their sublayers, we next investigated the cell-cell  
122 interactions that immediately precede SAC dendrite stratification. Because SACs stratify early –  
123 before any other cell type investigated to date (Fig. 1; Kay and Sanes, 2013; Stacy and Wong,  
124 2003) – they are unlikely to form strata by following pre-existing laminar cues. Instead, we  
125 hypothesized that SACs create their sublayers by engaging in homotypic interactions. To test this  
126 idea, we examined embryonic retina to determine if and when SACs establish homotypic contact.

127 SACs exit the cell cycle at the apical retinal surface and migrate radially through the outer  
128 neuroblast layer (ONBL). They next arrive at the inner neuroblast layer (INBL), where  
129 postmitotic neurons reside (Hinds and Hinds, 1978; Fig. 2A,B). Then they begin to innervate the  
130 nascent IPL, which begins to appear in some retinal regions at E16 (Fig. 2A). To reveal SAC  
131 morphology throughout these steps, the early SAC marker *Isl1* (Galli-Resta et al., 1997) was  
132 used to drive Cre-dependent expression a membrane-targeted GFP (mGFP) reporter (*Isl1<sup>mG</sup>*  
133 mice). We also examined the orientation of SAC dendrite projections using antibodies to  
134 internexin, a marker of SAC primary dendrites (Fig. 2-Supplement 1). Staining was performed at  
135 E16, when SACs at all stages of their early development could be discerned (Fig. 2A-D).

136         Since mature SACs contact each other in the IPL, we expected that the onset of SAC  
137 homotypic contact would occur around the time of their earliest IPL projections. Surprisingly,  
138 however, this analysis revealed that SACs begin to contact each other within the INBL cell body  
139 layer upon the conclusion of their radial migration. Migrating SACs rarely interacted, but on  
140 arrival at the INBL, SAC arbors were observed touching the soma or primary dendrite of  
141 neighboring SACs (Fig. 2A-D). The majority of INBL SACs engaged in these soma-layer  
142 contacts, such that a GFP<sup>+</sup> arbor network connected them (Fig. 2G). Analysis of primary dendrite  
143 orientation indicated that soma-layer contacts likely arose due to projections targeted within this  
144 layer: Unlike mature SACs, which exclusively project their primary dendrites towards the IPL,  
145 many E16 SACs projected tangentially through the INBL – i.e., towards neighboring somata  
146 (Fig. 2E,F). We even noted cases where SACs appeared to project directly towards each other  
147 (Fig. 2E). These observations suggest that post-migratory SACs initiate contact with each other  
148 by generating an arbor network in the INBL cell body layer.

149 Many E16 SACs also innervate the nascent IPL, raising the question of whether the  
150 soma- or IPL-layer projection establishes the first homotypic contact. We concluded that soma-  
151 layer SAC contact precedes IPL innervation, for three reasons. First, soma contacts were found  
152 in retinal regions where the IPL had not yet emerged (Fig. 2-Supplement 2). Second, soma  
153 contacts were observed among cells that still showed migratory morphological features, such as  
154 apical and/or basal processes (Deans et al., 2011; Hinds and Hinds, 1978), and did not yet project  
155 into the IPL (Fig. 2D; Fig. 2-Supplement 2). Third, SAC dendrite polarization in the tangential  
156 plane was highly transient: By P1, the vast majority of SAC primary dendrites were oriented  
157 towards the IPL (Fig. 2E,F). These three observations suggest that INBL SACs transiently seek  
158 out homotypic soma contact before shifting to target the IPL.

159 We next sought to determine how long the soma-layer SAC arbor network persists. To  
160 this end we examined SAC anatomy at early postnatal ages using *Isl1<sup>mG</sup>* and *Chat<sup>mG</sup>* (Fig. 1-  
161 Supplement 1) mice. At P0-1, although SAC arbors within the soma layers no longer express  
162 internexin (Fig. 2-Supplement 1), the arbor network remained remarkably prominent (Fig. 2G).  
163 Most OFF SACs assumed a bi-laminar morphology, with one set of arbors in the IPL and  
164 another set targeting neighboring SACs in the INL (Fig. 2H-J,L; Fig. 2-Supplements 2-3). INL  
165 contacts were highly SAC-selective: 88.8% of branches terminated homotypically ( $n = 122$  arbor  
166 tips from 22 cells), significantly greater than the contact rate expected by chance (Fig. 2-  
167 Supplement 3). By P2-3, however, this dense INL network was mostly gone (Fig. 2G,L; Fig. 2-  
168 Supplement 2). ON SACs also made soma layer projections between P0-P3 that contacted  
169 neighboring SAC somata (Fig. 2K,L; Fig. 2-Supplement 3). Together, these observations  
170 demonstrate that both ON and OFF SACs make transient soma-layer homotypic contacts that

171 arise prior to IPL dendrite elaboration, and are disassembled at P2-3 after SAC sublayers have  
172 formed (Fig. 2M).

### 173 **Homotypic contact is required for SAC IPL innervation and dendrite lamination**

174 SAC homotypic contacts arise at a time when they could serve as a cue for IPL  
175 innervation and sublayer formation. To test this idea, we developed a genetic strategy to prevent  
176 SACs from contacting each other in vivo. *Ptf1a* encodes a transcription factor required for  
177 progenitor cells to assume an amacrine fate (Fujitani et al., 2006; Nakhai et al., 2007; Fig. 3-  
178 Supplement 1). We crossed conditional *Ptf1a*<sup>fllox</sup> mutant mice (Krah et al., 2015) to a Cre line  
179 (*Six3-Cre*; Furuta et al., 2000), that drives widespread recombination in central retina but spares  
180 some progenitors from Cre activity in peripheral retina (Fig. 3A; Fig. 3-Supplement 1). In *Six3-  
181 Cre; Ptf1a*<sup>fllox/fllox</sup> mice (abbreviated Ptf1a-cKO), only these spared Cre<sup>-</sup> progenitors were capable  
182 of giving rise to SACs, indicating that any SACs produced in these mutants are wild-type at the  
183 *Ptf1a* locus (Fig. 3C). Therefore, the Ptf1a-cKO mutant creates a situation where otherwise-  
184 normal SACs are present at significantly lower density than in wild-type retina (Fig. 3B,C). In  
185 P1-2 mutants, some SACs were effectively segregated from their neighbors – these were termed  
186 “solitary” SACs – while others had neighbors sufficiently nearby that they touched (Fig. 3B-F;  
187 Fig. 3-Supplement 2).

188 Comparing solitary to touching SACs in Ptf1a-cKO retinas revealed a role for homotypic  
189 contacts in promoting IPL innervation and sublayer formation. At P1-2, touching SACs projected  
190 normally to the IPL, similar to SACs from *Ptf1a*<sup>+</sup> littermates (Fig. 3D,E,G). This suggests that  
191 any changes in retinal cell type composition caused by loss of *Ptf1a* (Fig. 3-Supplement 1) are  
192 not by themselves sufficient to perturb SAC sublayer formation. By contrast, solitary SACs  
193 largely failed to innervate the IPL (Fig. 3F,G). This was not caused by abnormal migration:

194 Solitary SACs were properly positioned at the IPL border, but sent only rudimentary arbors into  
195 it (Fig. 3F; Fig. 3-Supplement 2). Solitary SACs were also more likely to project processes into  
196 the soma layers (Fig. 3G), and when they did so, the projections were typically more elaborate  
197 than those observed in wild-type retina (Fig. 3D,F; Fig. 3-Supplement 2). Thus, solitary SACs  
198 overgrew arbors directed towards neighboring somata instead of growing IPL dendrites. Both  
199 types of projection errors were also seen at P15, indicating that early errors persist to retinal  
200 maturity (Fig. 3-Supplement 2). Misprojecting SACs were still closely apposed to numerous  
201 other amacrine cells, and their arbors were intermingled in the IPL, strongly suggesting that  
202 generic amacrine interactions are not sufficient to ensure normal dendrite targeting (Fig. 3-  
203 Supplement 2). Instead, homotypic interactions are specifically required for IPL innervation and  
204 sublayer formation.

### 205 **Requirement for MEGF10 in SAC IPL innervation and sublayer formation**

206 To understand how SACs initiate IPL innervation upon homotypic contact, we next  
207 sought to identify the molecular cues that SACs use to recognize that contact has occurred. The  
208 cell-surface protein MEGF10 (Fig. 4A) is a strong candidate to mediate homotypic recognition in  
209 this context, for four reasons. First, it is selectively expressed by SACs during the perinatal  
210 period (Fig. 1B; Fig. 1-Supplement 1). Second, the onset of its expression coincides with onset  
211 of SAC homotypic contact at the conclusion of radial migration (Fig. 4B). Third, MEGF10  
212 protein is present on soma-layer SAC arbors, making it available to transduce signals arising on  
213 these arbors (Fig. 4C). Finally, MEGF10 mediates SAC-SAC interactions in a separate context –  
214 during formation of the orderly “mosaic” among SAC cell bodies across the retina (Kay et al.,  
215 2012). Thus, we tested whether MEGF10 also mediates SAC-SAC recognition to initiate IPL  
216 innervation. If so, SACs from mice lacking *Megf10* gene function should have phenotypes

217 similar to solitary *Ptf1a*-cKO SACs – i.e., reduced IPL innervation and increased arborization in  
218 cell body layers.

219 To test this prediction, we examined SAC anatomy in *Megf10* null mutants (Kay et al.,  
220 2012) and littermate controls at P0-1, when sublayers are first forming. We found a striking  
221 effect on sublayer formation: Both ON and OFF strata were absent or severely disrupted in  
222 mutants (Fig. 5A). The cause of sublayer absence was investigated using pan-SAC labeling (Fig.  
223 5A,B) and single-cell analysis (Fig. 5C; Fig. 6D). These studies revealed a severe deficit in IPL  
224 dendrite arborization: Most *Megf10*<sup>-/-</sup> SACs made only rudimentary, unstratified IPL projections  
225 at P0-1 ( $n = 1/15$  OFF SACs were stratified). Other amacrine cell types showed normal dendritic  
226 morphology in *Megf10* mutants (Fig. 5-Supplement 1), indicating that the phenotype was  
227 specific to SACs. Loss of IPL innervation was not due to aberrant SAC radial migration, because,  
228 at P0, mutant SACs had reached the inner retina in normal numbers (wild-type,  $2600 \pm 287$   
229 SACs/mm<sup>2</sup>; mutant,  $3153 \pm 145$  SACs/mm<sup>2</sup>;  $p = 0.144$ , 2-tailed *t*-test;  $n = 3$  each group), and  
230 were positioned adjacent to the IPL, similar to littermate controls (Fig. 5A). Furthermore, most  
231 mutant SACs sent at least some arbors into the IPL at P0-1 (Fig 5A,C; Fig. 6D), suggesting that  
232 they migrated to a location from which IPL innervation was feasible. However, the mutant SAC  
233 arbors that reached the IPL appeared undifferentiated, with a lack of space-filling branches (Fig.  
234 5A,C). As a result, not only did their arbors enclose a significantly smaller IPL territory, but they  
235 also failed to sample as much of their enclosed territory as control SACs (Fig. 5C; also compare  
236 to control cell in Fig. 2H). By P3 some ON SAC IPL innervation was evident, but OFF SAC  
237 arbors remained largely confined to the soma layer; those that did reach the IPL remained  
238 undifferentiated (Fig. 5B; Fig. 6A,D). These observations indicate that deletion of MEGF10  
239 causes an IPL innervation phenotype strongly reminiscent of *Ptf1a*-cKO solitary SACs: Both

240 manipulations profoundly impair SAC dendrite arborization within the IPL, preventing timely  
241 sublayer formation.

242 In contrast to their underinnervation of the IPL, *Megf10* mutant SACs arborized  
243 exuberantly in the soma layers (Fig. 6A). Both ON and OFF SACs were affected (Fig. 6D,E; Fig.  
244 6-Supplement 1), but the OFF SAC phenotype was particularly striking: Starting at P1, the  
245 mutant INL network became much more elaborate than the control network of any age (Fig.  
246 6A,C). INL arbor density increased in mutants from P0 to P1 and remained high at P3; by  
247 contrast, control SACs largely eliminated their INL projections over the same period (Fig 5A,B;  
248 Fig. 6A,E). To understand how mutant SACs generate a denser and more persistent soma-layer  
249 network, we assessed single SAC morphology (Fig. 6A,D). From this analysis we determined  
250 that one reason for the denser mutant network, particularly at P2-3, was that a larger number of  
251 mutant cells projected to the soma layers (Fig. 6E). However, this reason was not sufficient to  
252 explain the denser mutant INL network at P1 (Fig. 6C), because at that age the number of cells  
253 projecting to the INL was similar in mutants and littermate controls (Fig. 6E). Therefore, to  
254 account for this increase in INL arbor density, we surmised that individual mutant SAC must, on  
255 average, overinnervate INL. Supporting this conclusion, we found that mutant SACs frequently  
256 had more extensive INL arbors than littermate control SACs (Fig. 6B). Further, mutant SACs  
257 continued to grow primary dendrites tangentially within soma layers at P1, when the vast  
258 majority of control SACs only targeted the IPL (Fig. 6F; also see Fig. 2F). These observations  
259 indicate that mutant SACs continue to expand their soma layer arbor network at P1. Thus, as  
260 with solitary *Ptf1a*-cKO SACs, soma layer projections were both more frequent and more  
261 exuberant for *Megf10*<sup>-/-</sup> SACs.

262 Together, these data suggest that MEGF10 governs a developmental transition from  
263 soma-layer to IPL-layer dendrite growth (Fig. 6G): Whereas control SACs have only a brief  
264 period of soma-layer growth, switching to IPL ramification around P0, *Megf10* mutant SACs do  
265 not make this transition and instead persist in soma-layer innervation. As a result of this failed  
266 transition, many individual mutant SACs ramify extensively in the INL but underinnervate the  
267 IPL, causing the dendrite targeting phenotypes that were observed at the population level (Fig  
268 6A-C). We conclude that, because MEGF10 regulates IPL innervation in this way, MEGF10 is  
269 required for initial formation of SAC IPL sublayers.

#### 270 **SAC dendrite targeting requires transcellular MEGF10 signaling**

271 Given the similar phenotypes of *Megf10* mutant and solitary *Ptf1a*-cKO SACs, we  
272 hypothesized that MEGF10 is the molecular cue that triggers IPL innervation upon SAC-SAC  
273 contact. A key prediction of this model is that SACs should require MEGF10 signals from their  
274 neighbors to target their dendrites properly. To test this prediction, we generated a conditional  
275 *Megf10<sup>lox</sup>* allele and used it to create a situation where *Megf10<sup>+</sup>* SACs were surrounded by  
276 *Megf10<sup>-</sup>* mutant cells. This was accomplished via the same *Six3-Cre* strategy that we employed  
277 in our *Ptf1a*-cKO studies (Fig. 3A-C). In central retina of *Six3-Cre; Megf10<sup>lox/lacZ</sup>* (*Six3*-*Megf10*-  
278 cKO) animals, the vast majority of cells expressed a Cre-dependent GFP reporter, indicating that  
279 they lacked *Megf10* function (Fig. 6A). Accordingly, SACs projected exuberantly to the INL and  
280 sublayer formation was disrupted, as in null mutants (Fig. 7B; Fig. 7-Supplement 1).

281 In peripheral retina, some SACs escaped Cre activity, leading to absence of the GFP  
282 reporter and continued MEGF10 protein expression (Fig. 7A,B; Fig. 7-Supplement 1). Our  
283 model predicts that these cells should have mutant dendrite phenotypes despite retaining  
284 MEGF10. To test this prediction, we imaged  $\beta$ gal-stained OFF SACs from *Six3*-*Megf10*-cKO

285 and littermate control mice at P2. This age was chosen because wild-type and null mutant mice  
286 showed a large difference in SAC INL projection frequency (Fig. 6E). In littermate controls, we  
287 found that  $\beta\text{gal}^+$  SACs rarely projected to the INL (Fig. 7C,D); therefore, they behaved like  
288 control SACs from earlier experiments (Fig. 6E). By contrast, *Megf10*<sup>+</sup> SACs surrounded by  
289 mutant SACs in *Six3-Megf10-cKO* retina showed a high rate of INL projections, nearly identical  
290 to their *Megf10*<sup>-</sup> neighbors (Fig. 7B,D; Fig. 7-Supplement 1). Thus, when *Megf10*<sup>+</sup> SACs are  
291 deprived of MEGF10 signal from adjacent SACs, they make exuberant soma-layer projections.  
292 This finding implicates MEGF10 as a transcellular signal that controls SAC dendrite targeting  
293 (Fig. 7K).

294         Next we investigated how SACs receive this MEGF10 signal from their neighbors. Given  
295 that MEGF10 can function as a receptor in other contexts (Chung et al., 2013; Kay et al., 2012),  
296 we speculated that MEGF10 might act as its own receptor. In support of this idea, co-  
297 immunoprecipitation experiments using intracellularly truncated *Megf10* constructs showed that  
298 MEGF10 can interact with itself through its extracellular domain (Fig. 7I,J; Fig. 7-Supplement 2).  
299 Thus, MEGF10 appears biochemically capable of acting as both ligand and receptor.

300         If MEGF10 is indeed a receptor in this context, SACs should require it to detect contact  
301 with MEGF10-expressing homotypic neighbors. To test this prediction, we asked whether  
302 removal of *Megf10* from a single SAC, during the period of soma-layer homotypic contact,  
303 would impair its IPL innervation despite normal MEGF10 expression by surrounding cells. We  
304 used *Chat*<sup>Cre</sup> to achieve sparse recombination in SACs of neonatal mice, as in the anatomy  
305 experiments described above (Fig. 2H-K; Fig. 6D). In *Chat-Megf10-cKO* animals, MEGF10  
306 immunostaining was used to identify SACs that lost MEGF10 protein prior to P3 – i.e., during  
307 the period when soma-layer arbors are present (Fig. 7F,G). MEGF10<sup>-</sup> cells constituted a small

308 minority of SACs at P3, meaning that they were generally surrounded by MEGF10<sup>+</sup> neighbors  
309 (Fig. 7-Supplement 1). In this context, MEGF10<sup>-</sup> SACs produced more exuberant soma-layer  
310 arbors than neighboring MEGF10<sup>+</sup> cells, while sending only minimal arbors into the IPL (Fig.  
311 7E-H). Thus, single MEGF10<sup>-</sup> SACs had phenotypes similar to SACs from mice entirely lacking  
312 *Megf10* (Fig. 7G,H; compare to Fig. 6D). By contrast, adjacent MEGF10<sup>+</sup> cells in the same Chat-  
313 *Megf10*-cKO retinas were indistinguishable from littermate control SACs (Fig. 7E,F,H).  
314 Therefore, when *Megf10* is lost during dendro-somatic contact (but not after; see below), SACs  
315 make projection errors typical of neurons deprived of homotypic interactions, and they do so  
316 even if their neighbors express MEGF10 and are developing normally. Together, these  
317 experiments support the conclusion that MEGF10 is a receptor through which SACs detect each  
318 other to terminate soma-layer growth and initiate IPL innervation (Fig. 7K).

### 319 **SAC errors persist to adulthood in *Megf10* mutants**

320 We next asked whether neonatal MEGF10-mediated interactions influence the anatomy  
321 of SAC IPL sublayers at maturity. We found that SAC sublayers eventually formed (by P5; Fig.  
322 8H), and were present in the mature *Megf10*<sup>-/-</sup> retina, but they were marred by numerous errors.  
323 Sporadically, and at apparently arbitrary retinal locations, two kinds of local laminar disruptions  
324 were apparent. First, there were discontinuities in the ON and OFF strata, such that mutant SACs  
325 did not completely innervate their sublaminae (Fig. 8A-C). These discontinuities diminished  
326 retinal coverage within each mutant sublayer by ~15% (OFF decrease, 15.0 ± 0.9%; ON decrease,  
327 13.7 ± 4.0%; mean ± SD; *n* = 9 fields of view/2 mice per genotype). Innervation gaps were not  
328 observed for other amacrine cells, indicating that SACs were selectively affected (Fig. 8-  
329 Supplement 1). Examination of single SACs revealed that while dendritic patterning  
330 substantially recovered between P1 and adulthood, SAC arbor territories remained significantly

331 smaller in mutants (Fig. 8D). These phenotypes suggest that mutant SACs never fully made up  
332 for their initial IPL innervation deficit, thereby contributing to gaps in the dendritic plexus.

333         The second type of SAC error in mature *Megf10*<sup>-/-</sup> IPL was dendrite mistargeting to  
334 ectopic IPL strata (Fig. 8A,B,E). Both ON and OFF SACs were affected; in each case ectopic  
335 arbors were mostly found in IPL regions inappropriately close to the soma layers (Fig. 8A,B).  
336 *En-face* images of mutant IPL revealed that ectopic OFF arbors formed a patchy but extensive  
337 fascicle network connecting many of the cells (Fig. 8E,F;  $78.5 \pm 3.5\%$  of SACs participated in  
338 the network, mean  $\pm$  95% CI). This IPL network was morphologically similar to the ectopic INL  
339 network observed in mutants at earlier ages (Fig. 6C), raising the possibility that the early  
340 network gives rise to the adult network by shifting location from the INL to the IPL. Supporting  
341 this view, we found that a soma layer-to-IPL transition occurs at P5, when mutant SACs began  
342 projecting to ectopic IPL locations in addition to the soma layers (Fig. 8G,H; Fig. 8-Supplement  
343 1). This transition occurred without a significant change in the number of mutant SACs  
344 projecting into the ectopic network (Fig. 8F; Fig. 8-Supplement 1), suggesting that the same cells  
345 continued to participate in the network but simply altered their anatomy to target the IPL. Thus,  
346 early exuberant soma-layer projections appear to give rise to adult IPL ectopias, starting between  
347 P3 and P5.

348         Together, these two adult mutant phenotypes demonstrate that DS circuit sublayer  
349 formation is delayed and imperfect in the absence of MEGF10. While other mechanisms appear  
350 to partially compensate for MEGF10 in generating the sublayers, such mechanisms are not  
351 sufficient to prevent persistence of innervation gaps and laminar targeting errors. Thus, MEGF10  
352 is essential for normal formation of the mature SAC IPL projection.

353           Next we sought to directly test the idea that MEGF10 is required early – at the time of  
354 initial SAC homotypic contact – to ensure normal SAC IPL lamination at maturity. To this end,  
355 we used *Megf10<sup>fllox</sup>* mice to delete MEGF10 at different times. Deletion prior to the onset of  
356 homotypic contact, using the *Six3-Cre* line, fully phenocopied *Megf10<sup>-/-</sup>* adult IPL errors (Fig.  
357 8A), suggesting a requirement for MEGF10 at the time of contact. To remove MEGF10 from  
358 SACs that had already established homotypic contact, we used *Chat<sup>Cre</sup>*. In this line, the number  
359 of SACs expressing Cre gradually increases over the first postnatal days to encompass the full  
360 SAC population (Xu et al., 2016). Therefore, Chat-Megf10-cKO mice can be used both for early,  
361 sparse MEGF10 deletion (Fig. 7F-H) and for later, broad MEGF10 deletion. MEGF10  
362 immunostaining revealed that this late, broad deletion occurs between P3 and P5 (Fig. 7-  
363 Supplement 1), such that MEGF10 expression is largely preserved during the period when  
364 homotypic soma-layer contacts exist (Fig. 2L), but is eliminated shortly thereafter. In this  
365 *Chat<sup>Cre</sup>*-mediated deletion regime, SAC laminar targeting and gap errors were exceedingly rare  
366 (Fig. 9A). These experiments therefore define a time window for MEGF10 function (Fig. 9C):  
367 Adult IPL targeting phenotypes require absence of MEGF10 during the soma-layer projection  
368 phase of SAC development – i.e. prior to P3. Any additional activity of MEGF10 after P3 is  
369 dispensable for the adult IPL phenotype. These findings strongly support a model whereby the  
370 functions of MEGF10 during early homotypic contact – i.e. promoting IPL innervation and  
371 terminating soma-layer arbor growth – are necessary for development of normal SAC IPL  
372 innervation at maturity.

### 373 **Mosaic spacing errors do not account for SAC IPL phenotype in *Megf10* mutants**

374           In addition to laminar targeting errors, *Megf10* mutants also show disruptions in the  
375 mosaic spacing of SAC cell bodies across the retina: Instead of a regular, uniform distribution,

376 mutant SAC positioning is random (Kay et al., 2012). We considered the possibility that SAC  
377 IPL errors might arise due to MEGF10 effects on soma spacing. Two lines of evidence suggest  
378 that this is not the case. First, the two phenotypes were not well correlated at the individual SAC  
379 level: Regardless of the severity of their mosaic spacing defects, SACs made IPL targeting errors  
380 at a constant rate (Fig. 9-Supplement 1). This finding suggests that disturbed cell positioning  
381 does not influence the probability of making an IPL error. Second, using our *Megf10<sup>lox</sup>* allele, we  
382 were able to dissociate the IPL and mosaic phenotypes: Deletion of MEGF10 after P3 in Chat-  
383 *Megf10*-cKO mice caused mosaic patterning deficits, but IPL projections were largely normal  
384 (Fig. 9A,B). This finding demonstrates that IPL laminar perturbations are not an inevitable  
385 consequence of altered soma positioning. Altogether, these experiments support the notion that  
386 altered SAC position makes at best a minor contribution to IPL phenotypes; instead, delayed IPL  
387 innervation and exuberant soma-layer arborization are likely the major sources of perturbed SAC  
388 projections at maturity.

### 389 **SAC IPL errors induce laminar targeting errors by their DS circuit partners**

390 Next we asked whether MEGF10, and its effects on SAC sublayer formation, are  
391 important for assembly of the broader DS circuit. To this end we tested the impact of SAC IPL  
392 stratification errors on laminar targeting by their circuit partners. First, we examined ooDSGC  
393 IPL projections using the *Hblx9-GFP* (referred to as Hb9-GFP; Fig. 10) and *Drd4-GFP* (Fig. 10-  
394 Supplement 1) transgenic lines, which label ooDSGC subtypes with different preferred directions  
395 (Trenholm et al., 2011; Huberman et al., 2009). In littermate control mice ( $n = 9$ ), ooDSGC  
396 dendrites were tightly and selectively associated with SAC arbors, as shown previously (Vaney  
397 and Pow, 2000). This association was maintained in *Megf10* mutants: Both normal and ectopic  
398 SAC IPL arbors reliably recruited ectopic ooDSGC projections (Fig. 10A-C; Fig. 10-Supplement

399 1;  $n = 240$  ectopias from 5 mutants, >97% contained ooDSGC arbors). Further, when SAC gaps  
400 were present in the mutant IPL, ooDSGC dendrites typically grew around the gap edges and  
401 failed to enter them (Fig. 10D; Fig. 10-Supplement 1;  $n = 325$  gaps from 5 mutants, >95%  
402 devoid of ooDSGC arbors). Thus, SACs provide both permissive cues required for ooDSGC IPL  
403 innervation, and also attractive cues sufficient to recruit ooDSGCs to the wrong IPL sublayer.

404         Next we determined the impact of altered SAC lamination on the axons of bipolar cells  
405 that participate in the DS circuit (Fig. 11A). We examined the four cell types (BC2, BC3a, BC5,  
406 and BC7) that make extensive monosynaptic connections with SACs and ooDSGCs (Duan et al.,  
407 2014; Ding et al., 2016; Greene et al., 2016; Kim et al., 2014; Chen et al., 2014). Bipolar axons  
408 were marked with type-specific antibodies and mouse lines reported previously (Wässle et al.,  
409 2009; Duan et al., 2014), as well as a novel transgenic marker of BC5 (*Gjd2-GFP*; Fig. 11-  
410 Supplement 1). In wild-type retina, DS-circuit bipolar cells arborized in close contact with SAC  
411 dendrites; however, unlike ooDSGCs, they remained adjacent to SACs rather than overlapping  
412 them (Fig. 11A-D; Fig. 11-Supplement 1). This arrangement was preserved in *Megf10* mutants:  
413 Axons of all four bipolar cell types were recruited to ectopic IPL locations by mistargeted SAC  
414 arbors, where they stratified adjacent to SACs (Fig. 11B-D,F; Fig. 11-Supplement 1). For  
415 example, BC5 and BC7 terminals always sandwiched SAC arbors, regardless of their IPL  
416 location – even when doing so required formation of a supernumerary BC axon field between the  
417 normal and ectopic SAC sublayers (Fig. 11C,D). To quantify the mistargeting effect we  
418 measured the position of BC5 and BC7 terminals adjacent to ON SAC ectopias. Their arbors  
419 were pushed farther apart by SAC arbor clumps (Fig. 11C-E), which shifted BC7 terminals  
420 significantly towards the GCL by  $\sim 4 \mu\text{m}$  ( $69 \pm 0.8\%$  of IPL depth in control regions to  $74 \pm$   
421  $1.9\%$  in affected regions; mean  $\pm$  S.E.M.;  $n = 21$  control, 6 affected; 2-tailed *t*-test,  $p = 0.0024$ ).

422 These observations indicate that DS-circuit bipolar cells, like ooDSGCs, respond to SAC  
423 attractive cues. However, in contrast to ooDSGCs, bipolar cell projections were minimally  
424 affected by SAC IPL gaps. While BC5 and BC7 terminals were slightly mispositioned in the  
425 absence of SAC arbors – they were closer together – innervation of gap regions was otherwise  
426 normal (Fig. 11C-F). Thus, DS-circuit bipolar axons either do not require SAC-derived signals  
427 for IPL innervation, or the relevant signals are capable of acting over larger distances than the  
428 typical SAC IPL gap size (35-45  $\mu\text{m}$  maximum diameter). Altogether, these analyses of DS  
429 circuit anatomy in *Megf10* mutants support the notion that early-stratifying SACs form a scaffold  
430 that directs IPL laminar targeting of their circuit partners using multiple guidance strategies.

#### 431 **Early SAC homotypic interactions impact DS circuit function**

432 Finally, we investigated the extent to which developmental events controlled by MEGF10  
433 affect DS circuit function. We sought to determine whether the anatomical perturbations caused  
434 by loss of MEGF10 – SAC laminar targeting and mosaic spacing errors – alter direction coding  
435 by ooDSGCs. To do this we recorded from wild-type and *Megf10*<sup>-/-</sup> retinas on a large-scale  
436 multielectrode array (Field et al., 2007; Yu et al., 2017). ooDSGCs were identified based on their  
437 responses to drifting gratings and moving bars (see Methods), which unambiguously  
438 distinguished them from other recorded RGCs (Fig. 12A). Because MEGF10 is not expressed in  
439 the adult DS circuit (Kay et al., 2012), we could be confident that any mutant physiological  
440 phenotypes reflect anatomical changes that arose during development.

441 These experiments revealed that ooDSGCs with robust direction selectivity were present  
442 in both wild-type and *Megf10*<sup>-/-</sup> retinas (Fig. 12A,B), and constituted a similar fraction of the  
443 RGC population in both strains (wild-type: 80/609, 13.1%; mutant: 74/551, 13.4%).  
444 Furthermore, loss of *Megf10* did not alter the organization of ooDSGC preferred directions along

445 cardinal axes (Oyster and Barlow, 1967), or the fraction of ooDSGCs preferring each direction  
446 (Fig. 12-Supplement 1). These results are consistent with the observation that mutant SACs  
447 remain paired with ooDSGC dendrites and bipolar cell axons even when normal lamination and  
448 arbor spacing are disrupted. They indicate that the qualitative functional properties of the circuit  
449 are still present.

450         However, a more careful examination of DS tuning properties in *Megf10*<sup>-/-</sup> retinas  
451 revealed clear quantitative differences in ooDSGC responses. Moving bars were used to measure  
452 the width and strength of direction tuning for each identified ooDSGC across the populations  
453 recorded on the electrode array (Fig. 12C). Tuning width was measured as the circular standard  
454 deviation of the tuning curve, while tuning strength was measured as the normalized response  
455 difference to motion in the preferred and null directions (see Methods). These experiments  
456 revealed systematic shifts toward broader (Fig. 12D) and weaker (Fig. 12E) direction tuning  
457 across the population of ooDSGCs in *Megf10* mutant retinas. This was mainly due to higher null  
458 direction spiking among ooDSGCs in mutants (Fig. 12B,C,E). Furthermore, these effects on  
459 tuning width and strength persisted across a broad range of stimulus contrasts (Fig. 12-  
460 Supplement 1). These results demonstrate that disruption of MEGF10-dependent developmental  
461 patterning degrades the precision and strength of ooDSGC direction tuning. They further suggest  
462 that perturbations to the anatomical regularity of the circuit across space (e.g. laminar uniformity  
463 and SAC spacing) may effectively introduce noise in the DS circuit that broadens and weakens  
464 direction tuning (see Discussion).

465         This idea led us to consider additional functional properties of ooDSGCs that might  
466 depend on the spatial regularity of the DS circuit, and therefore might be perturbed in *Megf10*  
467 mutants. One such property is the generation of symmetric DS responses to stimuli that are

468 darker or brighter than the background (Fig. 12F,G). This ON-OFF symmetry allows the DS  
469 response to be largely insensitive to contrast reversals (Amthor and Grzywacz, 1993); it arises  
470 because ooDSGCs receive highly symmetric SAC inputs in both ON and OFF sublayers (Fig.  
471 1A). In *Megf10* mutants, ON-OFF anatomical symmetry is disturbed, because ON and OFF SAC  
472 errors are not spatially correlated (Fig. 8A-C). We hypothesized that this might lead to disparities  
473 in the direction tuning of individual cells' ON and OFF responses. Indeed, *Megf10*<sup>-/-</sup> ooDSGCs  
474 exhibited greater separation (i.e. less coherence) between their ON and OFF preferred directions  
475 than wild-type ooDSGCs, across a broad range of contrasts (Fig. 12H; Fig. 12-Supplement 1).  
476 These results support the idea that MEGF10 serves to establish a highly uniform and regular  
477 network of SAC dendrites (via controlling both the precise timing of INL lamination and through  
478 regularizing inter-SAC spacing), the net effect of which is to allow greater precision and  
479 coherence in the direction tuning of ooDSGCs.

## 480 **DISCUSSION**

481           Neural circuits typically consist of multiple cell types born at different places and times,  
482 raising the question of how circuit partners manage to converge at a common site for selective  
483 synapse formation. Here we describe a developmental strategy that the retinal DS circuit uses to  
484 solve this problem. We show that SACs coordinate amongst themselves to assemble a dendritic  
485 scaffold that subsequently recruits projections from their DS circuit partners. By identifying for  
486 the first time a genetic manipulation – loss of *Megf10* – that causes SACs to misproject outside  
487 their two typical IPL layers, we uncover mechanisms by which SACs assemble this dendritic  
488 scaffold. Further, we use *Megf10* mutants to examine the effects on DS circuit anatomy and  
489 function when the SAC scaffold is disrupted. We find that MEGF10 establishes DS circuit  
490 spatial homogeneity across the retina, both by controlling IPL innervation patterns and by  
491 positioning SAC cell bodies. In *Megf10* mutants, disruptions in circuit homogeneity occur with  
492 minimal effects on radial SAC dendrite anatomy or synaptic partnering, making the phenotype  
493 unique among DS circuit developmental mutants. Finally, we find that this abnormal spatial  
494 pattern degrades DS circuit function by broadening the range of directions to which ooDSGCs  
495 will respond, and by weakening overall direction selectivity. These results provide new insight  
496 into general strategies for circuit development, as well as the specific mechanisms that ensure  
497 functional assembly of the DS circuit.

### 498 **Homotypic recognition as a mechanism regulating dendrite differentiation**

499           During radial migration, newborn central nervous system neurons have a multipolar  
500 morphology, but on arrival at their final position within the tissue they become highly polarized  
501 (Nadarajah et al., 2001; Tabata and Nakajima, 2003; Cooper, 2014; Chow et al., 2015; Krol et al.,  
502 2016; Hinds and Hinds, 1978). This morphological change enables elaboration of dendrites and

503 integration into local circuitry. If dendrite differentiation begins early, migration is impaired  
504 (Hoshiba et al., 2016), suggesting that the transition from migratory to mature morphology must  
505 be highly regulated to ensure that neurons only differentiate once they arrive at their final  
506 position. The extracellular cues that signal arrival are poorly understood in most nervous system  
507 regions.

508         Here we show that SACs use homotypic recognition, mediated by MEGF10, to initiate  
509 IPL-directed dendrite morphogenesis. When deprived of homotypic neighbors or MEGF10,  
510 SACs at the IPL retain a multipolar morphology (compare Fig. 2C to Figs. 3F, 6A) instead of  
511 polarizing arbors towards the IPL. This indicates that the transition from migratory to mature  
512 morphology is impaired in the absence of SAC homotypic recognition. We show that migrating  
513 SACs first establish homotypic contact upon arrival at the inner retina. At this stage they are still  
514 multipolar (Fig. 2D), but they orient primary dendrites tangentially within the INBL to ultimately  
515 contact their SAC neighbors. These contacts occur prior to IPL innervation, and are required for  
516 it to occur in a timely manner. SACs lacking neighbors or the molecular means to detect them  
517 (i.e., MEGF10) appear to persist in this multipolar soma-layer-targeting phase, causing over-  
518 innervation of the INL/GCL and delaying IPL innervation (Fig. 6G). Thus, establishment of  
519 homotypic contact is a key checkpoint for the progression of SAC dendrite differentiation and  
520 IPL sublayer morphogenesis.

521         We propose that the function of this checkpoint is to ensure that SACs elaborate dendrites  
522 only when they have arrived adjacent to the IPL. The presence of other SACs that have already  
523 completed their migration is a reliable indicator of arrival in the proper location. Because soma-  
524 layer SAC contacts appear earliest, and because MEGF10 selectively influences IPL innervation  
525 during the period when they exist, we favor the notion that the key homotypic interactions occur

526 through these arbors. However, we cannot exclude that IPL-based interactions also play a role.  
527 INL-directed arbors resembling those we describe can be discerned in many developing  
528 zebrafish amacrine cells (Godinho et al., 2005; Chow et al., 2015), raising the possibility that this  
529 mechanism applies across species and across other amacrine cell types. Because most neurons  
530 require a way to control when and where they differentiate, we anticipate that this homotypic  
531 contact strategy, or variations upon it, may have important roles in the differentiation of other  
532 CNS neurons at the completion of their radial migration.

### 533 **MEGF10 as the signal mediating SAC homotypic recognition**

534 We conclude that MEGF10 is the molecule responsible for homotypic recognition during  
535 SAC IPL innervation. Four key results support this conclusion. First, MEGF10 is expressed at  
536 the right time and place to assume this role: It is expressed selectively in SACs (Fig. 1), upon  
537 conclusion of their radial migration, and in the soma-layer arbors that we propose mediate  
538 recognition (Fig. 4). Second, *Megf10* null mutant SACs phenocopy the dendrite polarization  
539 errors seen in solitary *Ptf1a*-cKO SACs, suggesting that homotypic recognition requires *Megf10*.  
540 Third, co-immunoprecipitation experiments indicate that MEGF10 interacts with itself via its  
541 extracellular domain, suggesting it could act as both ligand and receptor. While this biochemical  
542 interaction may take place in the *cis* configuration, the fourth line of evidence indicates that  
543 MEGF10 interacts in *trans* as well: Using a conditional-null *Megf10* allele in vivo, we show that  
544 MEGF10 is required on the cell that sends homotypic signals as well as the cell receiving those  
545 signals. Loss of MEGF10 on either side leads to dendritic phenotypes resembling solitary SACs  
546 and *Megf10* null mutants. Together, these data are consistent with a model whereby SAC-SAC  
547 contact initiates a transcellular MEGF10 homophilic interaction, in which MEGF10 serves as

548 both receptor and ligand to trigger the switch from migratory to mature morphology (see model,  
549 Fig. 7K).

550 This homophilic model of MEGF10 function is consistent with its role during  
551 establishment of mosaic cell body patterning (Kay et al. 2012). In that context, MEGF10 acts as  
552 ligand and receptor to mediate cell-cell repulsion, thereby spacing SAC somata evenly across the  
553 retina. Here we discover a second MEGF10 function in SAC IPL innervation. Because the two  
554 SAC phenotypes have different underlying cell biology (soma movement vs. dendrite dynamics),  
555 and separable temporal requirements for MEGF10 function (Fig. 9), it seems unlikely that they  
556 reflect disruption of a single biological event. Instead, MEGF10 appears to act at distinct, albeit  
557 partially overlapping times, to control different aspects of SAC development, each of which are  
558 regulated by contact with homotypic neighbors (see model, Fig. 9C).

### 559 **Formation of SAC IPL sublayers**

560 Our results shed light on the mechanisms controlling SAC dendrite lamination. While  
561 repulsion mediated by *Sema6a* and *PlexinA2* prevents OFF SACs from straying to the ON  
562 sublayer (Sun et al., 2013), molecules required for formation of the SAC sublayers have not been  
563 identified. We show that SACs deprived of homotypic neighbors or MEGF10 initially fail to  
564 form IPL sublayers, and when they eventually do so, their strata are riddled with errors. Both the  
565 lack of sublayers at early stages and the dendritic mistargeting to inappropriate sublayers at  
566 maturity are novel SAC phenotypes; they implicate MEGF10 as a key player in forming SAC  
567 IPL sublayer-specific projections.

568 It is generally assumed that sublayer formation has two basic molecular requirements: 1)  
569 Attractive/adhesive molecules that mediate co-fasciculation of stratified arbors; and 2) repulsive  
570 cues that prevent straying of arbors into other sublayers (Lefebvre et al., 2015; Sanes and

571 Yamagata, 2009). Our MEGF10 studies suggest an additional, earlier requirement for cell-cell  
572 interactions that occur prior to neuropil innervation. The purpose of this surprisingly early SAC-  
573 SAC interaction, we propose, is to ensure that SACs grow dendrites at the right time and place to  
574 co-fasciculate with their SAC neighbors. The molecular basis of this homotypic co-fasciculation  
575 – clearly another essential player in sublayer formation – remains to be determined. MEGF10 is  
576 probably not involved; the co-fasciculation system appears intact in *Megf10* mutants given that  
577 sublayers do eventually form. Perhaps this system is part of the mechanism that compensates for  
578 loss of MEGF10 to ultimately generate the sublayers.

579         When IPL arborization is delayed by loss of *Megf10*, two SAC errors ensue. First, SACs  
580 generate mistargeted dendritic material that appears to persist as ectopic IPL sublayers. Second,  
581 SACs never completely innervate their sublayers, resulting in fragmented IPL strata. These two  
582 errors are caused by delays rather than an ongoing requirement for MEGF10 during later stages  
583 of arbor growth, as shown by conditional mutant experiments (Fig. 9). Thus, our findings support  
584 the idea that timing is critical to the sequential lamination of the IPL: When SAC dendrites arrive  
585 in the IPL too late, they encounter a different cellular and molecular milieu that may not support  
586 the proper development of their arbors. In this view, the normal role of MEGF10 in DS circuit  
587 assembly is to instigate SAC dendrite outgrowth at the crucial time when laminar self-assembly  
588 can occur.

589         SACs may face an additional obstacle to overcoming their delayed IPL innervation in  
590 *Megf10* mutants: abnormal soma positioning. While mosaic spacing errors do not account for the  
591 *Megf10* mutant ectopic IPL phenotype, we cannot exclude the possibility that the placement of  
592 IPL arbor gaps might be at least partly explained by soma position. If SACs are struggling to  
593 make up for their delayed IPL innervation, it is plausible that increasing the distance between

594 SACs (as happens sporadically due to random positioning) might further hinder the development  
595 of complete retinal coverage.

### 596 **SACs as a scaffold for DS circuit assembly**

597       Because of their early stratification, SAC dendrites have been proposed to act as a  
598 scaffold that guides assembly of the DS circuit (Stacy and Wong, 2003). A key prediction of this  
599 model is that laminar targeting of later-stratifying cell types should depend on the existence of  
600 this scaffold. We show using a SAC-specific manipulation – removal of *Megf10* – that disruption  
601 of SAC stratification causes their bipolar and ooDSGC circuit partners to make corresponding  
602 projection errors. Based on the kinds of errors we observed, SACs appear to provide attractive,  
603 permissive, and possibly even repulsive arbor sorting cues to influence the laminar positioning of  
604 their circuit partners. This work thus constitutes the first critical test of the scaffolding model,  
605 and provides strong support for it. We find that SACs use homotypic interactions to initiate  
606 formation of their circuit sublayers, and then heterotypic interactions to recruit circuit partners to  
607 join them. SACs might achieve their scaffolding functions directly, by providing guidance cues  
608 to their partners; or they may do so indirectly, by patterning the IPL projections of an  
609 intermediary cell type that in turn guides later-arriving projections. Direct scaffolding may be  
610 mediated in part by Cadherins 8 and 9, which regulate interactions between SAC dendrites and  
611 DS circuit bipolar cell axons (Duan et al., 2014). Molecular mediators of ooDSGC-SAC dendrite  
612 interactions remain to be identified.

613       Evidence that the SAC scaffold can be repulsive – or at least can exclude bipolar arbors  
614 from certain IPL regions – came from our observations of BC axon anatomy. In wild-type retina,  
615 we were surprised to note how completely the BC3a, BC5, and BC7 axon terminals were  
616 excluded from the SAC territory – they contacted it but did not enter (Fig. 11B-D; Fig. 11-

617 Supplement 1). This behavior stands in stark contrast to the behavior of ooDSGC dendrites,  
618 which completely overlapped SACs (Fig. 10A-B; Vaney and Pow, 2000). Moreover, in *Megf10*  
619 mutants, the laminar distance between BC5 and BC7 terminals was reduced in the absence of  
620 SAC arbors, and increased in the presence of SAC ectopias, further suggesting the existence of  
621 local SAC-BC repulsion. The finding that SACs exclude bipolar circuit partners from their  
622 sublayers appears at first counterintuitive. But given that no bipolar cell type is exclusively  
623 devoted to the DS circuit (Wässle et al., 2009; Greene et al., 2016; Kim et al., 2014), a  
624 mechanism must exist to ensure that they can also contact non-DS partners. We speculate that  
625 SACs initially recruit their bipolar partners using long-range attractive cues, and then use  
626 contact-repulsion (or an equivalent arbor sorting mechanism) to displace bipolar arbors such that  
627 they remain in contact with the SAC layers but also innervate adjacent layers. This model is  
628 consistent with bipolar arbor phenotypes in *Megf10* mutants, but will require further study.

### 629 **Role of MEGF10 in the functional assembly of DS circuitry**

630 We found that impairment of SAC interactions in the perinatal retina causes permanent  
631 functional DS circuit deficits. In *Megf10* mutants, direction tuning of ooDSGCs becomes broader  
632 and weaker, and their ON/OFF preferred directions are less aligned. Direction tuning is degraded  
633 in large part because mutant ooDSGCs have aberrant spiking responses to null-direction stimuli.  
634 This suggests that impaired null-direction inhibition – which arises from SACs – is a key  
635 contributor to the phenotype. Broader ooDSGC tuning curves have been shown, in modeling  
636 studies, to degrade population-level coding of directional information, and the ability of  
637 downstream neurons to extract such information (Fiscella et al., 2015). Thus, the physiological  
638 phenotypes we identified are likely sufficient to impair the ability of mutant retina to  
639 appropriately relay visual information.

640 Dysfunctional DS circuit physiology in *Megf10* mutants is almost certainly a  
641 consequence of its effects on development, because neurons do not express MEGF10 beyond the  
642 second postnatal week (Kay et al., 2012). Further, even though MEGF10 is expressed by Müller  
643 glia in adulthood, we have been unable to detect any changes in Müller glia anatomy or  
644 interactions with DS circuit synapses upon loss of *Megf10* function (Wang et al., 2017; J.W. and  
645 J.N.K., unpublished observations). We therefore conclude that anatomical changes to the DS  
646 circuit arising during development are responsible for circuit dysfunction.

647 The fundamental change to DS circuit anatomy in *Megf10* mutants is altered distribution  
648 of arbors and synapses, unlike other manipulations which simply serve to destroy SAC radial  
649 morphology or disrupt synaptic partnering among DS circuit cells (Sun et al., 2013; Duan et al.,  
650 2014; Kostadinov and Sanes, 2015; Peng et al., 2017). In *Megf10* mutants, the combined effect  
651 of mosaic spacing defects and IPL laminar targeting errors is to disturb the regularity of SAC  
652 IPL innervation. As a result, some parts of the visual map become over-innervated (e.g. Fig. 9A)  
653 while others are uninnervated (Fig. 9C). In turn, ooDSGCs are recruited to the over-innervated  
654 regions and excluded from uninnervated gaps, likely causing sporadic local inhomogeneity in  
655 synapse density across visual space. According to some models of DS, which posit that the total  
656 amount of SAC inhibition is the key factor underlying DS responsiveness, these relatively small-  
657 scale changes would be considered unlikely to change circuit function (Taylor and Vaney, 2002;  
658 Demb, 2007). A more recent alternate view is that the fine spatial arrangement of glutamatergic  
659 inputs to SACs, and the synaptic balance of SAC and bipolar input onto ooDSGC dendrites, are  
660 both important for DS responses (Ding et al., 2016; Vlasits et al., 2016; Poleg-Polsky and  
661 Diamond, 2016; Sethuramanujam et al., 2016, 2017). The finding that *Megf10* mutants have DS  
662 tuning phenotypes suggests that local synaptic arrangements are indeed important for the DS

663 computation. More broadly, this finding shows that the developmental mechanisms we describe  
664 here are important for enabling circuit function, raising the possibility that other circuits  
665 throughout the retina and CNS may use similar developmental mechanisms to establish their  
666 functional connectivity.

667

## 668 MATERIALS AND METHODS

## 669 Key Resources Table

Reagent type	Designation	Source or Reference	Identifier	Additional information
Antibody	Megf10: rabbit, 1:1000	Kay et al., 2012		
Antibody	Sox2: rabbit, 1:500	Abcam	ab97959	
Antibody	Sox2: goat, 1:500	Santa Cruz	sc-17320	
Antibody	ChAT: goat, 1:400	EMD Millipore	AB144P	
Antibody	Beta Galactosidase: rabbit, 1:5000	other		Antibody was a gift of J.R. Sanes, Harvard
Antibody	GFP: chicken, 1:1000	Life Technologies	A10262	
Antibody	GFP (Co-IP): rabbit, 1:1000	Thermo Fisher Scientific	A-6455	
Antibody	AP-2a: mouse, 1:200	Developmental Studies Hybridoma Bank	3B5	
Antibody	RBPMS: guinea pig, 1:2000	other		Antibody was a gift of N. Brecha, UCLA
Antibody	Chx10: sheep, 1:300	Exalpha	X1180P	
Antibody	Chx10: goat, 1:500	Santa Cruz	sc-21690	
Antibody	GAD65: rabbit, 1:1000	Millipore	AB1511	
Antibody	FLAG: mouse, 1:500	Sigma Aldrich	F-1804	
Antibody	VGLUT3 guinea pig	synaptic systems	135 204	
Antibody	Synaptotagmin-2 (Sy2), mouse, 1:250	Zebrafish International Resource Center	ZDB-ATB-081002-25	
Antibody	Isl1: mouse, 1:25	Developmental Studies Hybridoma Bank	39.4D5	
Antibody	Internexin: rabbit, 1:1000	EMD Millipore	AB5354	
Antibody	Normal Rabbit IgG	Cell signaling Technology	2729S	
Antibody	Normal Mouse IgG	Cell Signaling Technology	5415S	
Antibody	Alexa Fluor 488 AffiniPure Donkey Anti-Chicken: 1:1000	Jackson ImmunoResearch	703-545-155	
Antibody	Alexa Fluor 488 AffiniPure Donkey Anti-rabbit: 1:1000	Jackson ImmunoResearch	711-545-152	
Antibody	Alexa Fluor 488 AffiniPure Donkey Anti-goat: 1:1000	Jackson ImmunoResearch	705-545-147	

Antibody	Alexa Fluor 488 AffiniPure Donkey Anti-mouse: 1:1000	Jackson ImmunoResearch	706-605-148	
Antibody	Alexa Fluor 647 AffiniPure Donkey Anti-rabbit: 1:1000	Jackson ImmunoResearch	705-605-147	
Antibody	Cy3-AffiniPure Donkey Anti-rabbit: 1:1000	Jackson ImmunoResearch	715-165-151	
Antibody	Cy3-AffiniPure Donkey Anti-Guinea Pig: 1:1000	Jackson ImmunoResearch	706-165-148	
Antibody	Cy3-AffiniPure Donkey Anti-Goat: 1:1000	Jackson ImmunoResearch	705-165-147	
Antibody	IRDye® 680RD Donkey anti-Mouse IgG (H + L): 1:1000	Li-Cor Biosciences	925-68072	
Antibody	IRDye® 800CW Donkey anti-Rabbit IgG (H + L): 1:1000	Li-Cor Biosciences	925-32213	
biological sample (AAV)	AAV9.hEF1a.lox.TagBFP.l ox.eYFP.lox.WPRE.hGH-InvBYF(Harvard)	Penn Vector Core	AV-9-PV2453	
biological sample (AAV)	AAV9.hEF1a.lox.mCherry.l ox.mTFP1.lox.WPRE.hGH-InvCheTF(Harvard)	Penn Vector Core	AV-9-PV2454	
chemical compound	Fetal Bovine Serum	Life Technologies	16250-078	
chemical compound	Opti-MEM® I Reduced Serum Medium	Thermo Fisher Scientific	31985070	
chemical compound	Polyethylenimine (PEI), Linear (MW 25,000)	VWR/Polysciences	23966-2	
chemical compound	16% Paraformaldehyde	Electron Microscopy Sciences	15710	
chemical compound	Normal Donkey Serum	Jackson ImmunoResearch	017-000-121	
Other	Immun-Blot Low Fluorescence PVDF membrane	Bio-Rad	1620264	
chemical compound	Fluoromount G	SouthernBiotech	0100-01	
chemical compound	Hoechst 33258	Invitrogen	H21491	
chemical compound	Isothesia: Isoflurane	Henry Schein	11695-6776	
chemical compound	Tissue Freezing Medium	VWR	15148-031	

chemical compound	Acrylamide/Bis solution	Bio-Rad	161-0158	
chemical compound	4x Laemmli Sample Buffer	Bio-Rad	1610747	
chemical compound	Immun-Blot® Low Fluorescence PVDF membrane	Bio-Rad	1620264	
chemical compound	Odyssey Blocking Buffer	Li-Cor Biosciences	927-40000	
chemical compound	Dynabeads® Protein G for Immunoprecipitation	Thermo Fisher Scientific	10003D	
chemical compound	cOmplete™, Mini, EDTA-free Protease Inhibitor Cocktail Tablets	Roche	4693159001	
commercial assay or kit	Bio-Rad DC Protein Assay Kit	Bio-Rad	5000112	
strain (musculus)	Mouse: <i>Megf10<sup>LacZ</sup></i>	Kay et al., 2012	<i>Megf10<sup>tm1b(KOMP)Jrs</sup></i>	
strain (musculus)	Mouse: <i>Megf10<sup>fllox</sup></i>	this study	<i>Megf10<sup>tm1c</sup></i>	see Methods, "Animals" section
strain (musculus)	Mouse: Ptf1a-cKO	Krah et al., 2015	<i>Ptf1a<sup>tm3Cvw</sup></i>	
strain (musculus)	Mouse: <i>Isl1<sup>Cre</sup></i>	Jackson Labs 024242	<i>Isl1<sup>tm1(cre)Sev/J</sup></i>	
strain (musculus)	Mouse: Hb9-GFP	Jackson Labs 005029	B6.Cg- <i>Tg(Hlxb9-GFP)1Tmj/J</i>	
strain (musculus)	Mouse: <i>Chat<sup>Cre</sup></i>	Jackson Labs 006410	<i>Chat<sup>tm2(cre)Lowl</sup></i>	
strain (musculus)	Mouse: <i>Six3-Cre</i>	Jackson Labs 019755	Tg(Six3-cre)69Frty	
strain (musculus)	Mouse: <i>Kcng4<sup>Cre</sup></i>	Jackson Labs 029414	<i>Kcng4<sup>tm1.1(cre)Jrs</sup></i>	
strain (musculus)	Mouse: <i>Drd4-GFP</i>	Huberman et al., 2009	<i>Tg(Drd4-EGFP)W18Gsat</i>	
strain (musculus)	Mouse: <i>Gjd2-GFP</i>	MMRRC	<i>Tg(Gjd2-EGFP)JM16Gsat/Mmucd</i> ; RRID:MMRRC_030611-UCD	
strain (musculus)	Mouse: <i>Rosa26<sup>mTmG</sup></i>	Jackson Labs 007676	<i>Gt(ROSA)26Sor<sup>m4(ACTB-tdTomato,-EGFP)Luo</sup></i>	
strain (musculus)	Mouse: <i>Rosa26<sup>fGFP</sup></i>	Rawlins et al., 2009	<i>Gt(ROSA)26Sor<sup>m1(CAG-EGFP)Blh</sup></i>	
strain (musculus)	Mouse: <i>Rosa26<sup>Ai14</sup></i>	Jackson Labs 007914	B6.Cg- <i>Gt(ROSA)26Sor<sup>m14(CAG-tdTomato)Hze/J</sup></i>	

strain (musculus)	Mouse: <i>ACTB:FLPe</i>	Jackson Labs 003800	B6;SJL- <i>Tg(ACTFLPe)9205Dym/J</i>	
strain (musculus)	Mouse: <i>Gad1-GFP</i>	Jackson Labs 007677	<i>Tg(Gad1-EGFP)G42Zjh</i>	
strain (musculus)	Mouse: C57Bl6/J	Jackson Labs 000664	C57BL/6J	
cell line (human)	HEK293T	ATCC	293T (ATCC® CRL-3216™)	Cell line was authenticated by ATCC at time of purchase
recombinant DNA reagent	CMV-M10-FLAG	this paper		see Methods, "Generation of MEGF10-ΔICD constructs" section
recombinant DNA reagent	CMV-M10-GFP	Kay et al., 2012		
recombinant DNA reagent	pCMV-MEGF10-ΔICD-GFP	Kay et al., 2012		
recombinant DNA reagent	MEGF10-ΔICD-Flag	this paper		see Methods, "Generation of MEGF10-ΔICD Constructs" section
recombinant DNA reagent	pAAV-EF1a-Brainbow-tagBFP-EYFP-WPRE	Addgene	45185	
recombinant DNA reagent	pAAV-EF1a-Brainbow-mTFP1-Cherry-WPRE	Addgene	45816	
software	Fiji/ImageJ	Schindelin et al., 2012		
software	Prism	GraphPad		
software	NIS Elements	Nikon Instruments		
software	Custom JAVA scripts for spike sorting	Yu et al. 2017		
software	Custom MATLAB scripts for data analysis	this paper	<a href="https://github.com/Field-Lab/megf10-dstuning">https://github.com/Field-Lab/megf10-dstuning</a>	see Methods, "Multielectrode Array Recordings"; "Quantification & Statistical Analysis" sections
software	Matlab	Mathworks, Natick, MA		
software	Image Studio™	LI-COR Biosciences		
software	Photoshop	Adobe		
sequence-based reagent	M10flagNotI_Rev	IDT	ATAGCGGCCG CttaCTTGTCGT CATCGTCTTTG TAGTCttcactgct gctgctgctgctg	

sequence-based reagent	M10flag_Fwd	IDT	GGTACATGCC TGTGCGAAGC A
sequence-based reagent	Cyto9_flag_Rev1	IDT	5'ATAGCGGCC GCTtaCTTGTCTG TCATCGTCTTT GTAGTC TTCCTTCCTCT TCTGCTTGTGT

670

671 **Animals**

672 All animal experiments were reviewed and approved by the Institutional Animal Care  
673 and Use Committee of Duke University. The animals were maintained under a 12-hour light-  
674 dark cycle with *ad lib* access to food and water. Retinas from adult (4-8 weeks old) *Megf10*<sup>-/-</sup>  
675 mutant mice and wild-type control mice with same genetic background were used for  
676 experiments performed on the multielectrode array (MEA). Animals were dark-adapted  
677 overnight prior to the experiment.

678 For this study the following transgenic and mutant mouse lines were used: 1)  
679 *Megf10*<sup>tm1b(KOMP)Jrs</sup> (Kay et al., 2012), referred to as *Megf10*<sup>-</sup> or *Megf10*<sup>lacZ</sup>; 2) *Ptf1a*<sup>tm3Cvw</sup> (Krah  
680 et al., 2015), referred to as *Ptf1a*<sup>fllox</sup> or (when crossed to Cre mice) Ptf1a-cKO; 3) *Isl1*<sup>tm(cree)Sev</sup>  
681 (Yang et al., 2006), referred to as *Isl1*<sup>Cre</sup>; 4) *Tg(Hlxb9-GFP)ITmj/J* (Trenholm et al., 2011),  
682 referred to as Hb9-GFP; 5) *Chat*<sup>tm2(cree)Lowl</sup> (Rossi et al., 2011), referred to as *Chat*<sup>Cre</sup>; 6) *Tg(Six3-*  
683 *cre)69Frty* (Furuta et al., 2000) referred to as *Six3-Cre*; 7) *Kcng4*<sup>tm1.1(cree)Jrs</sup> (Duan et al., 2014)  
684 referred to as *Kcng4*<sup>Cre</sup>; 8) *Tg(Drd4-EGFP)W18Gsat* (Huberman et al., 2009), referred to as  
685 *Drd4-GFP*; 9) *Tg(Gjd2-EGFP)JM16Gsat*, referred to as *Gjd2-GFP*; 10) *Tg(Gad1-*  
686 *EGFP)G42Zjh*, referred to as *Gad1-GFP*. Two Cre reporter strains were used that express  
687 membrane-targeted green fluorescent protein (mGFP) upon Cre recombination: 1)  
688 *Gt(ROSA)26Sor*<sup>tm4(ACTB-tdTomato,-EGFP)Luo</sup>, also known as *mT/mG* (Muzumdar et al., 2007); 2)

689 *Rosa26<sup>GFP</sup>* (Rawlins et al., 2009). An additional Cre reporter strain was used that expresses  
690 tdTomato fluorescent protein upon Cre recombination: *Gt(ROSA)26Sor<sup>tm14(CAG-tdTomato)Hze</sup>*  
691 (Madisen et al., 2010). See Key Resources table for repository stock numbers where applicable.

692 To produce *Megf10<sup>lox</sup>* mice, *Megf10<sup>tm1a(KOMP)Jrs</sup>* mice (Kay et al., 2012) were crossed to  
693 germline Cre strain *B6;SJL-Tg(ACTFLPe)9205Dym/J*, thereby generating a functional allele  
694 (also known as *Megf10<sup>tm1c</sup>*) in which exon 4 was flanked by loxP sites.

### 695 **Cell Culture**

696 HEK293T cells were obtained from, validated by, and mycoplasma tested by ATCC. The  
697 cells were cultured in Dulbecco's Modified Eagle's Medium (DMEM) with 10% bovine growth  
698 serum, 4.5 g/L D-glucose, 2.0 mM L-glutamine, 1% Penicillin/Streptomycin in 10 cm cell  
699 culture dishes. Cells were passaged every 2-3 days to reach confluence. Before splitting, culture  
700 media were removed and Dulbecco's phosphate-buffered saline (D-PBS) was used to rinse cell  
701 layers as well as removing residual serum. Cells were detached from dish with 4 ml of 0.05%  
702 Trypsin and incubated at 37°C until cell layer is dispersed (about 5 minutes). Equal volume of  
703 complete culture media was added to the dish to inhibit protease activity. The suspension was  
704 centrifuged at 200 x g for 5 minutes. Supernatant was aspirated and the cells were suspended  
705 with appropriate amount of media and plated (1:4-1:8). Cells used for experiments were  
706 passaged no more than 10 times. Cell stocks were stored as 2 million cells per vial in complete  
707 culture media with 10% DMSO in liquid nitrogen.

## 708 Identification of DS circuit cell types using antibody and transgenic markers

### 709 *SAC markers in mature retina*

710 Antibodies to choline acetyltransferase (ChAT) were used as a SAC marker in mice older  
711 than P5. This antibody stains SAC somata and their dendrites in the IPL (e.g. Fig. 8A).

### 712 *SAC markers in embryonic and neonatal retina*

713 Antibodies to ChAT and vesicular acetylcholine transporter, typically used as SAC  
714 markers in the mature retina, do not stain reliably in the embryonic and neonatal (P0-P3) mouse  
715 retina, precluding their use as markers during one of the key time periods of this study. We  
716 therefore characterized several other SAC markers that we found to be suitable for definitive  
717 SAC identification and their anatomical characterization in the E16-P3 period:

718 The *Megf10<sup>lacZ</sup>* allele (Kay et al., 2012) drives strong, selective  $\beta$ -galactosidase ( $\beta$ gal)  
719 expression in all SACs starting at embryonic day (E)17 (Fig. 1B; Fig. 1-Supplement 1; data not  
720 shown). Horizontal cells are also labeled. Expression is strong enough to allow characterization  
721 of SAC dendrite anatomy at these early stages. Antibodies to *Megf10* yield a similar staining  
722 pattern (Fig. 1-Supplement 1; Fig. 4B,C), but staining of fine dendritic arbors was brighter with  
723 anti- $\beta$ gal staining of *Megf10<sup>lacZ</sup>* mice, so this approach was used for most of our anatomical  
724 experiments analyzing the full SAC population at or before P3. In some such experiments a  
725 *Megf11<sup>lacZ</sup>* allele (Kay et al., 2012) was also present; this allele drives  $\beta$ gal expression in  
726 essentially the same pattern as *Megf10<sup>lacZ</sup>* and therefore contributed to signal brightness. The  
727 presence of this allele had no apparent effect on SAC anatomy, in either wild-type or *Megf10*  
728 mutant background.

729           Antibodies to Sox2 (Whitney et al., 2014) strongly label all SAC nuclei in the INL and  
730 GCL, starting at embryonic stages (Fig. 1-Supplement 1; Fig. 2D,E,G). Progenitor cells in the  
731 ONBL are also labeled. This marker was typically used in conjunction with *Megf10<sup>lacZ</sup>* to  
732 provide definitive identification of SACs as  $\beta\text{gal}^+\text{Sox2}^+$  cells.

733           Antibodies to internexin label SAC intermediate filaments, which localize in a polarized  
734 manner to the primary dendrite(s) and the side of the cell body from which they emerge (Fig. 2-  
735 Supplement 1). Primary dendrites were defined as any first-order dendrite branch, i.e. those  
736 arising directly from the cell body. Internexin is a selective marker of SAC in perinatal mouse  
737 retina, as previously shown in tree shrew (Knabe et al., 2007). RGC axons are also labeled (Fig.  
738 2-Supplement 1).

739           Antibodies to *Isl1* (Fig. 2A) label all SAC nuclei, starting at cell cycle exit (Galli-Resta et  
740 al., 1997). A large subset of RGCs are also labeled. The *Isl1<sup>Cre</sup>* knock-in mouse (Yang et al.,  
741 2006) faithfully recapitulated this expression pattern (Fig. 2A,B) and was used to study SAC  
742 anatomy at embryonic stages (see below for further details).

#### 743 *SAC single-cell labeling*

744           To assess the single-cell morphology of individual SACs during early postnatal  
745 development, the *Chat<sup>Cre</sup>* line was used. In contrast to mature retina (e.g. Fig. 8B), in which all  
746 SACs were labeled, *Chat<sup>Cre</sup>* expression was rare and sporadic in early postnatal retina (Fig. 1C;  
747 Fig. 1-Supplement 1), as reported previously (Xu et al., 2016). Therefore, when crossed with Cre  
748 reporter mice to make *Chat<sup>mG</sup>* animals, the full anatomy of individual SACs was clearly  
749 delineated (e.g. Fig. 2H-K). We did not typically observe Cre recombination in non-SAC cell

750 types; nevertheless, we always co-stained with another SAC marker, either Sox2 or *Megf10*: $\beta$ gal,  
751 to confirm the SAC identity of the cells that were analyzed.

#### 752 *ooDSGC markers*

753 Two mouse lines were used, each of which labels distinct types of ooDSGCs. *Hb1x9-GFP*  
754 (referred to as Hb9-GFP throughout the manuscript) labels the superior subtype of ooDSGC,  
755 while *Drd4-GFP* labels the posterior subtype of ooDSGC (Trenholm et al., 2011; Huberman et  
756 al., 2009).

#### 757 *DS-circuit bipolar cell markers*

758 Four types of bipolar cells have been shown to make monosynaptic connections with  
759 SACs and/or ooDSGCs: Types BC2, BC3a, BC5, and BC7 (Duan et al., 2014; Ding et al., 2016;  
760 Greene et al., 2016; Kim et al., 2014; Chen et al., 2014). OFF bipolar cells BC2 and BC3a were  
761 labeled, respectively, by antibodies to Syt2 and HCN4 (Wässle et al., 2009).

762 ON bipolar cells BC5 and BC7 were marked with *Kcng4*<sup>Cre</sup> (Duan et al., 2014) crossed to  
763 mGFP Cre reporter mice (denoted *Kcng4*<sup>mG</sup>). Labeling of BC7 was more prominent with the  
764 Rosa26 locus mGFP Cre reporter line that we used, compared to the cytosolic GFP reporter  
765 driven by Thy1 that was used by Duan et al. (2014).

766 *Gjd2-GFP* was also used to label BC5 bipolar cells (Fig. 11-Supplement 1). In adult  
767 retina, GFP was strongly expressed by a bipolar cell type that ramified in a laminar location  
768 typical of BC5 (Sidney Kuo, University of Washington, personal communication). We  
769 confirmed this expression pattern; weak expression in amacrine cells was also noted (Fig. 11-  
770 Supplement 1). At earlier developmental stages the amacrine cell staining was much stronger and

771 filled many amacrine processes throughout the IPL, precluding use of this line for developmental  
772 studies of bipolar axons (M. Stogsdill and J.N.K, unpublished observations).

### 773 **Immunohistochemistry**

#### 774 *Retinal cross sections:*

775 Mice were anesthetized by isoflurane or cryoanesthesia (neonates only) followed by  
776 decapitation. Eyes were enucleated, washed in PBS, and fixed in PBS containing 4%  
777 formaldehyde (pH 7.5) for 1.5 hours at 4° C. After fixation, eyes were washed 3X with PBS and  
778 stored in PBS containing 0.02% sodium azide at 4° C until further processing. Retinas were  
779 dissected from the eyecup, cryoprotected by equilibration in PBS containing 30% sucrose, then  
780 embedded in Tissue Freezing Medium and frozen by submersion in 2-methylbutane chilled by  
781 dry ice. Tissue sections were cut on a cryostat to 20 µm and mounted on Superfrost Plus slides.  
782 Slides were dried on a slide warmer for 1 h then stored at -80° C or used immediately.

783 For antibody labeling, slides were washed for 5 min with gentle agitation in PBS to  
784 remove embedding medium and blocked for 1 h in PBS + 0.3% Triton X-100 (PBS-Tx)  
785 containing 3-5% normal donkey serum. Primary antibodies were diluted in blocking buffer,  
786 added to slides, then incubated overnight at 4° C. Slides were washed with PBS 3X for 10  
787 minutes followed by incubation with secondary antibody diluted in PBS-Tx for 1-2 h at RT.  
788 Slides were washed again with PBS 3X for 10 minutes then coverslipped using Fluoromount G.

#### 789 *Retinal whole-mounts:*

790 Tissue was processed as above up to the point of dissection from the eyecup. After  
791 dissection from eyecup, retinas were washed in PBS then blocked for 3 hours with agitation at 4°  
792 C in blocking buffer (constituted as described above). Primary antibodies were diluted in

793 blocking buffer, added to retinas, and incubated for 5-7 days with gentle agitation at 4°C. Retinas  
794 were washed 3X with PBS over the course of 2 hours with gentle agitation. Secondary antibody  
795 was diluted in PBS containing 0.3% Triton X-100 and was added to retinas followed by  
796 incubation overnight at 4° C with gentle agitation. Retinas were washed again 3X in PBS over  
797 the course of 2 hours with gentle agitation. For mounting on slides, 4 radial incisions separated  
798 by 90° were made centripetally, approximately 1/3 the radius of the retina. Retinas were flattened  
799 on nitrocellulose paper photoreceptor side down and coverslipped with Fluoromount G.

#### 800 *Image acquisition and processing*

801       Sections and whole-mounts were imaged on a Nikon A1 or an Olympus FV300 confocal  
802 microscope. Image Z-stacks (Z-resolution 0.4 - 0.5 µm for whole-mount images; 0.8 - 1.0 µm for  
803 cross-sections) were imported to Fiji (Schindelin et al., 2012), de-noised by median-filtering (0.5  
804 - 2.0 pixel radius), and projected to a single plane. The portion of the stack selected for  
805 maximum-intensity projection was determined by the Z-volume of the structure to be depicted in  
806 the final image. Except where noted, data analysis and quantification was only performed using  
807 original stacks, not Z-projections. Color channels were assembled, and minor adjustments to  
808 brightness and contrast were made, in Adobe Photoshop. When images were to be compared,  
809 equivalent adjustments were performed on all images in the experiment. The width of the IPL is  
810 marked in many of the figures; this was determined by one of the following methods: 1)  
811 counterstaining with Hoechst to label all cell nuclei; 2) tdTomato fluorescence from  
812 unrecombined cells in *mT/mG* mice, which fills the IPL; 3) immunofluorescence against GAD65,  
813 which also fills the IPL; 4) autofluorescence signal intensity differences between soma layers  
814 and IPL.

## 815 Analysis of SAC anatomy in embryonic retina

816 To study SAC anatomy during embryonic stages, *Isl1<sup>Cre</sup>* was crossed to *lox-stop-lox-*  
817 *mGFP* Cre reporter mice (*mT/mG* or *Rosa26<sup>GFPf</sup>*; see Key Reagents) to generate *Isl1<sup>mG</sup>* animals.  
818 Timed-pregnant dams were sacrificed at E16 and eyes collected from embryos ( $n = 11$  mice  
819 from 3 litters). Tissue was processed as described for postnatal eyes, except fixation time was 60  
820 min. Cross-sections were stained with anti-GFP to reveal the morphology of *Isl1<sup>mG</sup>*-expressing  
821 neurons, as well as Sox2 to distinguish *Isl1<sup>mG</sup>*-positive SACs from RGCs. (All cells shown in Fig.  
822 2B-G were confirmed to be SACs by Sox2 co-labeling.) In combination with these markers, anti-  
823 internexin staining was used to assess orientation of primary dendrites. Location and/or presence  
824 of the IPL was determined using Hoechst nuclear staining, which revealed cell body-free  
825 neuropil regions, and/or by *Isl1<sup>mG</sup>* labeling of neuronal processes, which filled these neuropil  
826 regions (Fig. 2-Supplement 2). We assessed anatomy of mGFP<sup>+</sup> migrating SACs in the ONBL,  
827 as well as SACs in the INBL that were concluding their migration. Morphology of ON SACs in  
828 the GCL could not be discerned due to *Isl1* expression by RGCs (Fig. 2A,B), but because  
829 displaced amacrine cells pause at the INL-IPL border before crossing to the GCL (Chow et al.,  
830 2015), the population of cells available to analyze might have included both ON and OFF SACs.

831 To measure the orientation of primary dendrites at E16 and P1, the angle ROI function in  
832 ImageJ was used. This function outputs an angle degree measurement (absolute value) between  
833 two line segments. The first line segment of the angle was drawn to follow the trajectory of the  
834 internexin<sup>+</sup> primary dendrite; the endpoint was at the cell body. The second line segment of the  
835 angle was a plumb line to the IPL (i.e. it was drawn to intersect the IPL at  $\sim 90^\circ$ ). As such,  
836 dendrites oriented exactly towards the IPL were assigned an angle of  $0^\circ$ . At E16 the IPL was  
837 occasionally not present yet; in this case the second line segment was a plumb line to the inner

838 limiting membrane. In cases where the internexin<sup>+</sup> dendrite curved, we traced the initial  
839 trajectory of the dendrite as it emerged from the cell body. Dendrites were classified as  
840 projecting 1) towards the IPL; 2) towards the ONBL; or 3) tangentially, according to the angle  
841 scheme delineated in Fig. 2-Supplement 1E. Image stacks were randomly selected for analysis  
842 from a larger library of images; within each selected stack every SAC was traced. *Isl1<sup>mG</sup>* and  
843 *Sox2* were used to confirm the SAC identity of each measured cell, as well as the trajectory of  
844 the internexin<sup>+</sup> dendrite.

#### 845 **Characterization of SAC homotypic arbor network in soma layers**

846 The homotypic nature of SAC soma-layer contacts was investigated by imaging single  
847 *Chat<sup>mG</sup>*-labeled OFF SACs in mice also carrying a single copy of the *Megf10<sup>lacZ</sup>* allele (Fig. 2I,J).  
848 Anti-βgal staining was used to reveal the full SAC population, including arbors. *En-face* images  
849 were captured in Z-stacks spanning the INL and IPL; slices corresponding to each layer were  
850 separately Z-projected for display in Fig. 2 and Fig. 2-Supplement 3. To quantify the frequency  
851 of SAC-SAC contacts, we used Z-stacks from P1 tissue to examine the trajectory and  
852 termination site of each dendritic tip in three dimensions. The fraction of *Chat<sup>mG</sup>*-labeled  
853 dendrites terminating on the βgal-positive soma or arbor of a neighboring SAC was quantified.  
854 To be counted, the putative contact needed to be confirmed in a single Z-stack slice; where  
855 necessary, 3D reconstructions and orthogonal views were used to confirm contact.

856 We also performed the same analysis on Z-stacks in which one channel had been flipped  
857 about the horizontal and vertical axes. This served as a negative control to measure the frequency  
858 with which GFP and βgal arbors interact by chance, given their density and geometry in the P1  
859 retina. Sample sizes are given in main text and in Fig. 2-Supplement 3.

## 860 **Generation and analysis of “solitary” SACs**

### 861 *Reduction of SAC density using Ptf1a<sup>lox</sup> mice*

862 *Ptf1a<sup>lox</sup>* mutant mice (Krah et al., 2015) were crossed into the *Six3-Cre* background to  
863 generate *Ptf1a*-cKO mice. *Six3-Cre* is expressed by retinal progenitors starting at E9.5 in a high-  
864 central-to-low-peripheral gradient (Furuta et al., 2000; Fig. 3A). In central retina, where Cre is  
865 expressed in all progenitors, amacrine cells were completely absent but bipolar cells, RGCs,  
866 Müller glia, and photoreceptors remained (Fig. 3B; Fig. 3-Supplement 1; data not shown). In  
867 peripheral retina, where Cre recombination was incomplete, amacrine cells derived only from  
868 Cre-negative progenitors (Fig. 3C). Because the number of Cre-expressing progenitors in  
869 peripheral retina still vastly exceeded the number that escaped Cre, amacrine cell density in  
870 *Ptf1a*-cKO peripheral retina was markedly reduced compared to littermate controls (Fig. 3A,B;  
871 Fig. 3-Supplement 1).

### 872 *Quantification of dendrite phenotypes in solitary and touching SACs*

873 To visualize SACs and quantify their arbor targeting frequencies in *Ptf1a*-cKO mice, we  
874 bred *Megf10<sup>lacZ</sup>* into the *Ptf1a<sup>lox</sup>* background. All *Ptf1a*-cKO and littermate control mice in these  
875 experiments carried one copy of the *Megf10<sup>lacZ</sup>* allele. SAC morphology was revealed with anti-  
876  $\beta$ gal. *Sox2* was used to confirm the SAC identity of all cells included in the experiment. SACs  
877 were scored as “solitary” or “touching” based on whether their dendrites contacted neighboring  
878 SACs in the same or adjacent sections. If this could not be determined (e.g. because the adjacent  
879 section was missing or damaged), the cell was excluded from further analysis. Because SACs  
880 were only present in *Ptf1a*-cKO peripheral retina, analysis of littermate control SACs was also  
881 limited to peripheral retina. In *Ptf1a*-cKO mice, SACs were more frequently found in the INL

882 than the GCL and it is possible that the INL SACs were a mixed population of ONs and OFFs.  
883 Therefore, we did not distinguish between SAC subtypes for the analyses.

884 IPL projections of  $\beta$ gal-stained cells were examined, and cells were assigned to one of  
885 three categories: 1) no arbors projecting to the IPL; 2) Arbors enter the IPL but fail to stratify; 3)  
886 Arbors enter the IPL and ramify in a laminar pattern. Examples of the first category of solitary  
887 SACs are shown in Fig. 3F, left, and Fig. 3-Supplement 1. Examples of the second category are  
888 shown in Fig. 3F, right, and Fig. 3-Supplement 1. The third category is exemplified by all  
889 touching SACs shown (Fig. 3E; Fig. 3-Supplement 1). Each cell in the dataset was also scored  
890 on an independent criterion: whether it projected to the soma layer (e.g. Fig. 3D,F, white arrows).

891 For each animal in the experiment, the following was calculated and plotted in Fig. 3G:  
892 1) Percentage of SACs with projections to the soma layers; 2) percentage of SACs projecting to  
893 the IPL (i.e., the cells assigned to categories 2 and 3 above); 3) percentage of SACs with  
894 stratified IPL dendrites (i.e. the cells in category 3). Sample sizes:  $n = 3$  wild-type littermates  
895 (28, 62, 32 cells analyzed in each animal);  $n = 4$  *Ptf1a*-cKO animals (11, 35, 13, 12 solitary and  
896 27, 44, 22, 23 touching SACs analyzed in each animal). Statistics: one-way ANOVA with  
897 Tukey's post-hoc test.

### 898 **Quantification of SAC projection phenotypes in *Chat<sup>mG</sup>* mice**

899 Single SACs labeled in *Chat<sup>mG</sup>* and *Chat<sup>mG</sup>;Mef10<sup>-/-</sup>* mice were morphologically  
900 assessed in cross-sections. GFP signal was amplified with anti-GFP antibody staining. All GFP<sup>+</sup>  
901 SACs on any given slide were imaged and analyzed, to avoid cell selection bias, with the  
902 exceptions of: 1) cells severed by the cryosectioning process; 2) cells with arbors that could not  
903 clearly be distinguished from those of their neighbors; 3) cells in the far retinal periphery, where

904 sections were oblique to retinal layers, obscuring IPL strata. In experiments analyzing *Megf10*  
905 mutants, littermates were always used as controls to avoid complications arising from the fact  
906 that the precise state of retinal development at the time of birth might vary from litter to litter.

907         A cell was scored as innervating the IPL if it ramified branched dendrites within the  
908 neuropil. Dendrites that entered the neuropil but did not branch or stratify (e.g. Fig. 6D) were not  
909 sufficient. A cell was scored as projecting to the soma layer if arbors emanating from the cell  
910 soma or primary dendrite terminated or arborized in the INL (for OFF SACs) or GCL (for ON  
911 SACs). The arbor was required to be  $\sim \geq 1$  cell diameter in length (i.e. small fine arbors were not  
912 counted). One other important exception that was not counted: We observed that many SACs at  
913 young ages had single unbranched arbors extending  $\sim 180^\circ$  away from the IPL (e.g. Fig. 2J,K –  
914 all four cells have such arbors, even the ones that do not project towards neighboring SAC  
915 somata). These processes were not counted for two reasons. First, their trajectory was such that  
916 they were unlikely to join the soma-layer dendrite network or contact neighboring somata.  
917 Second, these  $180^\circ$  arbors were sometimes still present in P5 SACs (Fig. 2-Supplement 2) and  
918 therefore they did not appear to be subject to the same developmental regulation as tangentially-  
919 directed arbors (Fig. 2L). This observation suggests they are fundamentally different, and likely  
920 serve a different (as yet uncharacterized) purpose. No obvious difference in their frequency was  
921 observed between wild-type and *Megf10* mutants.

922         To produce graphs in Figs. 2L, 6E, and 8F, the fraction of cells making ectopic  
923 projections – either to the soma layer or to inappropriate IPL sublayers – was calculated for each  
924 genotype and each time point. To determine whether a GFP+ IPL arbor was located in normal or  
925 abnormal IPL strata, *Megf10*: $\beta$ gal was used as a counterstain. *Chat*<sup>Cre</sup> was rarely expressed in  
926 OFF SACs at P0, making it difficult to obtain large sample sizes at this age. For this reason, and

927 because soma-layer projection frequency did not appear to differ much between P0 and P1, the  
 928 data from each time point was pooled for analysis of *Megf10* litters.

929 Sample sizes for Fig. 2M: P0,  $n = 25$  OFF, 63 ON; P1,  $n = 51$  OFF, 79 ON; P2,  $n = 46$   
 930 OFF, 55 ON; P3,  $n = 33$  OFF, 49 ON; P5,  $n = 15$  OFF, 26 ON; P7,  $n = 23$  OFF, 34 ON. Data  
 931 were from four litters of mice, each of which was assessed at no less than two of these time  
 932 points.

933 Sample sizes for *Megf10*; *Chat*<sup>mG</sup> experiments (Figs. 5F, 7G): *Megf10* heterozygous  
 934 littermate controls: P0/1,  $n = 11$  OFF, 25 ON; P2,  $n = 25$  OFF, 23 ON; P3,  $n = 17$  OFF, 22, ON;  
 935 P5,  $n = 16$  OFF, 16 ON. *Megf10* mutants: P0/1,  $n = 6$  OFF, 25 ON; P2,  $n = 14$  OFF, 20 ON; P3,  
 936  $n = 34$  OFF, 41 ON; P5,  $n = 48$  OFF, 54 ON. Data were from two litters of mice.

937 For the adult data reported in Fig. 8F, a different procedure was used; see “Quantification  
 938 of Mosaic Spacing Phenotypes” section below.

### 939 **Analysis of Chat-Megf10-cKO conditional mutants**

#### 940 *Characterization of timing of MEGF10 deletion*

941 For initial characterization of when MEGF10 protein is eliminated by the *Chat*<sup>Cre</sup> driver  
 942 line, the following experiment was performed: *Chat*<sup>Cre</sup>; *Megf10*<sup>lox</sup> mice were intercrossed with  
 943 *Chat*<sup>Cre</sup>; *Megf10*<sup>lacZ</sup> carriers to generate *Chat*<sup>Cre</sup>; *Megf10*<sup>lox/lacZ</sup> (Chat-Megf10-cKO) experimental  
 944 animals and littermate controls (*Chat*<sup>Cre</sup>; *Megf10*<sup>lox/+</sup>). These animals also carried a *Rosa26*  
 945 mGFP Cre reporter allele. Animals were sacrificed at P1, P3, and P5; retinas were cross-  
 946 sectioned and immunostained for anti-MEGF10 (Fig. 6-Supplement 1). Comparisons were made  
 947 across animals from the same litter to assess how MEGF10 immunoreactivity changed over time.  
 948 Two litters were analyzed in this way, each yielding the same conclusion: MEGF10

949 immunoreactivity was largely eliminated by P5 in Chat-Megf10-cKO mice (Fig. 6-Supplement  
950 1). At P3, overall MEGF10 levels were reduced, but most SACs still expressed detectable  
951 protein (Fig. 6-Supplement 1). The cells that lost MEGF10 immunoreactivity by P3 were not  
952 necessarily the same cells that recombined the mGFP reporter at the *Rosa26* locus (Fig. 6F,G).  
953 At P1, only a very small number of cells (< 5 per retina) could be identified that lacked MEGF10  
954 immunoreactivity; most of these were ON SACs although a few recombined OFF SACs were  
955 identified (Fig. 6G). We conclude that a small fraction of SACs loses MEGF10 protein prior to  
956 P3, while the majority lose MEGF10 between P3 and P5. Further, ON SACs are somewhat more  
957 likely to lose MEGF10 before P3 than OFF SACs.

#### 958 *Assessment of morphological and IPL projection phenotypes*

959 To ask if loss of MEGF10 prior to P3 affects dendritic targeting, *Chat<sup>mG</sup>*-labeled single  
960 SACs were identified in retinal cross-sections from Chat-Megf10-cKO and *Chat<sup>Cre</sup>; Megf10<sup>lox/+</sup>*  
961 control mice, as described above. Analysis was performed at P1 and P3; data in Fig. 6H is from  
962 P3 only. All mGFP<sup>+</sup> SACs were first scored as to whether they expressed MEGF10 protein (see  
963 Fig. 6F,G). Subsequently, each cell was scored for soma-layer projection as described above for  
964 wild-type and *Megf10<sup>-/-</sup>* animals. This scoring was done blind to the cell's MEGF10 expression  
965 status. The fraction of cells classified as either "soma-projecting" or "IPL-only" was calculated  
966 for MEGF10<sup>+</sup> SACs, MEGF10<sup>-</sup> SACs, and littermate control SACs (Fig. 6H). Sample sizes: *n* =  
967 26 OFF, 18 ON cells from controls; 24 OFF, 19 ON MEGF10<sup>+</sup> cells from Chat-Megf10-cKO; 9  
968 OFF, 17 ON MEGF10<sup>-</sup> cells from Chat-Megf10-cKO.

969 To assess SAC stratification at maturity, cross-sections from P17 Chat-Megf10-cKO and  
970 littermate controls were stained for anti-ChAT. Four mutants and three littermate controls, from  
971 two litters, were examined.

## 972 **Analysis of Six3-Megf10-cKO conditional mutants**

### 973 *Characterization of Cre recombination patterns*

974 Breeders carrying the relevant alleles were interbred to generate *Six3-Cre; Megf10<sup>lox/lacZ</sup>*  
975 (*Six3 Megf10<sup>cKO</sup>*) mice and littermate controls (*Six3-Cre; Megf10<sup>+ /lacZ</sup>* or *Cre<sup>-</sup> Megf10<sup>lox/lacZ</sup>*). As  
976 noted above in *Ptfla* section, Cre is expressed very early (~E9.5) in *Six3-Cre* retina, but  
977 expression is incomplete, with some parts of peripheral retina spared from Cre activity (Furuta et  
978 al., 2000). Therefore, all mice used for these experiments also carried the *Rosa26<sup>GFPf</sup>* Cre  
979 reporter, to reveal retinal regions that either lacked MEGF10 (GFP<sup>+</sup> cells) or were spared from  
980 MEGF10 deletion (GFP<sup>-</sup> cells). Anti-MEGF10 staining confirmed that the GFP Cre reporter is a  
981 reliable marker of MEGF10 expression status (Fig. 6-Supplement 1).

### 982 *Assessment of morphological phenotypes*

983 For quantification of INL projection frequency at P2, *Six3 Megf10<sup>cKO</sup>* and littermate  
984 control whole-mount retinas were stained for  $\beta$ gal, Sox2, and anti-GFP. This staining marked  
985 SACs (Sox2 and  $\beta$ gal), revealed their dendritic morphology ( $\beta$ gal), and defined their MEGF10  
986 expression status (GFP). Confocal stacks were acquired through the INL, extending to the IPL  
987 (which was clearly discernable due to dense  $\beta$ gal and GFP expression). The INL was defined as  
988 the region above this in the image stack, containing Sox2<sup>+</sup> neurons. Cells that projected into the  
989 INL were clearly discernable due to their multipolar morphology with numerous dendritic  
990 protrusions (e.g. Fig. 7B). Cells that did not project to the INL had a round morphology with  
991 only minor lateral branches less than one cell radius in length (Fig. 7C). Each  $\beta$ gal-labeled SAC  
992 was scored as to whether it expressed GFP, and whether it projected lateral arbors into the INL.  
993 If the cell had only INL branches directed towards the IPL through the stack Z-plane, it was not

994 counted as INL-projecting. Scoring was done in separate sessions so that the scorer was blind to  
995 GFP expression status when determining INL projections. Sample sizes:  $n = 117$  SACs from 2  
996 control mice;  $n = 302$  GFP<sup>+</sup> SACs and 149 GFP<sup>-</sup> SACs from 2 Six3-Megf10-cKO mice.

997       To assess SAC stratification in cross-sections, P2, P4, or P17 Six3-Megf10-cKO and  
998 littermate control retinas were sectioned and stained for anti-βgal (P2) or anti-ChAT (P17). The  
999 number of animals examined was: P2, 4 mutants, 2 controls; P4, 2 mutants, 3 controls; P17, 2  
1000 mutants, 2 controls.

### 1001 **Quantification of area covered by SAC dendritic arbors**

#### 1002 *Neonatal individual SAC arbor territory*

1003       P0 *Chat<sup>mG</sup>* retinas were imaged in whole-mount preparations stained with anti-Sox2 and  
1004 anti-GFP antibodies to identify single GFP<sup>+</sup> SACs. To avoid cell selection biases, all labeled  
1005 SACs with arbors that were clearly distinguishable from their neighbors were imaged and  
1006 analyzed, except for far-peripheral cells that may have been damaged during mounting. At least  
1007 4 animals were imaged for each genotype. Z stacks were acquired through the GCL, IPL, and  
1008 INL to encompass all arbors of a single cell. Images were imported into ImageJ, z-projected into  
1009 a single plane, and polygons were drawn connecting the dendritic tips, nearest neighbor to  
1010 nearest neighbor, until the dendritic field was captured. Area of this polygon was calculated  
1011 using ImageJ. Sample sizes: OFF SACs,  $n = 16$  wild-type and 16 *Megf10<sup>-/-</sup>*; ON SACs,  $n = 31$   
1012 wild-type and 34 *Megf10<sup>-/-</sup>*. Statistics: two-tailed *t*-tests.

1013 *Adult individual SAC arbor territory*

1014 Individual SACs were labeled by injection of *Chat<sup>Cre</sup>* mice with “Brainbow” Adeno-  
1015 associated virus (AAV) driving fluorophore expression in a Cre-dependent manner (Cai et al.,  
1016 2013). The two Brainbow AAV9 viruses, encoding farnesylated fluorescent proteins that are  
1017 targeted to the plasma membrane (University of Pennsylvania Vector Core), were mixed to 1.5 x  
1018 10<sup>12</sup> genome copies per mL. Adult mice (P40-50) were anesthetized with ketamine-xylazine by  
1019 intraperitoneal injection. Proparacaine hydrochloride (0.5%) ophthalmic solution (Akorn, Lake  
1020 Forest, IL) was applied to the eye to provide local anesthesia. A 30 1/2G needle was used to  
1021 make a small opening near the ora serrata, and 1µl of virus was injected with a 33G blunt-ended  
1022 Hamilton syringe intravitreally. Tissue was collected 3 weeks after the virus injection.

1023 Retinas were stained in whole-mount with anti-GFP, anti-mCherry, and anti-mKate  
1024 antibodies to reveal SACs. OFF SACs were not labeled in large numbers, so analysis was  
1025 restricted to more abundantly labeled ON SACs. Imaging, image processing, and quantification  
1026 were as for P0, except that only SACs in central and mid-peripheral retina were used to avoid  
1027 confounding effects of eccentricity on arbor size. Sample sizes: *n* = 10 wild-type and 16 *Megf10*  
1028 mutant SACs.

1029 *ChAT+ arbor plexus retinal coverage*

1030 *En-face* images of adult (P46) ON or OFF SAC plexus were obtained from confocal Z-  
1031 stacks (0.4 µm Z resolution) by performing maximum-intensity Z-projections of 2-4 optical  
1032 slices encompassing the relevant layer. Using ImageJ, these images were then thresholded,  
1033 converted to binary, and the percentage of the field of view covered by ChAT-positive arbors  
1034 was calculated. All image stacks were obtained from central or mid-peripheral retina. Sample  
1035 size: 9 fields of view from 2 *Megf10* mutants and 2 heterozygous littermate controls were used to

1036 calculate average coverage for each genotype. Percent change is reported in the Results; total  
1037 retinal coverage was as follows: Control ON,  $65.9 \pm 1.3$  %; control OFF,  $70.6 \pm 3.6$ %; mutant  
1038 ON  $56.9 \pm 3.8$ %; mutant OFF,  $60.0 \pm 3.7$ % (mean  $\pm$  S.D).

### 1039 **Hb9-GFP stratification**

1040 P1-P2 retinas carrying *Megf10<sup>lacZ</sup>* and Hb9-GFP were co-stained for  $\beta$ gal and GFP. RGCs  
1041 with dendrites that co-fasciculated with  $\beta$ gal-positive IPL strata were counted. Cells that  
1042 projected to  $\beta$ gal-positive regions, but also filled non-SAC-projecting IPL regions, were not  
1043 counted as co-fasciculated. To judge co-fasciculation, we used 2 criteria: 1) inspection of  
1044 dendrite anatomy across the confocal stack; 2) fluorescence profiles of GFP and  $\beta$ gal channels  
1045 across IPL (see next section below). Examples of cells falling into each category are provided in  
1046 Fig. 1 and Fig. 1-Supplement 2. See Results for sample sizes.

### 1047 **Quantitative assessment of IPL stratification level**

1048 Images of retinal cross sections were processed in ImageJ. A vertical ROI ( $12.5 \mu\text{m}$   
1049 wide) was drawn to perpendicularly bisect the IPL strata, from the edge of the INL to the edge of  
1050 the GCL. IPL stratification levels were reported as percentage of IPL width. Intensity was  
1051 calculated for each pixel along the length of the ROI as an average across its width. Background  
1052 (minimum pixel value) was subtracted; then, all pixel intensity values were normalized to the  
1053 maximum value of that ROI. Location of fluorescent peaks was calculated as the pixel with  
1054 maximum intensity; if multiple pixels had the same intensity the peak was defined as the center  
1055 of the plateau. The procedure was typically performed on single confocal optical sections, but for  
1056 some P1-2 cells, which have much smaller arbors, it was necessary to use a maximum-intensity  
1057 projection of a small number of slices in order to fully capture dendrite morphology.

1058 For BC5-BC7 arbor distance measurements (Fig. 9F), distances as percentage of total IPL  
1059 width were compared by one-way ANOVA/Tukey's post-hoc test.  $n = 14$  measurements from 2  
1060 control mice;  $n = 7$  normal IPLs, 11 SAC clumps, 11 SAC gaps from 3 *Megf10*<sup>-/-</sup> mice.

### 1061 **Generation of Megf10-ΔICD Constructs**

1062 The MEGF10-ΔICD-GFP construct was reported previously (Kay et al., 2012), which  
1063 was originally made from pUbC-MEGF10-GFP (Addgene #40207). It encodes a version of  
1064 MEGF10 in which the cytoplasmic domain is truncated after the 9<sup>th</sup> amino acid and replaced by  
1065 GFP. Inclusion of those 9 amino acids was necessary to achieve plasma membrane localization.  
1066 For this study it was subcloned into the pEGFPN3 plasmid, containing the CMV promoter, to  
1067 make pCMV-MEGF10-ΔICD-GFP.

1068 To make the MEGF10-ΔICD-Flag construct, Megf10 (truncated after the 9<sup>th</sup> intracellular  
1069 domain amino acid as above) was PCR amplified from pUbC-MEGF10-GFP vector using  
1070 M10flag\_Fwd forward primer and Cyto9\_flag\_Rev1 reverse primer. Resulting PCR products  
1071 were digested with NotI and AscI restriction enzymes and ligation cloned into pEGFPN3 vector  
1072 linearized with corresponding restriction enzymes.

### 1073 **Assay for interaction of MEGF10-ΔICD constructs**

#### 1074 *Co-Immunoprecipitation*

1075 HEK293T cells were grown to 80% confluency. Cells were then transfected using a  
1076 linear polyethylenimine (PEI) transfection reagent: DNA, PEI, and Opti-MEM were mixed in a  
1077 1:3:30 ratio and incubated for 10 minutes at room temperature then applied to confluent cells.  
1078 Cells were harvested 48-hour post transfection. Cells were lysed with NP-40 lysis buffer (1%

1079 NP-40, 150mM NaCl, 50mM Tris-Cl, and 1X proteinase inhibitor) by pipetting. Lysate was  
1080 centrifuged at 14000 x g at 4°C for 15 min. to remove insoluble material. The soluble protein  
1081 fraction was quantified with Bio-Rad DC assay. For immunoprecipitation, 500µl (1µg/ µl)  
1082 protein in NP-40 buffer lysis buffer was incubated overnight at 4°C with antibody (1µl of  
1083 chicken anti-GFP or 2µl of mouse anti-Flag). Protein G Dynabeads (10µl) were added to mixture  
1084 for 1 hour at 4°C while rotating. Beads were sequestered by magnet and flow-through was  
1085 removed. Beads were washed with 500µl lysis buffer (3x) on ice then eluted with 30µl 2X  
1086 Laemmli containing 5% β-mercaptoethanol.

#### 1087 *Western Blot*

1088         Samples were prepared in 2X Laemmli sample buffer, heated at 95°C for 10 minutes, and  
1089 loaded onto SDS-acrylamide gel (running gel: 8% acrylamide/bis Tris-HCl with 0.1% SDS pH  
1090 8.8; stacking gel: 5% acrylamide pH 6.8; cross linked with TEMED and APS). Precision Plus  
1091 Protein Dual Color Standards (BioRad) were used as a molecular weight marker. The gel was  
1092 run on a BioRad mini gel running apparatus with SDS-PAGE running buffer (25 mM Tris, 192  
1093 mM glycine, 0.1% SDS). Electrophoresis was carried out at 50 V through the stacking gel then  
1094 adjusted to 120 V until the dye front reached the lower end of the gel. BioRad Immobilon-FL  
1095 PVDF membrane and Whatman filter paper were used with the BioRad mini cassette for transfer.  
1096 Samples were transferred in 25 mM Tris, 192 mM glycine, 20% methanol at 100 V for 90  
1097 minutes. Membranes were blocked with PBS/Odyssey blocking buffer and stained with chicken  
1098 anti-GFP 1:20000, mouse anti FLAG 1:20000 overnight at 4°C with shaking. After washing with  
1099 PBST for 4 times, membranes were stained with 1:20000 secondary antibodies for one hour at  
1100 room temperature. The membranes were washed with PBST four times and then rinsed with PBS

1101 and water. Finally, the membranes were imaged with LI-COR Odyssey using the Image Studio  
1102 software.

### 1103 **Quantification of mosaic spacing phenotypes and their effects on SAC IPL projections**

#### 1104 *Regularity index*

1105 Regularity of SAC cell body distribution in Six3-Megf10-cKO, Chat-Megf10-cKO, and  
1106 littermate control mice was calculated as previously described (Kay et al., 2012). The Voronoi  
1107 domain regularity index (VDRI) was used as a measure of regularity. It is calculated by first  
1108 assigning a Voronoi domain to each cell in an array (Fig. 9-Supplement 1), and then calculating  
1109 the mean and standard deviation of the domain areas. The VDRI is defined as the mean area  
1110 divided by the standard deviation. Arrays that are less regularly distributed will have a lower  
1111 VDRI because their domain sizes are more variable (and hence have a higher standard deviation).

1112 P17 whole-mount retinas were stained with an antibody to ChAT and imaged *en face*.  
1113 One eye was processed from each animal used in the experiment. For each eye, 3 confocal image  
1114 stacks were obtained using a 20x objective (636.5  $\mu\text{m}^2$  field of view). Images of INL SACs were  
1115 analyzed using Fiji software. The location of each SAC in the field of view was marked; this  
1116 information was used to count the number of SACs (Fig. 9B) as well as define Voronoi domains  
1117 belonging to each cell, using Fiji functions. The area of each Voronoi domain (excluding edges)  
1118 was calculated in Fiji.

1119 For statistical analysis of regularity effects across genotypes, we first calculated the per-  
1120 animal average cell density and VDRI from the 3 acquired images. Differences between  
1121 genotypes were then evaluated using one-way ANOVA and Fisher's PLSD. Previously  
1122 published *Megf10* null and simulation data was also included for comparison (Kay et al., 2012).

1123 The simulations define the VDRI that would be expected for a randomly-arranged array of cells  
1124 matched in size and density to real SACs. Data collection and analysis was virtually the same as  
1125 in the previous study, allowing us to include these data in our statistical comparisons.

1126 *Effects of soma position upon IPL errors: Single-cell analysis*

1127 To ask if soma position correlates with IPL errors, we first defined the ectopic projection  
1128 status of each OFF SAC in a set of Z-stacks acquired from ChAT-immunostained retinal whole-  
1129 mounts. Sample sizes:  $n = 515$  cells from 2 control (*Megf10*<sup>+/-</sup>) mice;  $n = 584$  cells from 2  
1130 *Megf10* mutant mice. The Z-stacks encompassed, at different levels of the stack, SAC somata in  
1131 the INL and their ramified arbors in the IPL. In *Megf10* mutants, the OFF ectopic IPL arbor  
1132 network and the typical OFF DS circuit sublayer were identified at different stack levels (Fig.  
1133 8C,E). ChAT<sup>+</sup> arbors arising from individual OFF SAC somata were traced through the stack to  
1134 identify those that joined into the ectopic network. The fraction of SACs that did so was then  
1135 calculated and plotted in Fig. 8F. For Fig. 8G, we further examined these stacks to look for SACs  
1136 that made ectopic projections at the INL level.

1137 Next, we defined the severity of mosaic spacing perturbations in the local neighborhood  
1138 of each SAC. Because SAC position is random in *Megf10* mutants, SACs might be more  
1139 crowded or more isolated from their neighbors than in controls; or, by chance, they might be  
1140 located at a fairly normal distance from their neighbors. The size of a cell's Voronoi domain is  
1141 influenced by the distance of all nearest neighbors (Fig. 9-Supplement 1), and therefore serves as  
1142 a convenient measure of local cell density. For simplicity we refer to Voronoi domains as  
1143 "territory size" in Fig. 9-Supplement 1. The effect of local cell density upon IPL projection  
1144 errors was determined by plotting the ectopic error rate for each 100  $\mu\text{m}^2$  territory size bin (Fig.

1145 8D,F). Sample size per bin, in order from smallest ( $<200 \mu\text{m}^2$ ) to largest ( $>1100 \mu\text{m}^2$ ):  $n = 32$ ,  
1146 65, 89, 102, 91, 80, 30, 39, 24, 34.

### 1147 **Multielectrode array recordings**

#### 1148 *Isolation of retina, recording, and spike sorting*

1149 Two wild-type and two *Megf10*<sup>-/-</sup> animals were used for multielectrode array (MEA)  
1150 recordings. Immediately following euthanasia, retinas were isolated under infrared (IR,  $>900$   
1151 nm) illumination with the assistance of IR-to-visual converters. This preserved the  
1152 photosensitivity of the retina during the dissection. Dissections were performed in sodium  
1153 bicarbonate-buffered Ames' solution (Sigma, St. Louis, MO) equilibrated with 5% CO<sub>2</sub> + 95%  
1154 O<sub>2</sub> to pH 7.4 and maintained at 32-34° C. Hemisection of the eye was performed along the ora  
1155 serrata by first making a small incision, following which the vitreous was removed and the retina  
1156 was isolated from the pigment epithelium and eye cup. A piece of dorsal retina (1-2 mm<sup>2</sup>) was  
1157 dissected and placed RGC-side down on the planar MEA.

1158 The MEA consisted of 519 electrodes with 30  $\mu\text{m}$  inter-electrode spacing, covering a  
1159 hexagonal region with 450  $\mu\text{m}$  on a side (Field et al., 2010). The voltage on each electrode was  
1160 digitized at 20 kHz and stored for post-hoc analysis. Details of recording methods and spike  
1161 sorting have been described previously (Field et al., 2007). Spikes were identified using a  
1162 threshold of four times the voltage standard deviation on each electrode. Principal component  
1163 analysis applied to the ensemble of spike waveforms measured on each electrode provided a  
1164 subspace for clustering spikes according to their shape. A Gaussian mixture model was used to  
1165 cluster the spikes originating from individual RGCs. The clusters were manually inspected for  
1166 each identified ooDSGC to ensure the spike waveforms were well isolated from other

1167 simultaneously recorded RGCs and all spikes were captured within each cluster. When a single  
 1168 cluster of spikes was captured by more than one Gaussian or when a single Gaussian included  
 1169 spikes from more than one cluster, the clustering was manually adjusted to generate a new set of  
 1170 initial conditions for re-fitting the mixture of Gaussians. Spike clusters with >10% estimated  
 1171 contamination based on refractory period violations, or spike rates <1 Hz, were excluded from  
 1172 further analysis.

### 1173 *Visual stimulation and RGC responses*

1174 Visual stimuli were focused on the photoreceptor outer segment, from an OLED display  
 1175 (Emagin, Inc.) with 60.35 Hz refresh rate. The mean intensity of the stimulus was 7000  
 1176 photoisomerizations per rod per s, or 5000 photoisomerizations per cone per s for a cone  
 1177 containing all M-opsin. These estimates do not account for the effect of pigment self-screening.  
 1178 To measure the direction tuning of ooDSGCs as a function of contrast, a positive contrast bar  
 1179 (1200  $\mu\text{m}$  wide) was presented on a gray background (Fig. 10B). On each presentation, the bar  
 1180 moved in one of twelve equally spaced directions at 400  $\mu\text{m}/\text{sec}$  and was presented at one of the  
 1181 following (Weber) contrasts: 5%, 10%, 20%, 40%, 80%, 150% and 300%. Responses to a total  
 1182 of 8 trials were collected for every condition; stimulus conditions were presented pseudo  
 1183 randomly. Spike times were binned at 1 ms resolution for all subsequent analyses.

1184 To distinguish DSGCs from other RGCs recorded on the MEA, square-wave drifting  
 1185 gratings were used. These gratings drifted in one of twelve different and equally spaced  
 1186 directions and at two different speeds (225  $\mu\text{m}/\text{sec}$  and 900  $\mu\text{m}/\text{sec}$ ; spatial period 400 $\mu\text{m}/\text{cycle}$ ).  
 1187 DSGCs were identified based on their direction selectivity index (DSI) defined as:

$$DSI = \frac{|\sum \vec{v}_i|}{\sum n_i}$$

1188 calculated from responses to drifting gratings and moving bars. Here,  $n_i$  is the number of spikes  
 1189 elicited to stimulus movement along the direction  $i$  defined by the vector  $\vec{v}_i$ .

1190 The distribution of DSIs across all recorded RGCs was bimodal, with DSGCs forming  
 1191 the high mode (Fig. 10A). Based on these distributions, a DSI of 0.25 reliably identified DSGCs  
 1192 in wild-type and *Megf10*<sup>-/-</sup> retinas. ooDSGCs were isolated from ON DSGCs by their distinct  
 1193 ON and OFF responses to a bar entering and exiting the receptive field (Fig. 10B). The total  
 1194 ooDSGC sample size obtained by this procedure was  $n = 80$  from the two wild-type and  $n = 74$   
 1195 from the two *Megf10*<sup>-/-</sup> retinas. The paired Kolmogorov-Smirnov (KS) test was used to compare  
 1196 cumulative probability distributions from these two populations.

### 1197 **Analysis of ooDSGC response**

#### 1198 *Measurement of direction tuning width*

1199 First, the direction tuning curve for each ooDSGC was obtained by calculating the  
 1200 number of spikes elicited across all trials for each direction of bar movement. Due to the circular  
 1201 nature of the data, the direction tuning curve was treated as circular normal distribution, also  
 1202 called von Mises distribution (Oesch et al., 2005), and the tuning width was measured as the  
 1203 circular standard deviation ( $\sigma_{circ}$ ), defined by

1204

$$\sigma_{circ} = \sqrt{-2\ln(R)}$$

1205

1206 where  $R$  is the second moment of the von Mises distribution:

1207

$$f(\theta, \mu) = \frac{1}{2\pi I_0(\kappa)} e^{\kappa \cos(\theta - \mu)}$$

1208

1209 This yielded a nonparametric estimate of the tuning curve width.

### 1210 *Measurement of direction tuning strength*

1211 To measure the strength of tuning, the difference between spike counts to motion in the  
 1212 preferred and null directions was normalized by the sum of these responses. The tuning curves  
 1213 were sampled at 30 degree intervals. To estimate the response in the preferred (null) direction,  
 1214 which could fall between sampled directions, a cosine-weighted average of the two strongest  
 1215 (weakest) responses was calculated. This yielded the following equation for measuring tuning  
 1216 strength:

$$1217 \quad \text{Tuning strength} = \frac{\sum_{i=1}^2 r_i \cos(|\theta_{PD} - \theta_i|) - \sum_{j=1}^2 r_j \cos(|\theta_{ND} - \theta_j|)}{\sum_{i=1}^2 r_i \cos(|\theta_{PD} - \theta_i|) + \sum_{j=1}^2 r_j \cos(|\theta_{ND} - \theta_j|)}$$

1218

1219 where the summation  $\sum_{i=1}^2$  is performed over the responses  $r_i$  weighted by the cosine terms for  
 1220 the two nearest neighbor movement directions  $\theta_i$  around the preferred direction  $\theta_{PD}$  and the null  
 1221 direction  $\theta_{ND}$ . This resulting index for tuning strength varied between zero and unity.

### 1222 *Measurement of direction tuning similarity between ON and OFF responses*

1223 To separately analyze the ON and OFF responses of ooDSGCs, we first defined temporal  
 1224 windows for each ooDSGC that distinctly separate the ON and OFF responses. This was done by  
 1225 passing high-contrast moving bars (150% and 300% contrast) through the receptive field. In the  
 1226 resulting spike rasters, ON and OFF response phases were clearly discernible (Fig. 10B,F). The

1227 boundary for separating the ON and OFF responses was set halfway between the peak ON and  
1228 OFF spike rate locations (Fig. 10F,G). Once the temporal boundary was defined, the preferred  
1229 direction was calculated independently for the ON and OFF responses for each ooDSGC. The  
1230 same ON-OFF temporal boundaries were used for all contrasts shown in Fig. 10-Supplement 1.  
1231 The difference between the preferred directions,  $\Delta\phi$ , quantified the angular difference between  
1232 the ON and OFF preferred directions (Fig. 10F).

### 1233 *Analysis of ooDSGC subtypes*

1234 ooDSGC subtype classification was performed using the K-means clustering algorithm.  
1235 This was done by first assigning a set of four initial seed values corresponding to the four  
1236 cardinal directions of ooDSGCs (Oyster and Barlow, 1967). Next, the angular difference  
1237 between the seed values (for first iteration) or the cluster means (for later iterations), and the  
1238 preferred directions of each ooDSGCs was calculated. The cluster for which the angular  
1239 difference was minimum was the cluster to which an ooDSGC was assigned. This yielded the  
1240 four subpopulations of ooDSGCs described in Fig. 10-Supplement 1.

### 1241 **Quantification and Statistical Analysis**

1242 Statistical analysis was performed using GraphPad Prism software  
1243 (anatomy/development studies) or using custom JAVA based software and MATLAB software  
1244 (physiology studies). This software is available, together with the primary data it was written to  
1245 analyze, at a public repository (Roy and Field, 2017; <https://github.com/Field-Lab/megf10->  
1246 [dstuning](https://github.com/Field-Lab/megf10-dstuning)). Statistical tests used for each experiment are given in the appropriate Methods section  
1247 above, and/or in the figure legends. Sample sizes for each experiment are given in the  
1248 appropriate Methods section above or else in the Results. *P*-values ( $\alpha = 0.05$ ) are given in figure

1249 legends, or in the Results if no figure is shown. Error bars are defined in figure legends. Exact *p*-  
1250 values are reported unless the value was less than  $1.0 \times 10^{-7}$ .

1251

## 1252 **ACKNOWLEDGEMENTS**

1253 For financial support we thank the National Eye Institute (EY024694 to JNK; EY026344  
1254 to TAR; EY024567 to GDF; EY5722 to Duke University); Pew Charitable Trusts, E. Matilda  
1255 Ziegler Foundation, McKnight Endowment Fund for Neuroscience, Alfred P. Sloan foundation  
1256 (JNK); the Whitehall Foundation (GDF); and Research to Prevent Blindness Unrestricted Grant  
1257 (Duke University). We thank Sidney Kuo and Greg Schwartz for suggesting use of the *Gjd2*-  
1258 *GFP* mouse line; members of the Kay lab and Cagla Eroglu for their comments on the  
1259 manuscript; Megan Stogsdill and Ari Pereira for mouse colony support; and X. Duan and J.  
1260 Sanes (Harvard) for *Kcng4<sup>Cre</sup>* mice.

1261

## 1262 **COMPETING INTERESTS**

1263 The authors have no competing interests to disclose.

1264 **REFERENCES**

- 1265 Amthor, F.R., and N.M. Grzywacz. 1993. Inhibition in ON-OFF directionally selective ganglion  
1266 cells of the rabbit retina. *J. Neurophysiol.* 69:2174–87.
- 1267 Baier, H. 2013. Synaptic laminae in the visual system: molecular mechanisms forming layers of  
1268 perception. *Annu. Rev. Cell Dev. Biol.* 29:385–416. doi:10.1146/annurev-cellbio-101011-  
1269 155748.
- 1270 Cai, D., K.B. Cohen, T. Luo, J.W. Lichtman, and J.R. Sanes. 2013. Improved tools for the  
1271 Brainbow toolbox. *Nat. Methods.* 10:540–7. doi:10.1038/nmeth.2450.
- 1272 Chen, M., S. Lee, S.J.H. Park, L.L. Looger, and Z.J. Zhou. 2014. Receptive field properties of  
1273 bipolar cell axon terminals in direction-selective sublaminae of the mouse retina. *J.*  
1274 *Neurophysiol.* 112:1950–62. doi:10.1152/jn.00283.2014.
- 1275 Chow, R.W., A.D. Almeida, O. Randlett, C. Norden, and W. a. Harris. 2015. Inhibitory neuron  
1276 migration and IPL formation in the developing zebrafish retina. *Development.* 142:2665–77.  
1277 doi:10.1242/dev.122473.
- 1278 Chung, W.-S., L.E. Clarke, G.X. Wang, B.K. Stafford, A. Sher, C. Chakraborty, J. Joung, L.C.  
1279 Foo, A. Thompson, C. Chen, S.J. Smith, and B.A. Barres. 2013. Astrocytes mediate synapse  
1280 elimination through MEGF10 and MERTK pathways. *Nature.* 504:394–400.  
1281 doi:10.1038/nature12776.
- 1282 Cooper, J.A. 2014. Molecules and mechanisms that regulate multipolar migration in the  
1283 intermediate zone. *Front. Cell. Neurosci.* 8:386. doi:10.3389/fncel.2014.00386.
- 1284 Deans, M.R., A. Krol, V.E. Abraira, C.O. Copley, A.F. Tucker, and L. V Goodrich. 2011.  
1285 Control of neuronal morphology by the atypical cadherin Fat3. *Neuron.* 71:820–32.  
1286 doi:10.1016/j.neuron.2011.06.026.
- 1287 Demb, J.B. 2007. Cellular mechanisms for direction selectivity in the retina. *Neuron.* 55:179–86.  
1288 doi:10.1016/j.neuron.2007.07.001.
- 1289 Ding, H., R.G. Smith, A. Polog-Polsky, J.S. Diamond, and K.L. Briggman. 2016. Species-  
1290 specific wiring for direction selectivity in the mammalian retina. *Nature.* 535:105–110.  
1291 doi:10.1038/nature18609.
- 1292 Duan, X., A. Krishnaswamy, I. De la Huerta, and J.R. Sanes. 2014. Type II cadherins guide  
1293 assembly of a direction-selective retinal circuit. *Cell.* 158:793–807.  
1294 doi:10.1016/j.cell.2014.06.047.
- 1295 Field, G.D., J.L. Gauthier, A. Sher, M. Greschner, T.A. Machado, L.H. Jepson, J. Shlens, D.E.  
1296 Gunning, K. Mathieson, W. Dabrowski, L. Paninski, A.M. Litke, and E.J. Chichilnisky.  
1297 2010. Functional connectivity in the retina at the resolution of photoreceptors. *Nature.*  
1298 467:673–7. doi:10.1038/nature09424.
- 1299 Field, G.D., A. Sher, J.L. Gauthier, M. Greschner, J. Shlens, A.M. Litke, and E.J. Chichilnisky.  
1300 2007. Spatial properties and functional organization of small bistratified ganglion cells in

- 1301 primate retina. *J. Neurosci.* 27:13261–72. doi:10.1523/JNEUROSCI.3437-07.2007.
- 1302 Fiscella, M., F. Franke, K. Farrow, J. Müller, B. Roska, R. Azeredo da Silveira, and A.  
1303 Hierlemann. 2015. Visual coding with a population of direction-selective neurons. *J.*  
1304 *Neurophysiol.* 114:2485–2499. doi:10.1152/jn.00919.2014.
- 1305 Fujitani, Y., S. Fujitani, H. Luo, F. Qiu, J. Burlison, Q. Long, Y. Kawaguchi, H. Edlund, R.J.  
1306 MacDonald, T. Furukawa, T. Fujikado, M.A. Magnuson, M. Xiang, and C.V.E. Wright.  
1307 2006. Ptf1a determines horizontal and amacrine cell fates during mouse retinal development.  
1308 *Development.* 133:4439–50. doi:10.1242/dev.02598.
- 1309 Furuta, Y., O. Lagutin, B.L. Hogan, and G.C. Oliver. 2000. Retina- and ventral forebrain-  
1310 specific Cre recombinase activity in transgenic mice. *Genesis.* 26:130–2.
- 1311 Galli-Resta, L., G. Resta, S.S. Tan, and B.E. Reese. 1997. Mosaics of islet-1-expressing  
1312 amacrine cells assembled by short-range cellular interactions. *J. Neurosci.* 17:7831–8.
- 1313 Godinho, L., J.S. Mumm, P.R. Williams, E.H. Schroeter, A. Koerber, S.W. Park, S.D. Leach,  
1314 and R.O.L. Wong. 2005. Targeting of amacrine cell neurites to appropriate synaptic laminae  
1315 in the developing zebrafish retina. *Development.* 132:5069–79. doi:10.1242/dev.02075.
- 1316 Green, E.S., J.L. Stubbs, and E.M. Levine. 2003. Genetic rescue of cell number in a mouse  
1317 model of microphthalmia: interactions between Chx10 and G1-phase cell cycle regulators.  
1318 *Development.* 130:539–52.
- 1319 Greene, M.J., J.S. Kim, H.S. Seung, and EyeWriters. 2016. Analogous Convergence of Sustained  
1320 and Transient Inputs in Parallel On and Off Pathways for Retinal Motion Computation. *Cell*  
1321 *Rep.* 14:1892–900. doi:10.1016/j.celrep.2016.02.001.
- 1322 Hinds, J.W., and P.L. Hinds. 1978. Early development of amacrine cells in the mouse retina: an  
1323 electron microscopic, serial section analysis. *J. Comp. Neurol.* 179:277–300.  
1324 doi:10.1002/cne.901790204.
- 1325 Hoshiba, Y., T. Toda, H. Ebisu, M. Wakimoto, S. Yanagi, and H. Kawasaki. 2016. Sox11  
1326 Balances Dendritic Morphogenesis with Neuronal Migration in the Developing Cerebral  
1327 Cortex. *J. Neurosci.* 36:5775–84. doi:10.1523/JNEUROSCI.3250-15.2016.
- 1328 Huberman, A.D., W. Wei, J. Elstrott, B.K. Stafford, M.B. Feller, and B.A. Barres. 2009. Genetic  
1329 identification of an On-Off direction-selective retinal ganglion cell subtype reveals a layer-  
1330 specific subcortical map of posterior motion. *Neuron.* 62:327–34.  
1331 doi:10.1016/j.neuron.2009.04.014.
- 1332 Kay, J.N., M.W. Chu, and J.R. Sanes. 2012. MEGF10 and MEGF11 mediate homotypic  
1333 interactions required for mosaic spacing of retinal neurons. *Nature.* 483:465–9.  
1334 doi:10.1038/nature10877.
- 1335 Kay, J.N., I. De la Huerta, I.-J. Kim, Y. Zhang, M. Yamagata, M.W. Chu, M. Meister, and J.R.  
1336 Sanes. 2011. Retinal ganglion cells with distinct directional preferences differ in molecular  
1337 identity, structure, and central projections. *J. Neurosci.* 31:7753–62.  
1338 doi:10.1523/JNEUROSCI.0907-11.2011.

- 1339 Kay, J.N., and J.R. Sanes. 2013. Development of retinal arbors and synapses. *In* The New Visual  
1340 Neurosciences. J.S. Werner and L.M. Chalupa, editors. MIT Press, Cambridge.
- 1341 Kim, J.S., M.J. Greene, A. Zlateski, K. Lee, M. Richardson, S.C. Turaga, M. Purcaro, M.  
1342 Balkam, A. Robinson, B.F. Behabadi, M. Campos, W. Denk, H.S. Seung, and EyeWriters.  
1343 2014. Space-time wiring specificity supports direction selectivity in the retina. *Nature*.  
1344 509:331–6. doi:10.1038/nature13240.
- 1345 Knabe, W., S. Washausen, N. Happel, and H.J. Kuhn. 2007. Development of starburst  
1346 cholinergic amacrine cells in the retina of *Tupaia belangeri*. *J. Comp. Neurol.* 502:584–597.  
1347 doi:10.1002/cne.
- 1348 Kostadinov, D., and J.R. Sanes. 2015. Protocadherin-dependent dendritic selfavoidance regulates  
1349 neural connectivity and circuit function. *Elife*. 4. doi:10.7554/eLife.08964.
- 1350 Krah, N.M., J.-P. De La O, G.H. Swift, C.Q. Hoang, S.G. Willet, F. Chen Pan, G.M. Cash, M.P.  
1351 Bronner, C.V. Wright, R.J. MacDonald, and L.C. Murtaugh. 2015. The acinar  
1352 differentiation determinant PTF1A inhibits initiation of pancreatic ductal adenocarcinoma.  
1353 *Elife*. 4. doi:10.7554/eLife.07125.
- 1354 Krol, A., S.J. Henle, and L. V Goodrich. 2016. Fat3 and Ena/VASP proteins influence the  
1355 emergence of asymmetric cell morphology in the developing retina. *Development*.  
1356 143:2172–82. doi:10.1242/dev.133678.
- 1357 Lefebvre, J.L., J.R. Sanes, and J.N. Kay. 2015. Development of dendritic form and function.  
1358 *Annu. Rev. Cell Dev. Biol.* 31:741–77. doi:10.1146/annurev-cellbio-100913-013020.
- 1359 Madisen, L., T.A. Zwingman, S.M. Sunkin, S.W. Oh, H.A. Zariwala, H. Gu, L.L. Ng, R.D.  
1360 Palmiter, M.J. Hawrylycz, A.R. Jones, E.S. Lein, and H. Zeng. 2010. A robust and high-  
1361 throughput Cre reporting and characterization system for the whole mouse brain. *Nat.*  
1362 *Neurosci.* 13:133–40. doi:10.1038/nn.2467.
- 1363 Matsuoka, R.L., K.T. Nguyen-Ba-Charvet, A. Parray, T.C. Badea, A. Chédotal, and A.L.  
1364 Kolodkin. 2011. Transmembrane semaphorin signalling controls laminar stratification in the  
1365 mammalian retina. *Nature*. 470:259–63. doi:10.1038/nature09675.
- 1366 Morgan, J.L., A. Dhingra, N. Vardi, and R.O.L. Wong. 2006. Axons and dendrites originate  
1367 from neuroepithelial-like processes of retinal bipolar cells. *Nat. Neurosci.* 9:85–92.  
1368 doi:10.1038/nn1615.
- 1369 Moshiri, A., E. Gonzalez, K. Tagawa, H. Maeda, M. Wang, L.J. Frishman, and S.W. Wang. 2008.  
1370 Near complete loss of retinal ganglion cells in the *math5/brn3b* double knockout elicits  
1371 severe reductions of other cell types during retinal development. *Dev. Biol.* 316:214–27.  
1372 doi:10.1016/j.ydbio.2008.01.015.
- 1373 Muzumdar, M.D., B. Tasic, K. Miyamichi, L. Li, and L. Luo. 2007. A global double-fluorescent  
1374 Cre reporter mouse. *genesis*. 45:593–605. doi:10.1002/dvg.20335.
- 1375 Nadarajah, B., J.E. Brunstrom, J. Grutzendler, R.O. Wong, and A.L. Pearlman. 2001. Two  
1376 modes of radial migration in early development of the cerebral cortex. *Nat. Neurosci.*

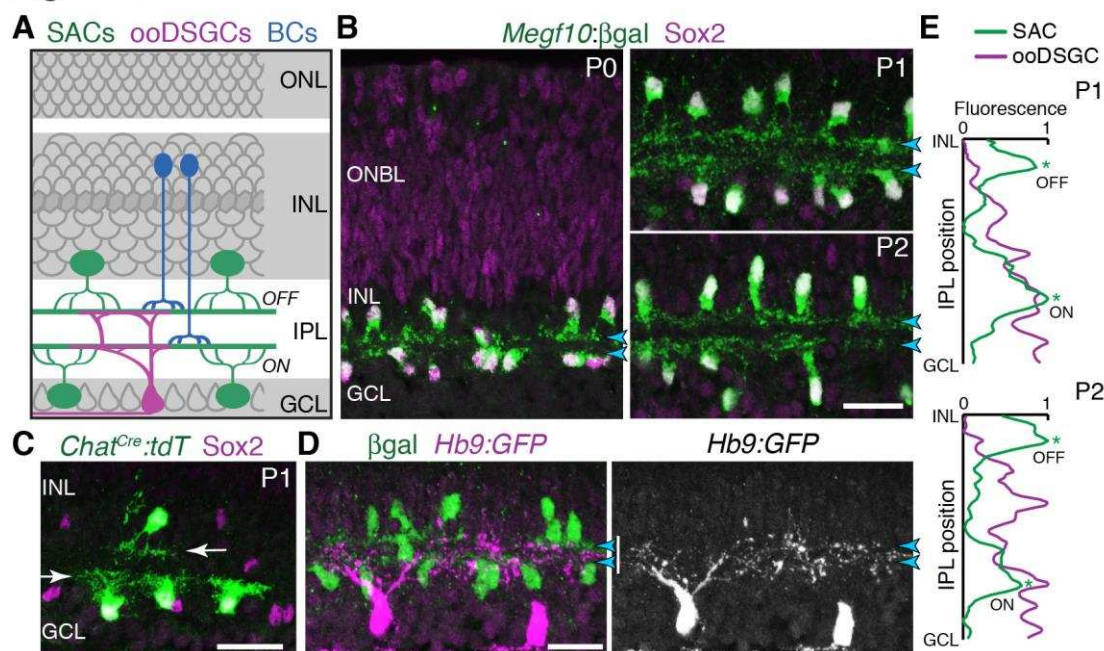
- 1377 4:143–50. doi:10.1038/83967.
- 1378 Nakhai, H., S. Sel, J. Favor, L. Mendoza-Torres, F. Paulsen, G.I.W. Duncker, and R.M. Schmid.  
1379 2007. Ptf1a is essential for the differentiation of GABAergic and glycinergic amacrine cells  
1380 and horizontal cells in the mouse retina. *Development*. 134:1151–60.  
1381 doi:10.1242/dev.02781.
- 1382 Oesch, N., T. Euler, and W.R. Taylor. 2005. Direction-selective dendritic action potentials in  
1383 rabbit retina. *Neuron*. 47:739–50.
- 1384 Oyster, C.W., and H.B. Barlow. 1967. Direction-selective units in rabbit retina: distribution of  
1385 preferred directions. *Science*. 155:841–842. doi:10.1126/science.155.3764.841.
- 1386 Peng, Y.R., N.M. Tran, A. Krishnaswamy, D. Kostadinov, E.M. Martersteck, and J.R. Sanes.  
1387 2017. Satb1 Regulates Contactin 5 to Pattern Dendrites of a Mammalian Retinal Ganglion  
1388 Cell. *Neuron*. 95:869–883.e6. doi:10.1016/j.neuron.2017.07.019.
- 1389 Poleg-Polsky, A., and J.S. Diamond. 2016. Retinal Circuitry Balances Contrast Tuning of  
1390 Excitation and Inhibition to Enable Reliable Computation of Direction Selectivity. *J.*  
1391 *Neurosci*. 36:5861–76. doi:10.1523/JNEUROSCI.4013-15.2016.
- 1392 Rawlins, E.L., T. Okubo, Y. Xue, D.M. Brass, R.L. Auten, H. Hasegawa, F. Wang, and B.L.M.  
1393 Hogan. 2009. The role of Scgb1a1+ Clara cells in the long-term maintenance and repair of  
1394 lung airway, but not alveolar, epithelium. *Cell Stem Cell*. 4:525–34.  
1395 doi:10.1016/j.stem.2009.04.002.
- 1396 Rossi, J., N. Balthasar, D. Olson, M. Scott, E. Berglund, C.E. Lee, M.J. Choi, D. Lauzon, B.B.  
1397 Lowell, and J.K. Elmquist. 2011. Melanocortin-4 receptors expressed by cholinergic  
1398 neurons regulate energy balance and glucose homeostasis. *Cell Metab*. 13:195–204.  
1399 doi:10.1016/j.cmet.2011.01.010.
- 1400 Roy, S., and G.D. Field. 2017. Field-Lab/megf10-dstuning. Github. [https://github.com/Field-](https://github.com/Field-Lab/megf10-dstuning)  
1401 [Lab/megf10-dstuning](https://github.com/Field-Lab/megf10-dstuning).
- 1402 Sanes, J.R., and M. Yamagata. 2009. Many paths to synaptic specificity. *Annu. Rev. Cell Dev.*  
1403 *Biol*. 25:161–95. doi:10.1146/annurev.cellbio.24.110707.175402.
- 1404 Sanes, J.R., and S.L. Zipursky. 2010. Design principles of insect and vertebrate visual systems.  
1405 *Neuron*. 66:15–36. doi:10.1016/j.neuron.2010.01.018.
- 1406 Schindelin, J., I. Arganda-Carreras, E. Frise, V. Kaynig, M. Longair, T. Pietzsch, S. Preibisch, C.  
1407 Rueden, S. Saalfeld, B. Schmid, J.-Y. Tinevez, D.J. White, V. Hartenstein, K. Eliceiri, P.  
1408 Tomancak, and A. Cardona. 2012. Fiji: an open-source platform for biological-image  
1409 analysis. *Nat. Methods*. 9:676–82. doi:10.1038/nmeth.2019.
- 1410 Sethuramanujam, S., A.J. McLaughlin, G. DeRosenroll, A. Hoggarth, D.J. Schwab, and G.B.  
1411 Awatramani. 2016. A Central Role for Mixed Acetylcholine/GABA Transmission in  
1412 Direction Coding in the Retina. *Neuron*. 90:1243–56. doi:10.1016/j.neuron.2016.04.041.
- 1413 Sethuramanujam, S., X. Yao, G. DeRosenroll, K.L. Briggman, G.D. Field, and G.B. Awatramani.

- 1414 2017. “Silent” NMDA Synapses Enhance Motion Sensitivity in a Mature Retinal Circuit.  
1415 *Neuron*. 96:1099–1111.e3. doi:10.1016/j.neuron.2017.09.058.
- 1416 Stacy, R.C., and R.O.L. Wong. 2003. Developmental relationship between cholinergic amacrine  
1417 cell processes and ganglion cell dendrites of the mouse retina. *J. Comp. Neurol.* 456:154–66.  
1418 doi:10.1002/cne.10509.
- 1419 Sun, L.O., Z. Jiang, M. Rivlin-Etzion, R. Hand, C.M. Brady, R.L. Matsuoka, K.-W. Yau, M.B.  
1420 Feller, and A.L. Kolodkin. 2013. On and off retinal circuit assembly by divergent molecular  
1421 mechanisms. *Science*. 342. doi:10.1126/science.1241974.
- 1422 Tabata, H., and K. Nakajima. 2003. Multipolar migration: the third mode of radial neuronal  
1423 migration in the developing cerebral cortex. *J. Neurosci.* 23:9996–10001. doi:23/31/9996  
1424 [pii].
- 1425 Taylor, W.R., and D.I. Vaney. 2002. Diverse synaptic mechanisms generate direction selectivity  
1426 in the rabbit retina. *J. Neurosci.* 22:7712–20.
- 1427 Trenholm, S., K. Johnson, X. Li, R.G. Smith, and G.B. Awatramani. 2011. Parallel mechanisms  
1428 encode direction in the retina. *Neuron*. 71:683–94. doi:10.1016/j.neuron.2011.06.020.
- 1429 Vaney, D.I., and D. V Pow. 2000. The dendritic architecture of the cholinergic plexus in the  
1430 rabbit retina: selective labeling by glycine accumulation in the presence of sarcosine. *J.*  
1431 *Comp. Neurol.* 421:1–13.
- 1432 Vaney, D.I., B. Sivyver, and W.R. Taylor. 2012. Direction selectivity in the retina: symmetry and  
1433 asymmetry in structure and function. *Nat. Rev. Neurosci.* 13:194–208. doi:10.1038/nrn3165.
- 1434 Visser, J.J., Y. Cheng, S.C. Perry, A.B. Chastain, B. Parsa, S.S. Masri, T.A. Ray, J.N. Kay, and  
1435 W.M. Wojtowicz. 2015. An extracellular biochemical screen reveals that FLRTs and Unc5s  
1436 mediate neuronal subtype recognition in the retina. *Elife*. 4:e08149.  
1437 doi:10.7554/eLife.08149.
- 1438 Vlasits, A.L., R.D. Morrie, A. Tran-Van-Minh, A. Bleckert, C.F. Gainer, D.A. DiGregorio, and  
1439 M.B. Feller. 2016. A Role for Synaptic Input Distribution in a Dendritic Computation of  
1440 Motion Direction in the Retina. *Neuron*. 89:1317–1330. doi:10.1016/j.neuron.2016.02.020.
- 1441 Wang, J., M.L. O’Sullivan, D. Mukherjee, V.M. Puñal, S. Farsiu, and J.N. Kay. 2017. Anatomy  
1442 and spatial organization of Müller glia in mouse retina. *J. Comp. Neurol.* 525:1759–1777.  
1443 doi:10.1002/cne.24153.
- 1444 Wässle, H., C. Puller, F. Müller, and S. Haverkamp. 2009. Cone contacts, mosaics, and  
1445 territories of bipolar cells in the mouse retina. *J. Neurosci.* 29:106–17.  
1446 doi:10.1523/JNEUROSCI.4442-08.2009.
- 1447 Whitney, I.E., P.W. Keeley, A.J. St John, A.G. Kautzman, J.N. Kay, and B.E. Reese. 2014. Sox2  
1448 regulates cholinergic amacrine cell positioning and dendritic stratification in the retina. *J.*  
1449 *Neurosci.* 34:10109–21. doi:10.1523/JNEUROSCI.0415-14.2014.
- 1450 Xu, H.-P., T.J. Burbridge, M. Ye, M. Chen, X. Ge, Z.J. Zhou, and M.C. Crair. 2016. Retinal

- 1451 Wave Patterns Are Governed by Mutual Excitation among Starburst Amacrine Cells and  
1452 Drive the Refinement and Maintenance of Visual Circuits. *J. Neurosci.* 36:3871–3886.  
1453 doi:10.1523/JNEUROSCI.3549-15.2016.
- 1454 Yamagata, M., and J.R. Sanes. 2008. Dscam and Sidekick proteins direct lamina-specific  
1455 synaptic connections in vertebrate retina. *Nature.* 451:465–9. doi:10.1038/nature06469.
- 1456 Yang, L., C.-L. Cai, L. Lin, Y. Qyang, C. Chung, R.M. Monteiro, C.L. Mummery, G.I. Fishman,  
1457 A. Cogen, and S. Evans. 2006. Isl1Cre reveals a common Bmp pathway in heart and limb  
1458 development. *Development.* 133:1575–85. doi:10.1242/dev.02322.
- 1459 Yu, W.-Q., N.M. Grzywacz, E.-J. Lee, and G.D. Field. 2017. Cell-type specific changes in  
1460 retinal ganglion cell function induced by rod death and cone reorganization in rats. *J.*  
1461 *Neurophysiol.* jn.00826.2016. doi:10.1152/jn.00826.2016.
- 1462

## 463 FIGURES &amp; LEGENDS

Figure 1



464

465

466

**Figure 1: Initial formation of DS circuit IPL sublayers.**

467

A: Schematic of mature direction-selective (DS) circuit and its cell types, depicted in cross-section. SACs (green) and bipolar cells (blue) project to one of two IPL sublayers (*OFF*, *ON*). *OFF* SACs reside in inner nuclear layer (INL); *ON* SACs reside in ganglion cell layer (GCL). ooDSGCs (purple) send dendrites to both DS circuit sublayers. ONL, outer nuclear layer.

471

B: SAC IPL sublayer formation assessed in *Megf10<sup>lacZ</sup>* mice. All SACs are double-positive for anti-Sox2 (purple) and anti-βgal (green). Progenitors in outer neuroblast layer (ONBL) also express Sox2. SAC IPL sublayers (arrowheads) begin to appear by P0, and are fully apparent by P1.

474

C: Sparse labeling of neonatal SACs in *Chat<sup>Cre</sup>* mice. Individual SACs have laminar-specific projections by P1 (arrows). tdT, tdTomato.

476

D,E: ooDSGCs (labeled by Hb9-GFP) project diffusely in the IPL at P1-P2, whereas SAC arbors are stratified (arrowheads). D: retinal cross-sections. Vertical white bar denotes IPL width. E: Fluorescence intensity plots of SAC and ooDSGC dendrite staining across IPL, from representative images (P2 image in D; P1 image in Fig.1-Supplement 2). ON and OFF strata (asterisks) are clear for SACs but not for ooDSGC dendrites.

480

Scale bars: 25 μm.

Figure 2

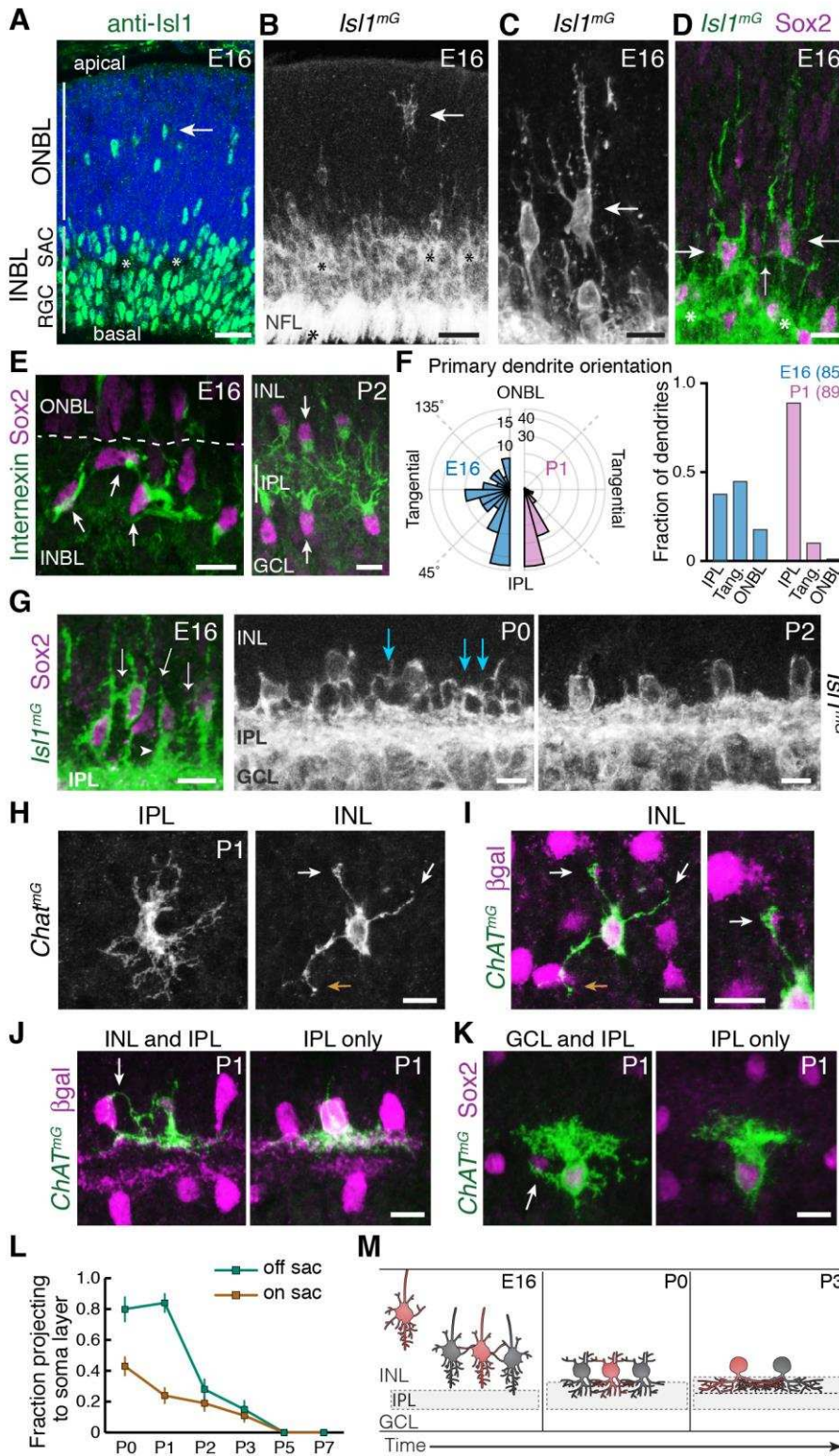


**Figure 2:** Newborn SACs contact each other via a network of soma layer arbors.

**A,B:** *Isl1* labels SACs and RGCs in embryonic retina. **A**, immunostaining; **B**, mGFP driven by *Isl1<sup>Cre</sup>* (*Isl1<sup>mG</sup>*). Arrows, newborn SACs migrating apico-basally through ONBL. INBL SACs and RGCs predominantly reside in indicated regions. IPL neuropil (asterisks) exists in discontinuous patches at this age. NFL, nerve fiber layer containing RGC axons. Blue, nuclear counterstain.

**B,C:** Migrating SACs in ONBL (arrows) have multipolar morphology. They are far from other SACs and do not contact them.

**D:** Morphology of *Sox2<sup>+</sup>Isl1<sup>+</sup>* SACs (large arrows) upon arrival at INBL. SACs contact each other outside the IPL (small arrow, connecting arbor). Their migratory morphology and distance from IPL (asterisks) indicate they have not yet innervated IPL (also see Fig. 2-Supplement 2).

**E:** Internexin immunostaining reveals polarization of SAC primary dendrites. SACs project towards IPL at P2. E16 INBL SACs often project tangentially within INBL, towards neighboring SAC somata (arrows).

**F:** Quantification of primary dendrite orientation. Left, polar histogram (raw counts) of primary dendrite angles (absolute values).  $0^\circ$  was defined as perpendicular towards IPL. Note that E16 and P1 are displayed on different

scales; each plot is scaled to size of largest bin, aiding legibility in E16 plot where bin sizes are more evenly distributed. Right, fraction of dendrites oriented towards IPL, ONBL, or tangential quadrants of the polar plot (denoted by dashed lines, labels). Sample size of scored dendrites is indicated.

**G:** A network of arbors (arrows) connects somata of INBL SACs at E16. The network remains prominent in INL at P0 but is mostly gone by P2. Arrowhead, IPL-directed projection.

524 **H,I:** An individual P1 OFF SAC labeled by *Chat<sup>mG</sup>*, imaged *en face* to show its arbor morphology at IPL and  
525 INL levels. Full SAC population is revealed using *Megf10:βgal*. INL arbors (I) make selective contacts with  
526 SAC neighbors (purple): GFP<sup>+</sup> arbor tips terminate on SAC somata (orange arrow) or SAC arbors (white  
527 arrows). Right panel (I): Higher magnification view of touching arbors. Images are Z-projections of confocal  
528 stacks encompassing each arbor's volume (H, 2.0 μm; I, 3.5 μm). Projections are shown for illustration but all  
529 contacts were verified across stack volume – see Fig. 2-Supplement 3 for details.

530 **J,K:** Individual P1 OFF (K) and ON (L) SACs labeled by *Chat<sup>mG</sup>* (green) in cross-section. Purple, full SAC  
531 population. Some SACs are bi-laminar with arbors that contact neighboring somata (arrows, left panels); others  
532 project only to IPL (right panels).

533 **L:** Frequency of soma layer projections across development, determined from single *Chat<sup>mG</sup>* cells as in J,K.  
534 Error bars, standard error. Sample sizes, see Methods.

535 **M:** Schematic of newborn SAC morphology based on B-L. Soma-layer homotypic contacts are established  
536 upon completion of migration, and are mostly eliminated by P3.

537 Scale bars: 25 μm (A,B); 10 μm (all others).

538

539

Figure 3

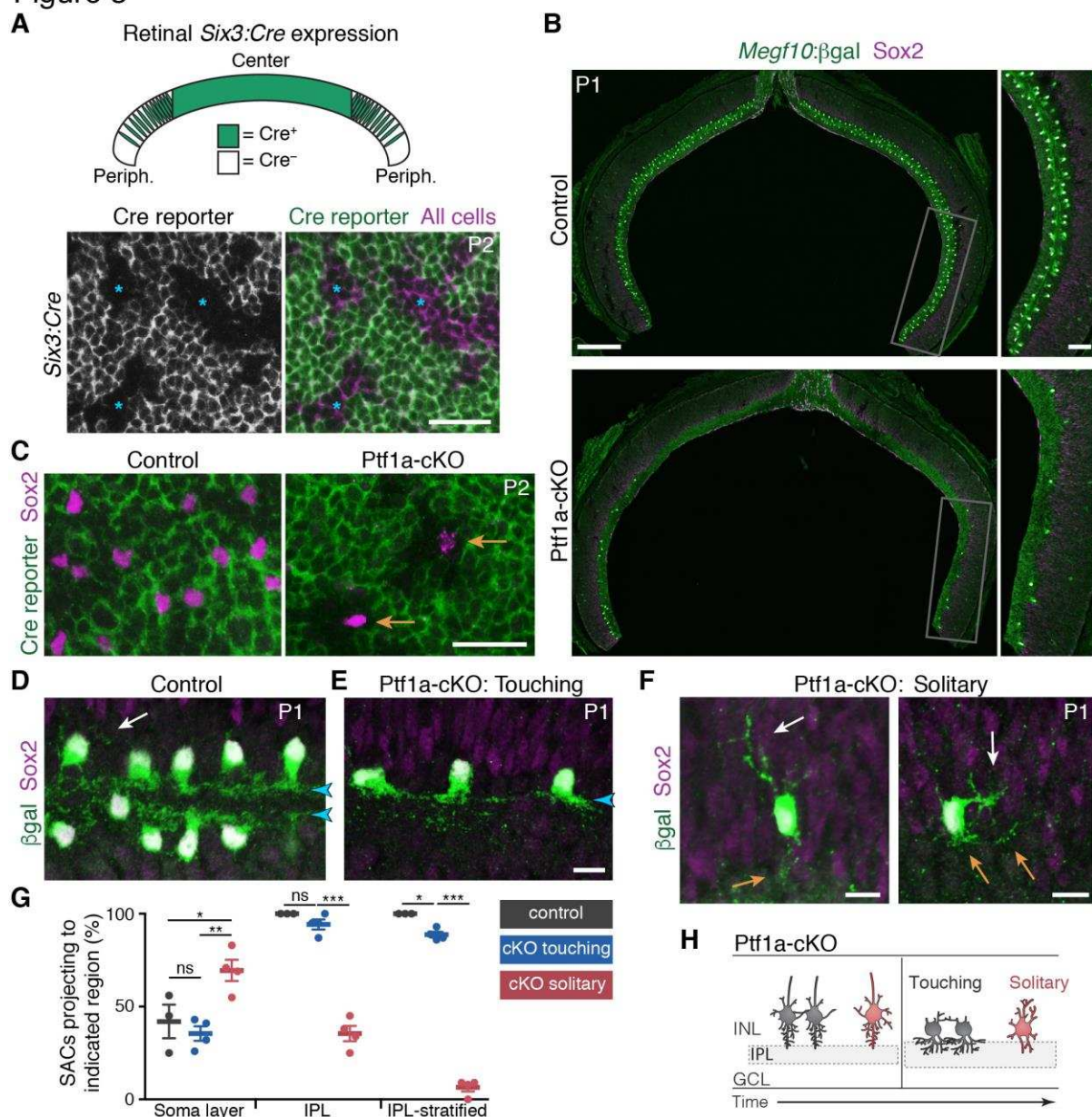


**Figure 3: SAC homotypic contact is required for IPL sublayer formation.**

**A:** Top: Schematic illustrating *Six3-Cre* expression pattern in retinal cross-section. Bottom: *En-face* view of *Six3-Cre* recombination in peripheral retina, revealed using GFP Cre reporter. Asterisks, Cre<sup>-</sup> regions.

**B:** Reduced SAC density in *Ptf1a-cKO* retina. SACs (labeled by *Sox2* and *Megf10<sup>lacZ</sup>*) are completely eliminated from *Ptf1a-cKO* central retina; some remain in peripheral retina (boxed regions, right panels). Top, littermate control (*Ptf1a<sup>+/+</sup>*).

**C:** *En-face* view of SACs in peripheral retina of *Ptf1a-cKO* and littermate control. Green, GFP Cre reporter. Control SACs were either Cre<sup>+</sup> or Cre<sup>-</sup>. Mutant SACs were Cre<sup>-</sup> (arrows), indicating that they derive only from cell lineages that maintain *Ptf1a* function.

**D-F:** SAC IPL laminar targeting in *Ptf1a-cKO* (E,F) and littermate control (D). *Ptf1a-cKO* SACs close enough to touch (E) form IPL strata (blue arrowheads), similar to control SACs (D). Solitary SACs (F) are not polarized towards IPL; they have extensive INL-directed arbors (white arrows) and rudimentary IPL-directed arbors

(orange arrows). Some solitary SACs entirely fail to innervate IPL (F, left cell) and resemble migrating E16 SACs (Fig. 2B,C); others innervate IPL with minimally-branched, non-stratified arbors (F, right cell).

**G:** Quantification of SAC dendrite phenotypes at P1-2. Left, frequency of soma layer innervation.  $*p = 0.0350$ ;  $**p = 0.0081$ ; ns,  $p = 0.7516$ . Center, frequency of IPL innervation failure (e.g. F, left).  $***p = 4.0 \times 10^{-7}$ ; ns,  $p = 0.3723$ . Right, frequency of cells that send arbors into IPL but fail to stratify (e.g. F, right).  $*p = 0.0110$ ;  $***p < 1.0 \times 10^{-7}$ . Dots, individual animals. Error bars, S.E.M. P-values, Tukey's post-hoc test. Sample sizes, see Methods.

**H:** Summary of *Ptf1a*-cKO SAC phenotype. Touching SACs are similar to wild-type SACs (Fig. 2M); they are able to innervate the IPL and form sublayers. Solitary SACs remain multipolar, similar to migrating SACs, and fail to innervate the IPL. Soma layer arbors are more elaborate than in wild-type or touching SACs.

Scale bars: 25  $\mu\text{m}$  (A,C); 200  $\mu\text{m}$  (B, left), 50  $\mu\text{m}$  (B, right), 10  $\mu\text{m}$  (D-F).

Figure 4

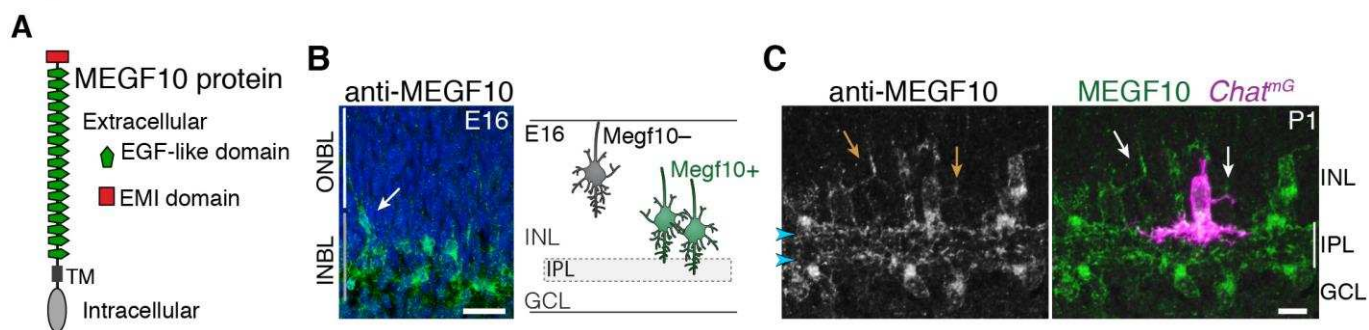


**Figure 4: MEGF10 is expressed by SACs during early homotypic contact**

**A:** Schematic of MEGF10 protein. TM, transmembrane domain.

**B:** Left, MEGF10 immunostaining at E16 reveals onset of protein expression at conclusion of radial migration. INBL SACs express MEGF10, but SACs migrating through ONBL do not. Arrow, INBL SAC with migratory morphology suggesting it is newly-arrived. Right: Schematic illustrating timing of *Megf10* expression onset in SACs (also see Kay et al., 2012).

**C:** SAC arbors in the INL (arrows) express MEGF10 protein. IPL dendrites are also labeled (arrowheads).

Scale bars: 25  $\mu$ m (B); 10  $\mu$ m (C)

Figure 5

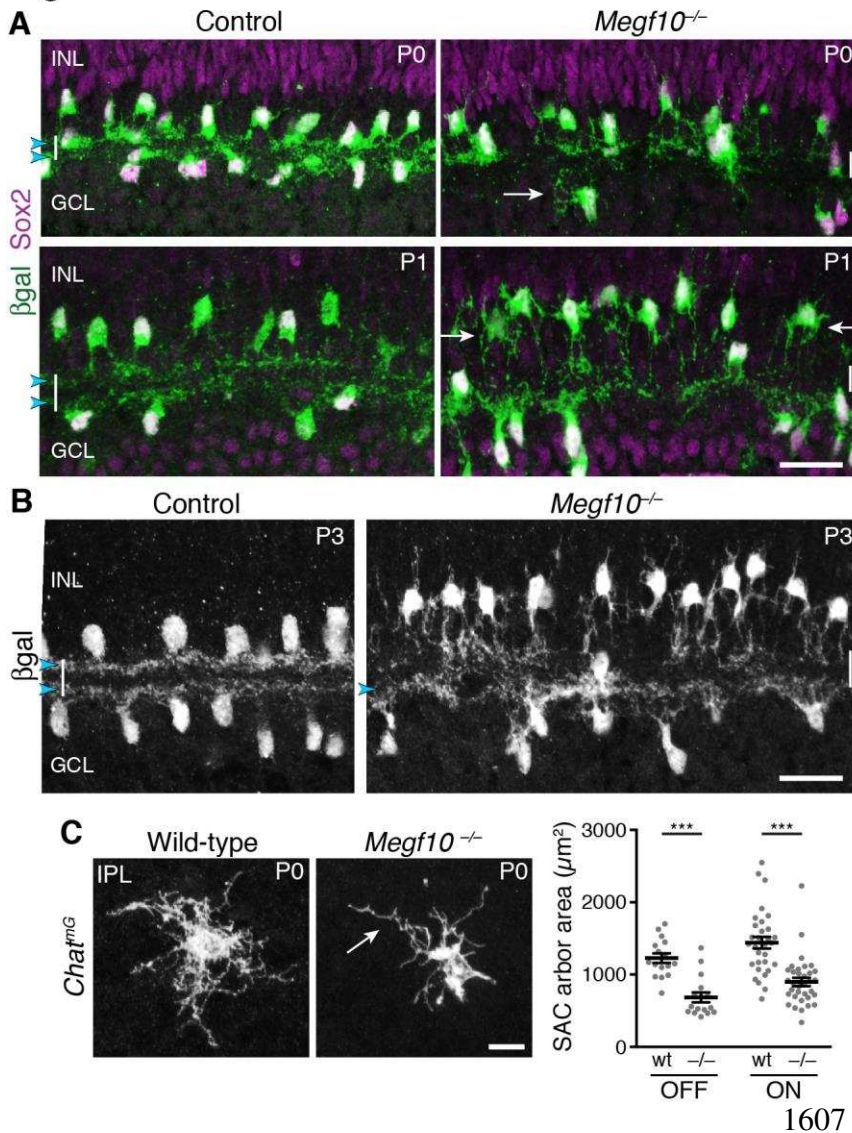


**Figure 5:** *Megf10* is required for initial formation of SAC IPL sublayers.

**A:** SAC sublayers are absent from P0-1 *Megf10* mutant IPL. Antibodies to Sox2 and  $\beta$ gal reveal SACs in retinal cross-sections. Littermate control, *Megf10<sup>lacZ/+</sup>*. Vertical white lines denote IPL location. Arrowheads, SAC IPL strata. Arrows, exuberant arbor growth in mutant INL and GCL. Note that mutant somata about the IPL at P0, indicating their radial migration was similar to controls. By P1 OFF somata have moved apically.

**B:** At P3, SAC IPL sublayers remain disrupted in *Megf10* mutants. Mutant OFF SACs mostly fail to ramify arbors in IPL; instead they arborize in INL (also see Fig. 6). INL projections are absent from controls. Some ON SACs are stratified in mutants (arrowhead) but have not yet formed a continuous restricted sublayer as is seen in controls.

**C:** Individual SACs show IPL innervation deficits in *Megf10* mutants. *En-face* whole-mount view of single P0 OFF SAC IPL arbors. Mutant SAC IPL dendrites appear undifferentiated, with less branching (arrow). Their arbors cover

smaller retinal territories than SACs from wild-type (wt) littermate controls (quantified at right, mean  $\pm$  s. e. m.). Images are Z-projections of slices encompassing full IPL arbor volume. \*\*\* $p(\text{on}) < 1.0 \times 10^{-7}$ ,  $p(\text{off}) = 9.38 \times 10^{-5}$ ; one-way ANOVA/Tukey's post-hoc test. Sample size, see Methods.

Scale bars: 25  $\mu\text{m}$  (A,B); 10  $\mu\text{m}$  (C).

Figure 6

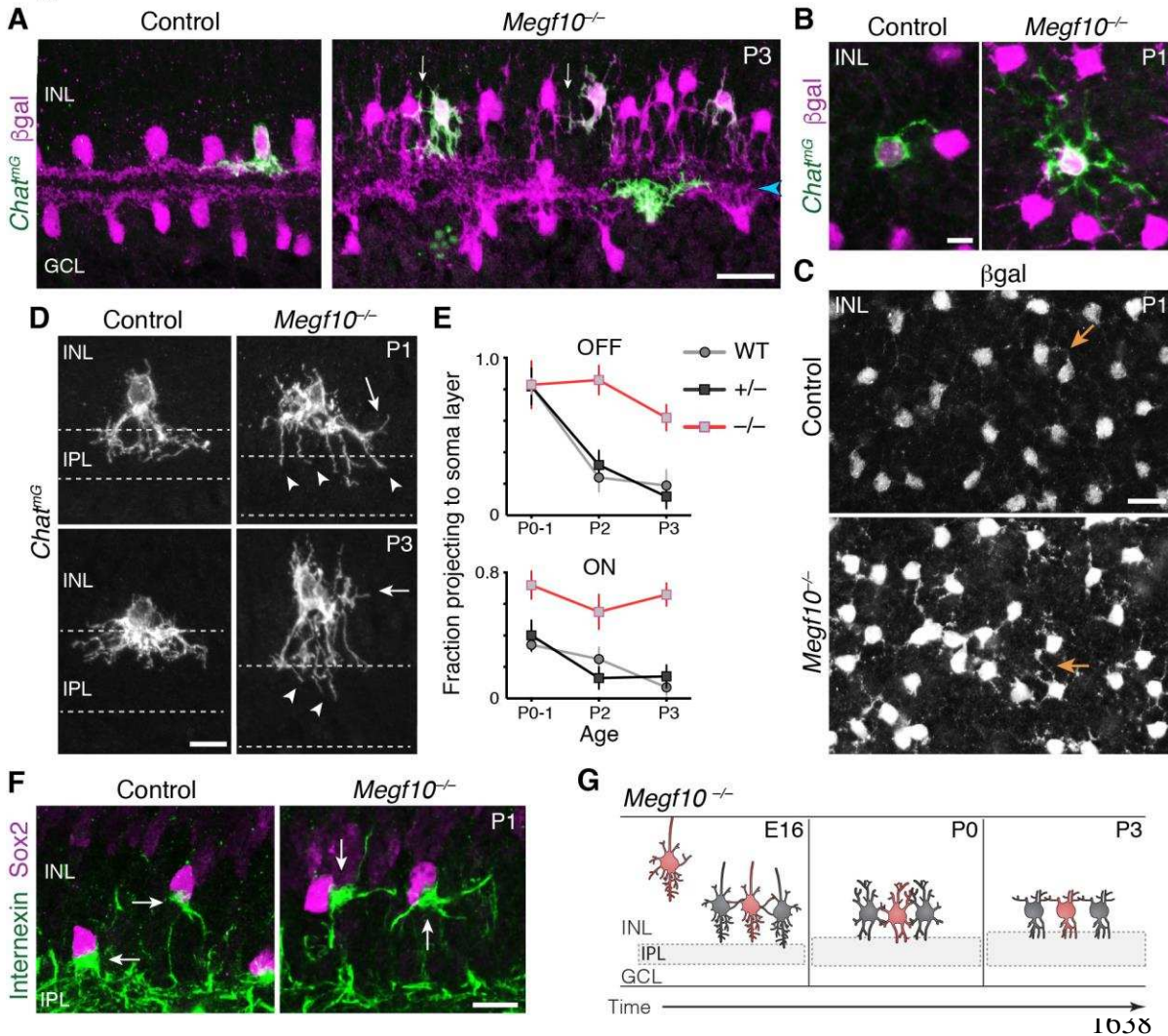


**Figure 6:**  
Exuberant  
soma-layer  
innervation by  
*Megf10* mutant  
SACs.

**A,B:** Individual SACs seen in cross-section (A) and whole-mount *en face* view (B) of *Chat<sup>mG</sup>* tissue at indicated ages. *Megf10* mutant SACs have more extensive branches in INL than littermate *Megf10<sup>+/-</sup>* control SACs. Images in B are Z-projections of confocal slices encompassing each cell's INL arbors.

**C:** *En face* images of  $\beta$ gal staining to show complete SAC INL network at P1. INL projections (arrows) are present at this age in controls (top); however, they are much more prominent in mutants (bottom), consistent with single-cell anatomy (B). Images are Z-projections of confocal slices encompassing volume of 2.0  $\mu$ m (bottom) or 2.4  $\mu$ m (top).

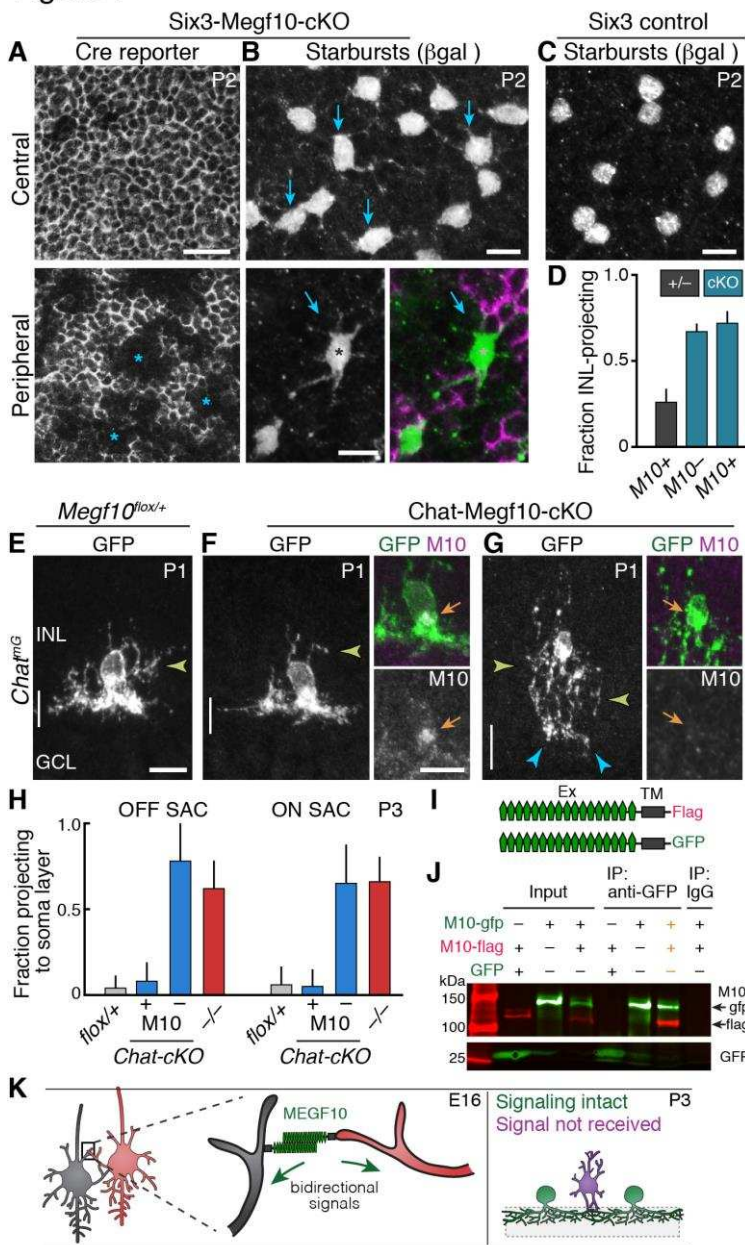
**D:** Higher-magnification view of individual OFF SACs labeled as in A. Genotypes and ages are indicated. Arrows, arbors in INL. Dashed lines denote borders of IPL. Mutant IPL projections (arrowheads) fail to arborize or stratify. See Fig. 6-Supplement 1 for ON SACs.

**E:** Frequency of soma layer projections across development in mutants ( $-/-$ ) and littermate controls ( $+/-$ ), determined from single *Chat<sup>mG</sup>* cells as in D. Wild-type (WT) data replotted from Fig. 2L to show that  $+/-$  controls resemble WT. Error bars, standard error. Sample size, see Methods.

**F:** Internexin immunoreactivity reveals orientation of SAC primary dendrites (arrows) at P1. Right: Example of mutant SACs projecting primary dendrites in tangential plane, within soma layer. Control primary dendrites were almost exclusively oriented towards IPL (left). **G:** Summary of *Megf10<sup>-/-</sup>* phenotype. After initial contact at E16, mutant SACs do not immediately innervate the IPL, instead overgrowing arbors in cell body layers. This leads to delayed sublayer formation and persistent soma-layer projections at P3.

Scale bars: 25  $\mu$ m (A,C); 10  $\mu$ m (B,D,F).

Figure 7

**Figure 7: *Megf10* mediates transcellular SAC signals for dendrite development.**

**A,B:** *En-face* images of INL in Six3-Megf10-cKO retinas stained for GFP Cre reporter (A) and  $\beta$ gal SAC marker (B). Reporter expression indicates loss of MEGF10 (see Fig. 7-Supplement 1). In central retina (top row), most SAC are mutant, and project extensive INL dendrites (B, arrows; compare to C). In peripheral retina (bottom row), some cells escape Cre (asterisks) and retain MEGF10 but still make ectopic INL projections. Purple, Cre reporter; green,  $\beta$ gal.

**C:** Littermate control retina imaged as in B; SACs rarely project INL dendrites at P2.

**D:** Quantification of P2 INL projection phenotypes illustrated in A-C. Six3-Megf10-cKO (*cKO*) SACs that escape Cre (M10<sup>+</sup>) make projection errors at similar rate as surrounding mutant cells from the same tissue (M10<sup>-</sup>).

**E-G:** *Chat-Megf10-cKO* phenotype. Morphology of single SACs, revealed by *Chat*<sup>mG</sup> in cross-sections. Anti-MEGF10 (M10) distinguished two classes of *cKO* SACs (orange arrows): Those that express MEGF10 (F) are anatomically similar to littermate control SACs (E). Those lacking MEGF10 (G) arborize extensively in INL (yellow arrowheads) but minimally in IPL (blue arrowheads). Vertical line, IPL.

**H:** SAC soma-layer projection frequency at P3. Sparse M10 deletion (blue, -) phenocopied

germline null (red). *Chat-Megf10-cKO* cells that retained M10 (blue, +) resembled controls (*flox*<sup>+/+</sup>).

**I:** Schematic of MEGF10 proteins used for co-immunoprecipitation (IP). Intracellular domain was deleted ( $\Delta$ ICD) and replaced with epitope tags (Flag or GFP). Ex, extracellular; TM, transmembrane.

**J:** Co-IP from lysates of HEK 293T cells transfected with indicated constructs (I). Western blot with antibodies to GFP (green) and Flag (red). IP with anti-GFP, but not rabbit IgG control, pulled down both MEGF10- $\Delta$ ICD constructs (2<sup>nd</sup> lane from right, orange text). IP with anti-Flag gave similar result (Fig. 7-Supplement 2). GFP alone did not co-IP with M10-Flag. Ladder molecular weights (kDa) at left. Full blots in Fig. 7-Supplement 2.

**K:** Model of MEGF10 function in early SAC dendrite development. Left, soma-layer contact between neighboring SACs initiates MEGF10-mediated signaling in each cell. This signal inhibits soma-layer dendrite growth and promotes arborization in IPL (see green cell, right panel). Purple, phenotype of SACs that fail to receive MEGF10 signals, either because neighbors do not have MEGF10, or because the cell itself lacks MEGF10 as a receptor. These SACs project exuberant soma-layer arbors and fail to ramify dendrites in IPL.

Error bars, 95% confidence interval. Sample sizes, see Methods. Scale bars: 25  $\mu$ m (A), 10  $\mu$ m (B-G).

Figure 8

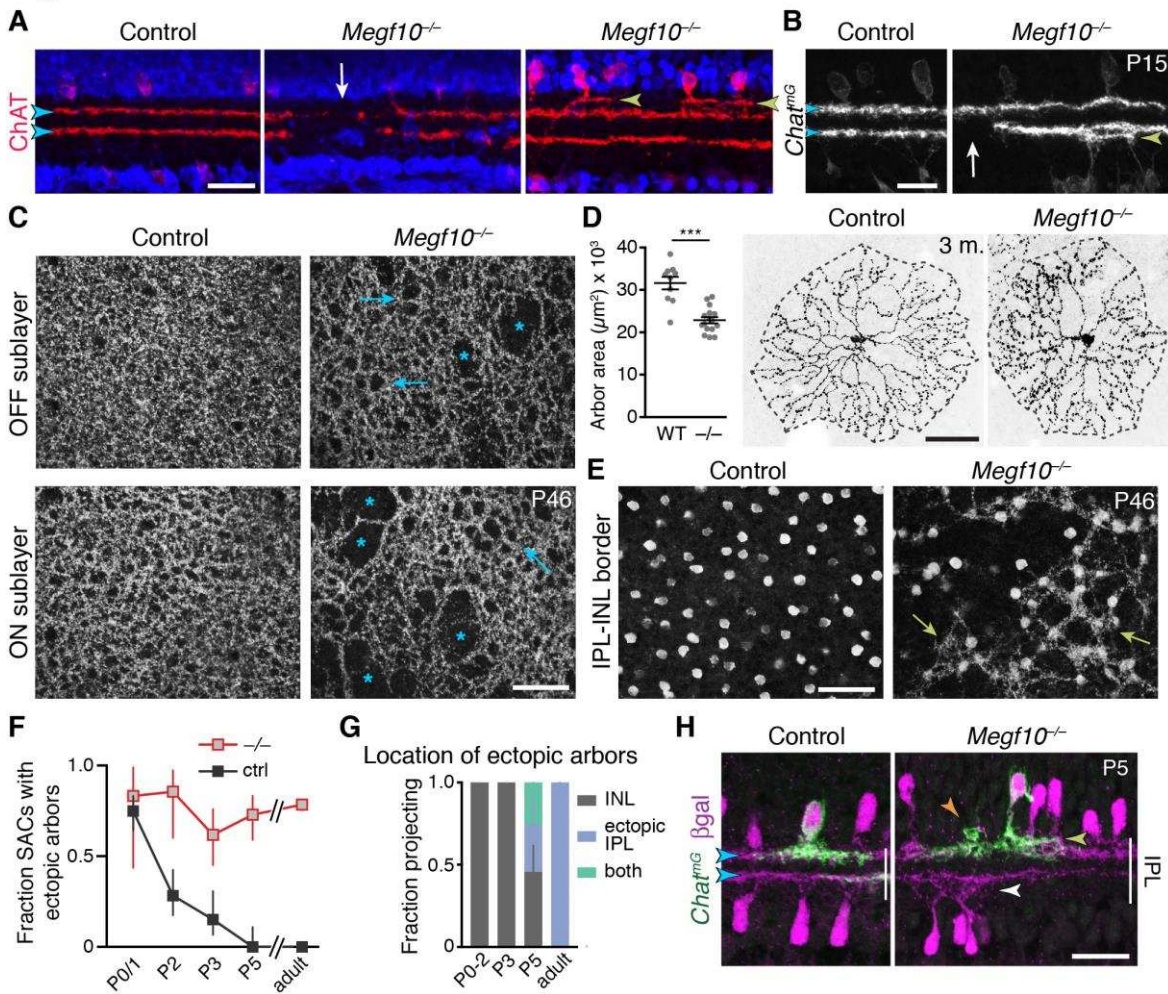


**Figure 8: SAC IPL errors persist to maturity in *Megf10* mutants.**

**A,B:** SAC IPL phenotype in mature (two-week-old) retina, cross-section view. Blue, soma counterstain. Control IPL has two continuous SAC dendrite bands (blue arrowheads). Mutant IPL has sporadic ectopic SAC arbors (yellow arrowheads) or laminar gaps (white arrows).

**C:** *En-face* views of SAC dendrites, stained with anti-

ChAT, in adult retinal whole-mounts. The same fields of view are shown at two different Z-stack planes, corresponding to OFF and ON SAC sublayers. SAC dendrite plexus is uniform in littermate controls, but has holes (arrows) and large gaps (asterisks) in mutants. Note that errors are not spatially correlated between OFF and ON sublayers. Images are Z-projections of 5 slices encompassing 2.0  $\mu\text{m}$  in Z.

**D:** Single SAC labeling in adult (3 month old) mice, via *Chat*<sup>Cre</sup>-dependent viral fluorescent protein expression. *Megf10*<sup>-/-</sup> SACs have relatively normal morphology but are significantly smaller than wild-type (WT) control cells (\*\*\*)  $p = 4.6 \times 10^{-6}$ , two-tailed *t*-test). Sample size, see Methods.

**E:** *En-face* images reveal extent of ectopic mutant SAC dendrite network. Same fields of view as C, but at different Z-planes depicting OFF IPL (at IPL-INL border). In mutant but not control, SAC dendrite fascicles (arrows) are evident at this IPL level. Images are Z-projections of 3 (left) or 2 (right) slices spaced 0.4  $\mu\text{m}$  in Z.

**F,G:** Dendrite targeting of individual OFF SACs assessed across development. Fraction of mutant SACs projecting into ectopic network does not change over time (F). However, location of ectopic arbors shifts from INL to IPL (G), starting at P5, when cells projected to either or both locations (G,H). In F, P0-3 data are replotted from Fig. 6E, with both control groups combined. Sample sizes, see Methods.

**H:** Example P5 SACs from *Megf10* mutant and littermate control. A mutant SAC projects to three different locations: 1) correct IPL sublayer (blue arrowhead); 2) ectopic IPL sublayer (yellow arrowhead); 3) ectopic INL arbor aggregate (orange arrowhead). ON SACs also make ectopic IPL projections (white arrowhead). Control cells are monostratified in IPL (left). Note that SAC sublayers have formed by P5 in mutants.

Error bars, 95% confidence intervals. Scale bars: 50  $\mu\text{m}$  (C-E); 25  $\mu\text{m}$  (A,B,H).

Figure 9

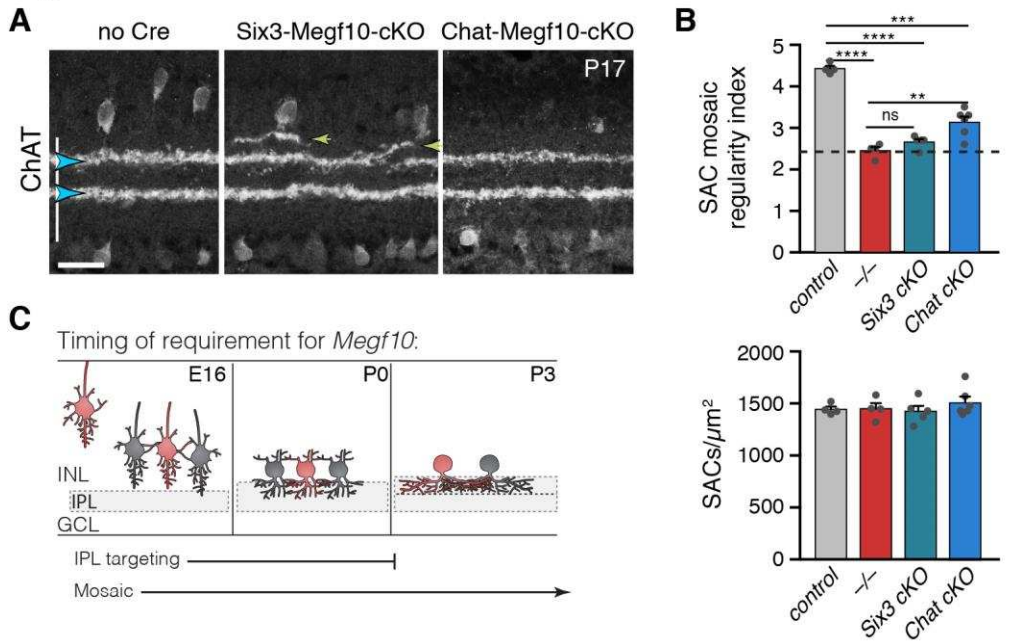


**Figure 9: Temporal requirements for MEGF10 in SAC IPL stratification and mosaic spacing.**

**A:** SAC IPL errors (yellow arrowheads) induced by early deletion of *Megf10* in *Six3-Megf10-cKO* mice, but not deletion between P3-5 in *Chat-Megf10-cKO* mice (see Fig. 7-Supplement 1 for MEGF10 expression in these strains). Blue arrowheads, SAC sublayers.

**B:** Mosaic spacing phenotype measured at P17 using Voronoi domain

regularity index (top graph). Dashed line, index for simulated random SAC arrays. In both *Six3* and *Chat* conditional mutants, SAC positioning is less regular than in controls (*Chat<sup>Cre</sup>; Megf10<sup>lox/+</sup>*). *Megf10<sup>-/-</sup>* and simulation data from Kay et al. (2012). ns,  $p = 0.6438$ ; \*\* $p = 0.0023$ ; \*\*\* $p = 2.1 \times 10^{-6}$ ; \*\*\*\* $p < 1.0 \times 10^{-6}$  (one-way ANOVA/Tukey's post-hoc test). Bottom graph, regularity effects are not due to changes in SAC cell density across genotypes. One-way ANOVA,  $F(3, 15) = 0.6063$ ;  $p = 0.6210$ .

**C:** Summary of results from all conditional *Megf10* mutant studies (A, B; Fig. 7). Loss of MEGF10 while soma-layer arbors are present (i.e. prior to P3) disrupts both SAC mosaic patterning and IPL laminar targeting; this conclusion is based on phenotypes of: 1) germline mutant; 2) *Six3-Megf10-cKO* mutant; 3) occasional cells in *Chat-Megf10-cKO* mice that lost MEGF10 prior to P3 (Fig. 7F-H). When MEGF10 is lost after P3, as is the case for most *Chat-Megf10-cKO* SACs (Fig. 7-Supplement 1), only mosaic is disrupted (A,B). Thus, MEGF10 acts at distinct, albeit partially overlapping times, to influence these two distinct SAC developmental events.

Error bars, S.E.M. Scale bar, 25 $\mu\text{m}$ .

Figure 10

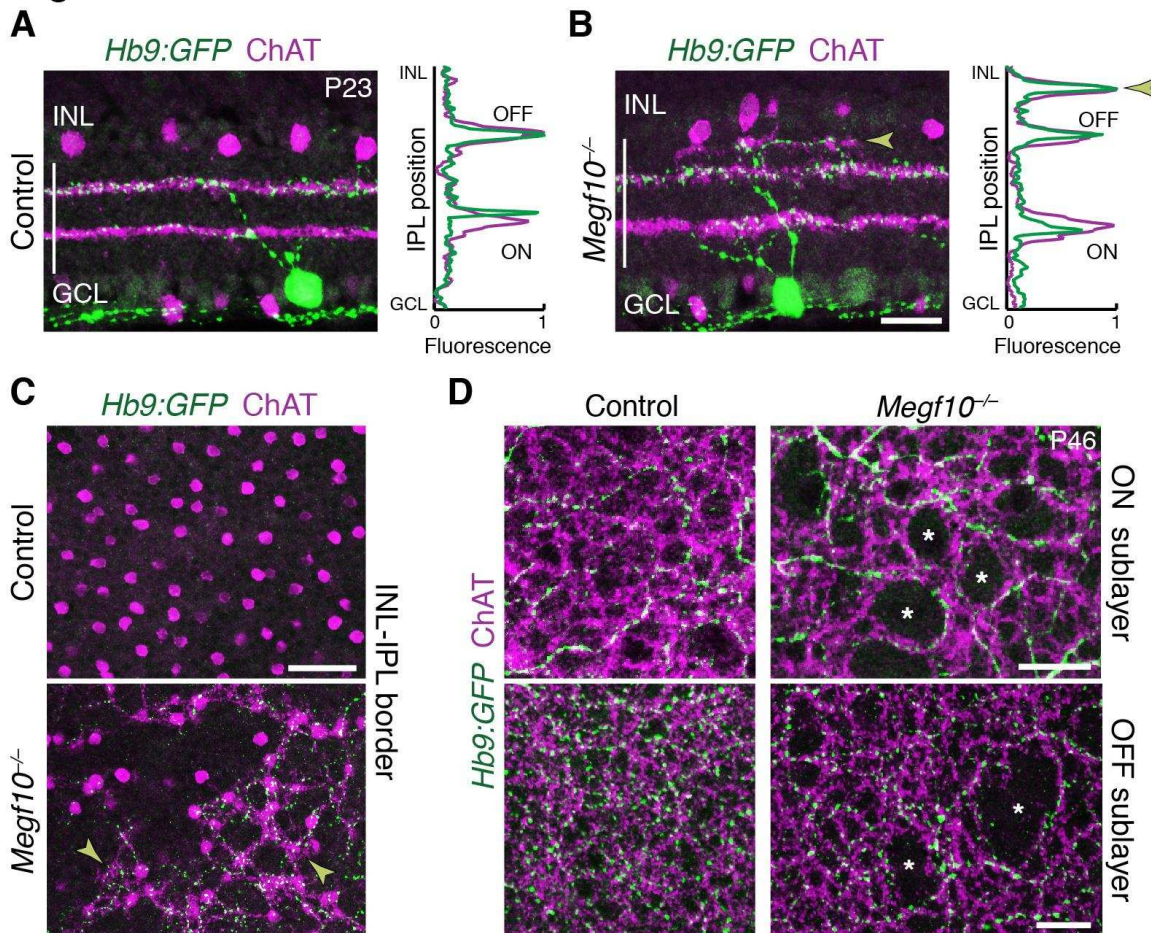


**Figure 10: SACs guide IPL sublayer choice by ooDSGCs.**

**A,B:** SACs (ChAT, purple) and ooDSGCs (Hb9-GFP, green) labeled in cross-sections. Right panels, fluorescence profile plots across IPL showing position of ON and OFF sublayers. In both controls (A) and *Megf10* mutants (B) ooDSGC dendrites strictly co-localize with SAC arbors. Arrowhead (B), ectopic sublayer.

**C:** *En-face* view of OFF IPL near INL border. Same fields

of view as Fig. 8E. In *Megf10* mutants (bottom), the ectopic SAC network is extensively innervated by ooDSGC dendrites (arrowheads). Control retina (top) lacks DS circuit arborization at this IPL level.

**D:** *En-face* view of ON (top) and OFF (bottom) SAC IPL sublayers. In *Megf10* mutants, ooDSGC dendrites (green) fail to enter IPL regions (asterisks) that are not innervated by SACs (purple).

Images in C,D are Z projections of confocal slices encompassing  $\geq 1.2 \mu\text{m}$  (C) or 2-4  $\mu\text{m}$  (D).

All scale bars: 25  $\mu\text{m}$ . Also see Fig. 10-Supplement 1 for phenotype of *Drd4-GFP* ooDSGCs.

801

802

Figure 11

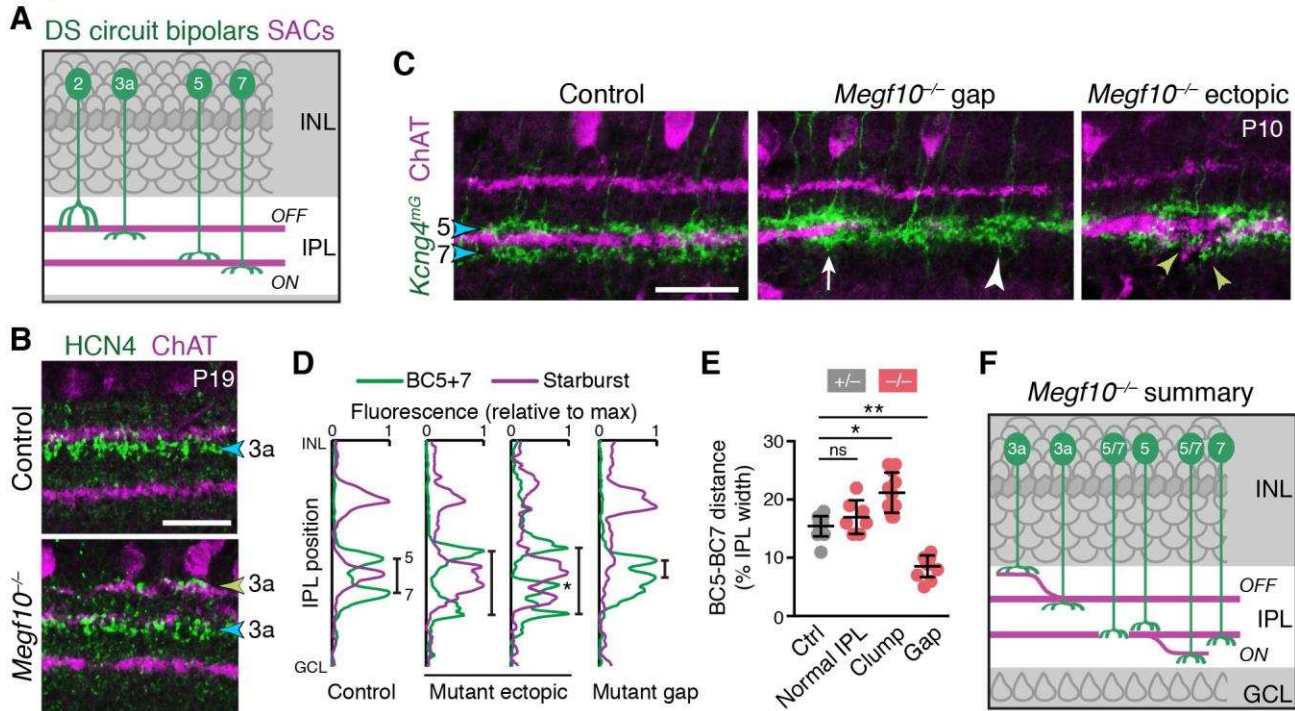


**Figure 11:** SACs guide IPL sublamina targeting by DS circuit bipolar cells.

**A:** Illustration depicting anatomy of four bipolar cell types known to participate in DS circuit. BC3a, BC5, and BC7 arborize axons in narrow sublayers directly adjacent to SAC strata. BC2 projects more broadly through OFF IPL, overlapping with SAC sublayer (see Fig. 11-Supplement 1).

**B:** BC3a IPL projections assessed with anti-HCN4. Blue arrowhead, normal BC3a stratum. Yellow arrowhead, ectopic stratum containing SAC dendrites (purple) and BC3a axons (green).

**C,D:** BC5 and BC7 IPL projections (blue arrowheads), labeled in *Kcng4<sup>mG</sup>* mice. D, images; E, representative fluorescence plots of *Kcng4<sup>mG</sup>* (green) and ChAT (purple) across IPL. In littermate controls, or normal regions of mutant IPL (C, arrow), BC5 and BC7 arborize in sublayers immediately adjacent to ON SAC layer, but do not enter it. In *Megf10* mutants, ectopic SAC arbors displace BC5+7 terminals to new IPL locations, where they remain adjacent to SACs but non-overlapping (C, yellow arrowheads; D, center plots). Asterisk (D): ectopic BC arbors between normal and ectopic SAC strata. BC5/7 arbors can innervate gaps in the SAC stratum (C, center panel); in these cases their terminals are abnormally close together (C, white arrowhead; D, right plot). Vertical bars in D: distance between BC5/7 strata.

**E:** Quantification of BC5-BC7 distance in normal IPL and in presence of SAC innervation gaps or ectopic arbor clumps. \* $p = 0.0219$ ; \*\* $p = 0.0012$ ; ns,  $p = 0.3965$  (Tukey's post-hoc test). Sample sizes, see Methods. Error bars, S.E.M.

**F:** Summary of *Megf10<sup>-/-</sup>* bipolar cell phenotypes. BC3a, BC5, and BC7 are illustrated here (see Fig. 11-Supplement 1 for BC2). Each of these cell types can either make errors (left cell in each pair) or project normally (right cell). All three cell types show recruitment to ectopic IPL locations. BC5 and BC7 terminals innervating SAC gaps colonize the sublayer normally occupied by SACs.

Error bars, 25  $\mu\text{m}$ .

Figure 12

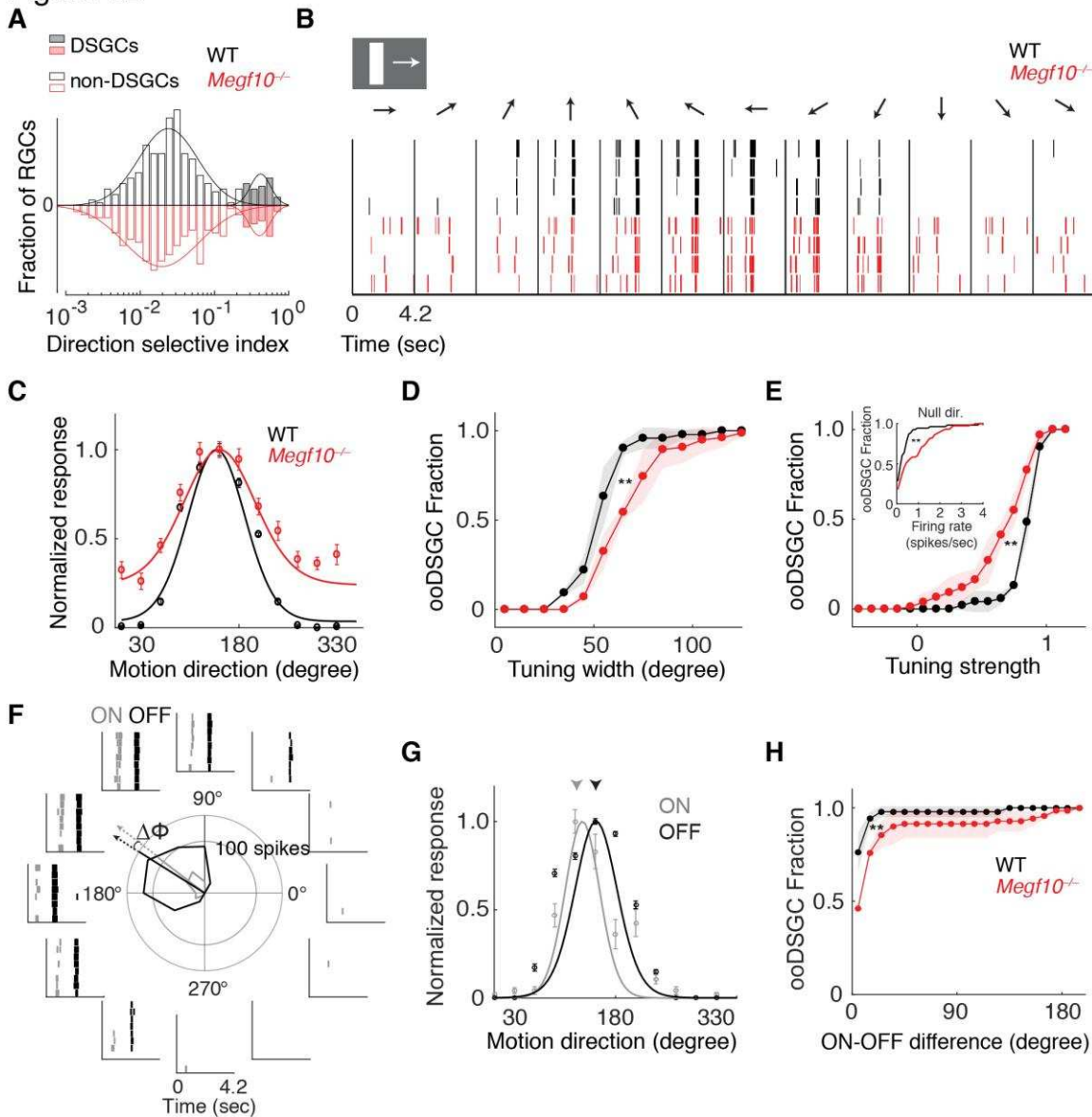


**Figure 12:**  
Broader and weaker  
direction tuning of  
oodSGCs in  
Megf10 mutants.

**A:** Histograms of RGC direction selectivity indices, measured on a multielectrode array, for wild-type (WT, black) and *Megf10*<sup>-/-</sup> (red) retinas. Bimodal histograms fit with two-Gaussian mixture model distinguished DSGCs (filled bars) from non-DSGCs (open bars).

**B:** Spike rasters from representative WT and *Megf10*<sup>-/-</sup> posterior-preferring oodSGCs in response to a bright bar moving along 12 directions (arrows).

**C:** Direction tuning

curves from cells in B normalized to the maximum response (line: von Mises fit). Non-zero values at tails of mutant curve reflect increase in null-direction spikes (B, left- and right-most bins).

**D,E:** Cumulative distribution of tuning widths (D) and tuning strengths (E) for all oodSGCs recorded from two retinas of each genotype (WT *n* = 80 cells; *Megf10*<sup>-/-</sup> *n* = 74 cells). Mutant oodSGC population is tuned more broadly (D, right shift of red curve) and more weakly (E, left shift of red curve) than WT. Similar results were obtained when ON and OFF responses were considered separately (not shown). Mutant oodSGCs also exhibit higher firing rate to null direction motion (E, inset). \*\**p* = 0.005 (D), *p* = 0.003 (E), paired KS-test.

**F:** Rasters and polar plot of a representative WT oodSGC, highlighting preferred directions of ON (gray) and OFF (black) responses (arrows).  $\Delta\phi$ , angular difference between preferred directions of ON and OFF responses.

**G:** ON and OFF direction tuning curves for cell in F (line, von Mises fit). ON and OFF preferred directions (arrowheads) are well aligned in WT retina.

**H:** Cumulative distribution across all oodSGCs of ON-OFF preferred direction difference ( $\Delta\phi$ ). Same cells as in D,E. Rightward shift of mutant curve indicates larger ON-OFF misalignment. \*\**p* = 0.004, paired KS test.

For all panels, background light level was photopic ( $10^4$  P\*/M-cone/sec; contrast of moving bar was 60%). Error bars/bands, S.E.M. Also see Fig. 12-Supplement 1.

Figure 1 - Supplement 1

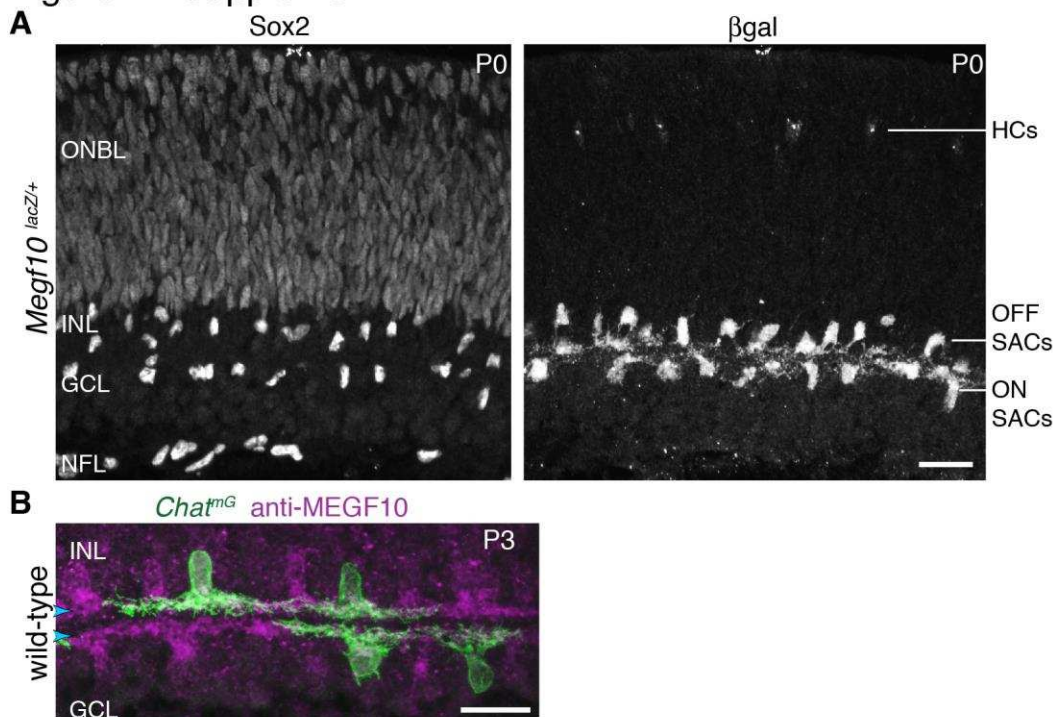


**Figure 1-Supplement 1:**  
Characterization of SAC  
markers in neonatal retina.

**A:** Sox2 and *Megf10* as SAC markers at P0. Individual color channels of P0 cross-section image shown in Fig. 1B. Sox2 (A, left panel) is a pan-SAC nuclear marker. Antibodies to Sox2 strongly label all SACs in the inner nuclear layer (INL) and ganglion cell layer (GCL), as well as astrocytes in the nerve fiber layer (NFL). Progenitor cells in the outer neuroblast layer (ONBL) are weakly labeled. Antibodies to βgal

(A, right panel) label the complete SAC population in *Megf10<sup>lacZ</sup>* mice. Horizontal cells (HCs) in outer retina are also labeled.

**B:** Antibodies to MEGF10 (purple) are selective for SACs and label the complete SAC population. *Chat<sup>mG</sup>* mice (i.e. *Chat<sup>Cre</sup>* crossed to membrane-targeted GFP Cre reporter) label a subset of SACs in the neonatal retina (green). Whereas *Chat<sup>Cre</sup>* is a marker of the full SAC population at later stages, its expression in neonatal retina is more sporadic (Xu et al., 2016). We took advantage of this feature for two purposes: 1) Single-cell anatomy studies of SAC dendrite morphology, as shown here; and 2) sporadic early knock-out of genes in a sparse subset of SACs (See Fig. 6).

Scale bars: 25 μm.

## Figure 1 - Supplement 2

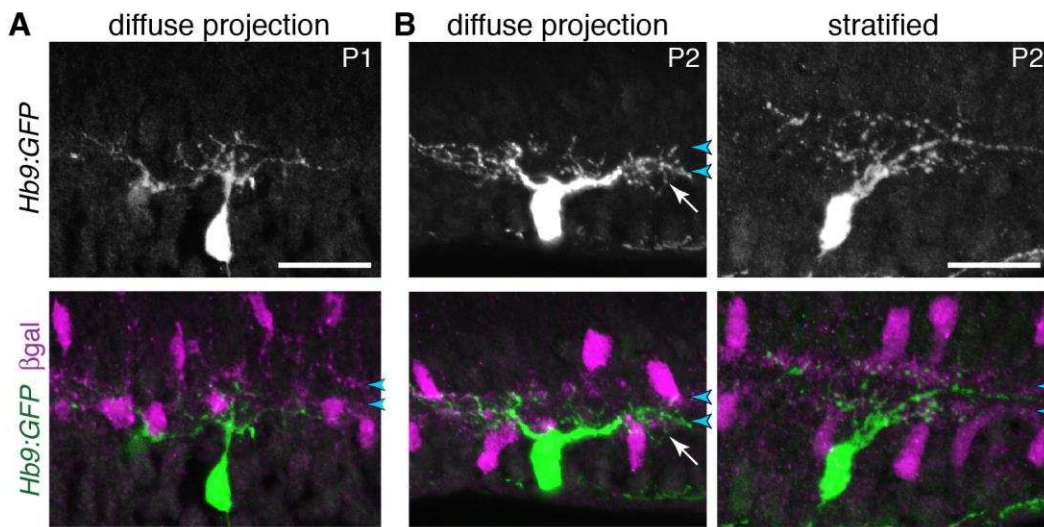


**Figure 1-Supplement 2:**  
oODSGC stratification in  
neonatal retina.

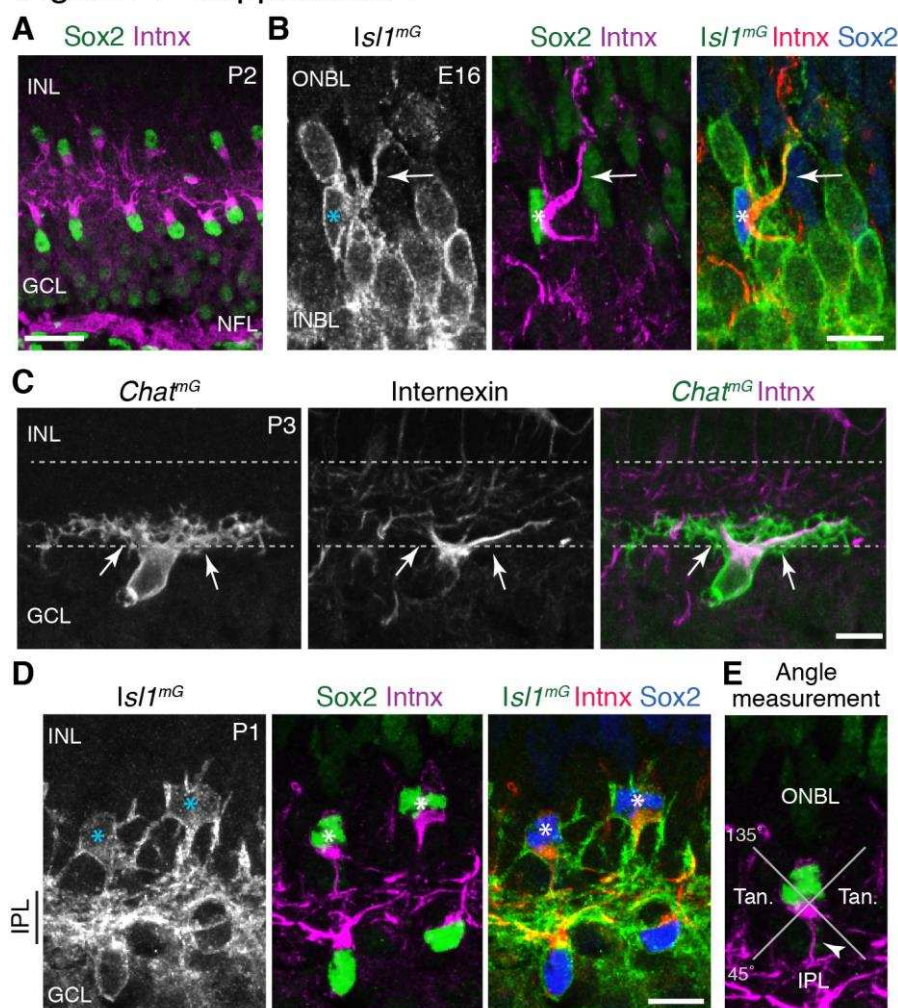
**A:** Anatomy of P1 oODSGCs labeled with *Hb9-GFP*. SACs are labeled by *Megf10:βgal*. At this age, oODSGC dendrites are rudimentary with few branches. No IPL stratification is evident. This cell was used for the IPL fluorescence plot shown in Fig. 1E.

**B:** Examples of P2

oODSGCs that were scored as diffusely-projecting (left) or stratified (right). Blue arrowheads, SAC sublayers. Arrow (center panel), arbors that fill IPL in area between SAC strata. See main text for quantification of stratification frequency.

Scale bars: 25 μm.

## Figure 2 - Supplement 1

**Figure 2-Supplement 1:****Characterization of internexin as a primary dendrite marker of developing SACs.**

**A:** Expression pattern of internexin in P2 mouse retina. Internexin (Intnx) immunoreactivity is detected in Sox2<sup>+</sup> SACs, and in RGC axons within the nerve fiber layer (NFL). This pattern is typical of the entire first postnatal week. In RGCs, axons are selectively labeled; their cell bodies in the GCL are internexin-negative. In SACs, internexin selectively labels primary dendrites, as well as the portion of the soma from which the primary dendrites arise. Therefore, internexin<sup>+</sup> intermediate filaments are trafficked to specific subcellular compartments of both SACs and RGCs. P2 SACs are strongly polarized towards the IPL (also at P1; see D). Note that this image is the same one depicted in Fig. 2E, but cropped differently; also, colors have been reversed to match other panels of this figure.

**B:** An individual E16 INBL SAC (asterisk), surrounded by *Isl1*<sup>mG</sup>-positive RGCs (identified as RGCs because they lack Sox2 or internexin staining). At E16, internexin has the same subcellular localization within SACs as at P1-2 (A,D): It localizes to the primary dendrites (arrow) and the side of the cell body from which it emerges. However at E16, SAC primary dendrite orientation is more variable than at P2 (see Fig. 2E,F). This SAC sends a primary dendrite towards the outer retina (ONBL) where it could potentially contact migrating SACs as they arrive at the INBL.

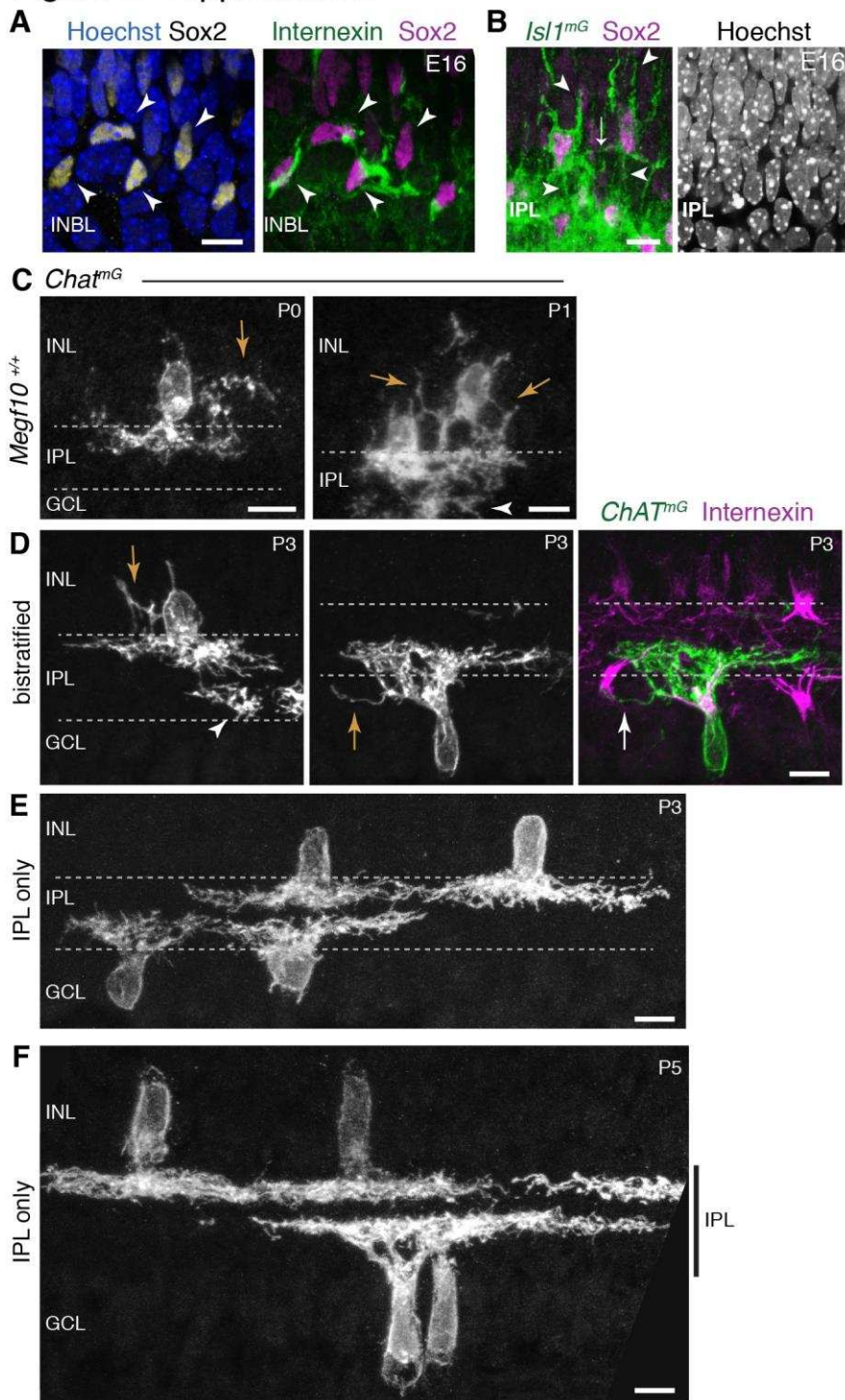
**C:** Antibodies to internexin strongly label SAC primary dendrites originating from the cell body (arrows), but fine dendritic branches within IPL are unlabeled. Occasionally, higher-order branches arising from the primary dendrites are weakly labeled. *Chat*<sup>mG</sup> was used to reveal the full dendritic arbor.

**D:** Internexin distinguishes IPL-directed primary dendrites from soma-layer arbors in neonatal SACs. *Isl1*<sup>mG</sup> labels full morphology of bi-laminar P1 OFF SACs (asterisks) that project to both INL and IPL. Only IPL-directed primary dendrites of these cells are internexin-positive (middle, right panels).

**E:** Schematic of method used to measure primary dendrite orientation (Fig. 2F). For each cell, the angle between the primary dendrite (arrowhead) and a plumb line directed to IPL was measured. Cells projecting within the labeled quadrants were defined as projecting towards IPL, towards ONBL, or tangentially (Tan).

Scale bars: 25  $\mu$ m (A), 10 $\mu$ m (B-D).

## Figure 2-Supplement 2

**Figure 2-Supplement 2: Soma-layer SAC arbors across development.**

**A:** E16 soma-layer arbor network can be established prior to IPL formation. Right panel, same cells as Fig. 2E, showing INBL SACs projecting towards each other. Left panel, same field of view showing Sox2 SAC nuclear marker and Hoechst nuclear stain (blue). These SACs are surrounded by other INBL cell bodies, with no IPL neuropil evident in this retinal region.

**B:** E16 homotypic SAC soma contacts occur outside the IPL. Left panel, same cells as Fig. 2D. Cells have migratory morphology, as shown by their prominent apical and basal processes (arrowheads). They do not make obvious projections into IPL, delineated by dense *Isl1<sup>mG</sup>* staining. Contact between the two SACs (arrow) occurs outside of IPL. Right panel, Hoeschst nuclear stain confirms location of nascent IPL inferred from *Isl1<sup>mG</sup>* labeling. IPL is narrow cell-free gap that corresponds to location of dense GFP<sup>+</sup> arbors (left panel).

**C:** Examples of soma layer-projecting *Chat<sup>mG</sup>*-labeled SACs in mice that are wild-type at the *Megf10* locus (*Megf10<sup>+/+</sup>*), demonstrating that the soma-contacting arbors shown in Fig. 2H-K are not a consequence of *Megf10* heterozygosity. Arrows, arbors in INL. Arrowhead, arbor of a neighboring ON SAC with cell body located in adjacent section.

**D-F:** Examples of P3 (D-E) and P5 (F) cells used to generate graph in Fig. 2L. SAC single-cell morphology was revealed using *Chat<sup>mG</sup>* labeling. At P3, most SACs project only to the IPL (E), but some SACs still make soma-layer projections (D). Representative INL-projecting OFF cell (D, left) and GCL-projecting ON cell (D, center, right) are depicted. The ON cell makes contact with the neighboring internexin-positive SAC soma (arrow in right panel of D). Arrows, soma-layer projecting arbors. Arrowhead, arbor of a neighboring ON SAC only partially present in the section. At P5 (F), all SACs project exclusively to IPL (vertical bar).

All scale bars: 10  $\mu$ m.

## Figure 2 - Supplement 3

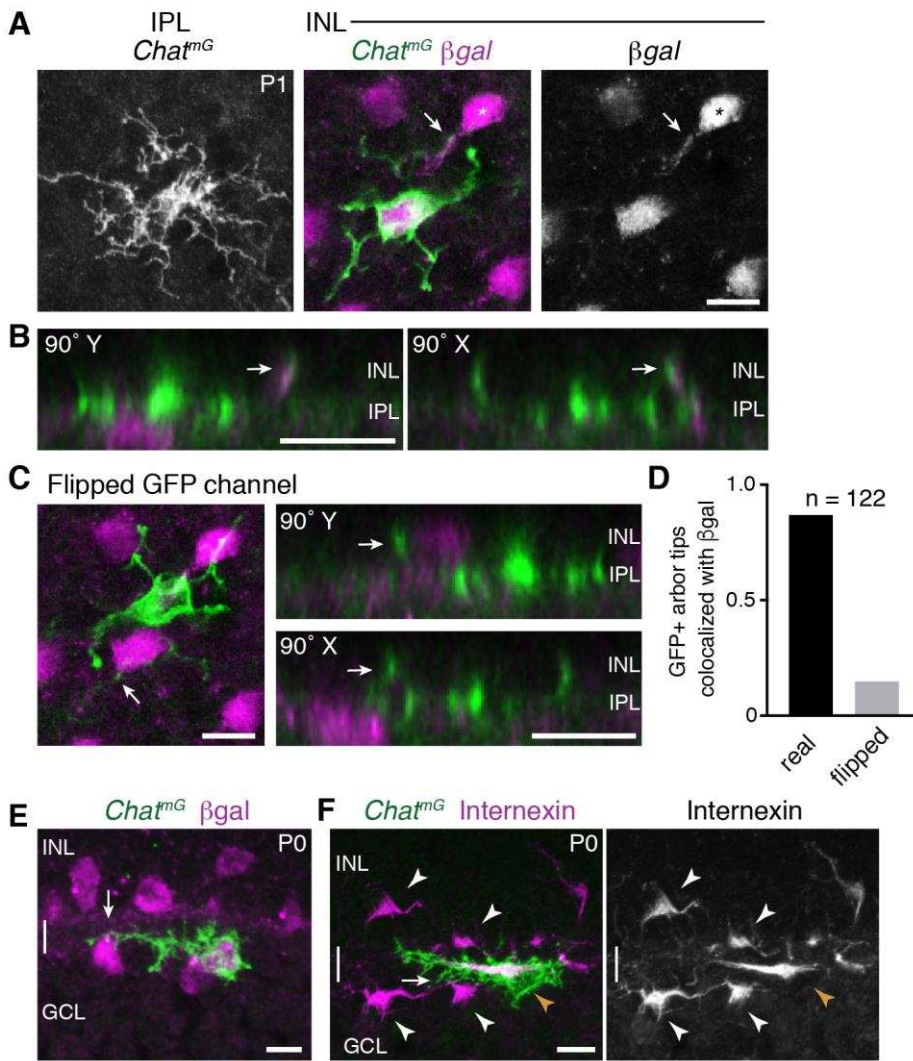


**Figure 2-Supplement 3:**  
Homotypic specificity of soma-layer SAC projections.

**A:** Single SAC from P1 *Chat<sup>mG</sup>* retinal whole-mount, imaged at level of IPL (left) and INL (center, right). *Megf10:βgal* marks the full SAC population. INL images are from a single confocal Z-stack plane. A GFP+ arbor tip that terminates on a βgal-positive neighboring SAC is marked (arrow, arbor tip). Most of the cell's other arbor tips are outside this focal plane, where several terminate on other SACs (not shown). IPL image is a maximum-intensity projection of 3 Z-stack slices (1.5 μm total distance).

**B:** Orthogonal (90° rotation) views of a Z-stack (0.5 μm Z resolution) through the cell shown in A. Left, Y-axis rotation; right, X-axis rotation. Arrows mark the same interacting INL arbors as in A. Note colocalization of green and purple arbors regardless of whether cell is viewed *en face* (A), or from the orthogonal perspectives (B).

**C:** The same cell as in A but with the GFP channel flipped in X and Y. This serves as a negative control to test whether superposition of GFP and βgal signals might occur by chance, given the density and geometry of each staining in the P1 retina. Arrows mark same arbor tip as in A,B. In *en face* view (left), the arbor crosses a βgal<sup>+</sup> cell body but terminates just beyond it. The lack of colocalization between this arbor tip and the adjacent cell body is clear in orthogonal rotation views (right).

**D:** Quantification of INL arbor homotypic specificity. The fraction of *Chat<sup>mG</sup>*-labeled SAC dendrite arbor tips terminating on βgal<sup>+</sup> neighbors was counted by examining z-stacks and orthogonal views (as in B). This was done for real image stacks, as well as for stacks with one channel flipped as in C. A high rate of homotypic interaction was observed for the real data (88.8%) but not the flipped negative control data (14.9%). Sample size,  $n = 122$  arbors from 22 SACs, two retinas each genotype.

**E,F:** ON SACs can contact neighboring SAC somata (arrows) without being bi-laminar. Cross-sections of P0 retina, co-stained for individual SACs (*Chat<sup>mG</sup>*) and markers of the complete SAC population (E, *Megf10:βgal*; F, internexin). The two cells shown here establish soma contact without a separate GCL projection; instead, these cells send fine branches from their IPL arbors to establish contact. These cells are representative of a phenomenon that was observed frequently among ON SACs at P0. The existence of such cells may help explain why the frequency of soma layer-projecting ON SACs is lower than for OFF SACs (Fig. 2L). Internexin staining (F) shows that these ON SACs (orange arrowhead) are polarized in the tangential plane along the INL-

049 GCL border towards their neighbors, adopting a horizontal morphology distinct from surrounding OFF and  
050 ON SACs (white arrowheads). This morphology is typical of a displaced amacrine cell in the process of  
051 crossing from the INL to the GCL (Chow et al., 2015).

052 Scale bars: 10  $\mu$ m.

053

## Figure 3 - Supplement 1

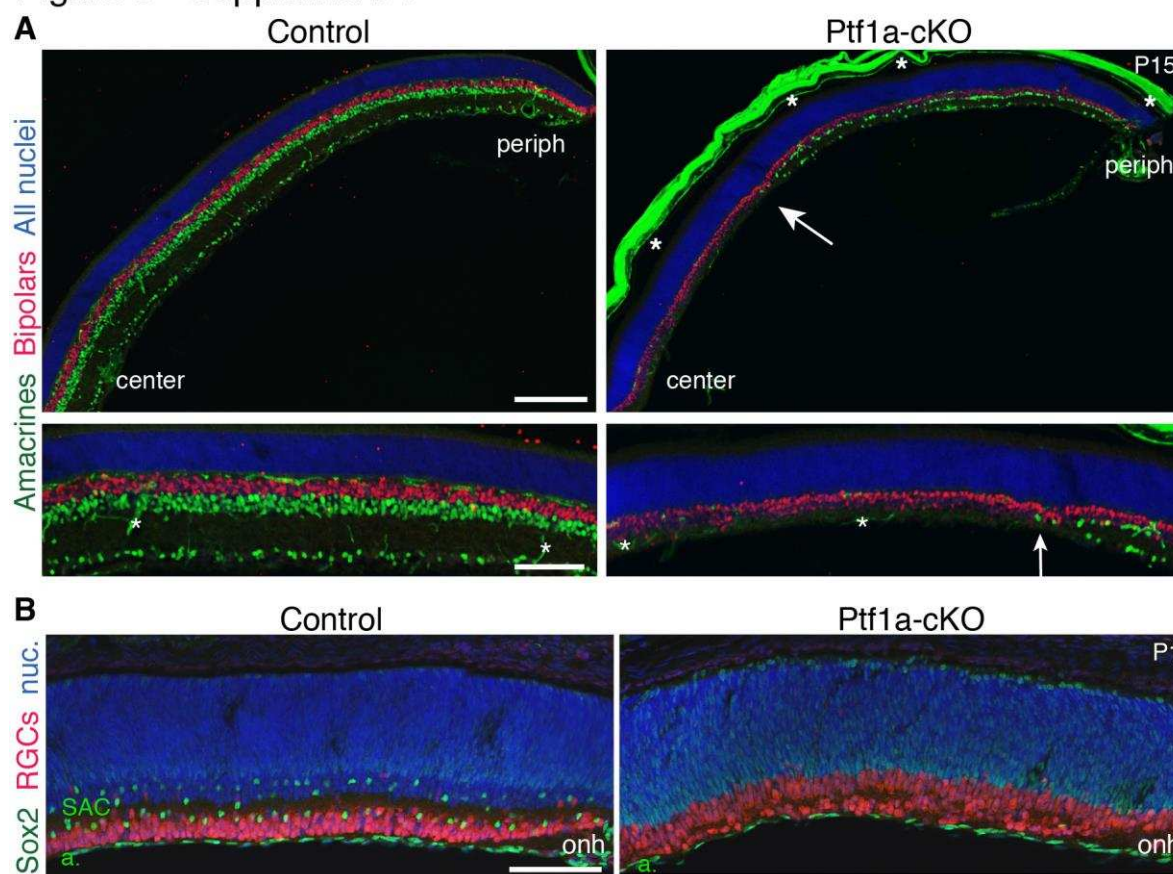


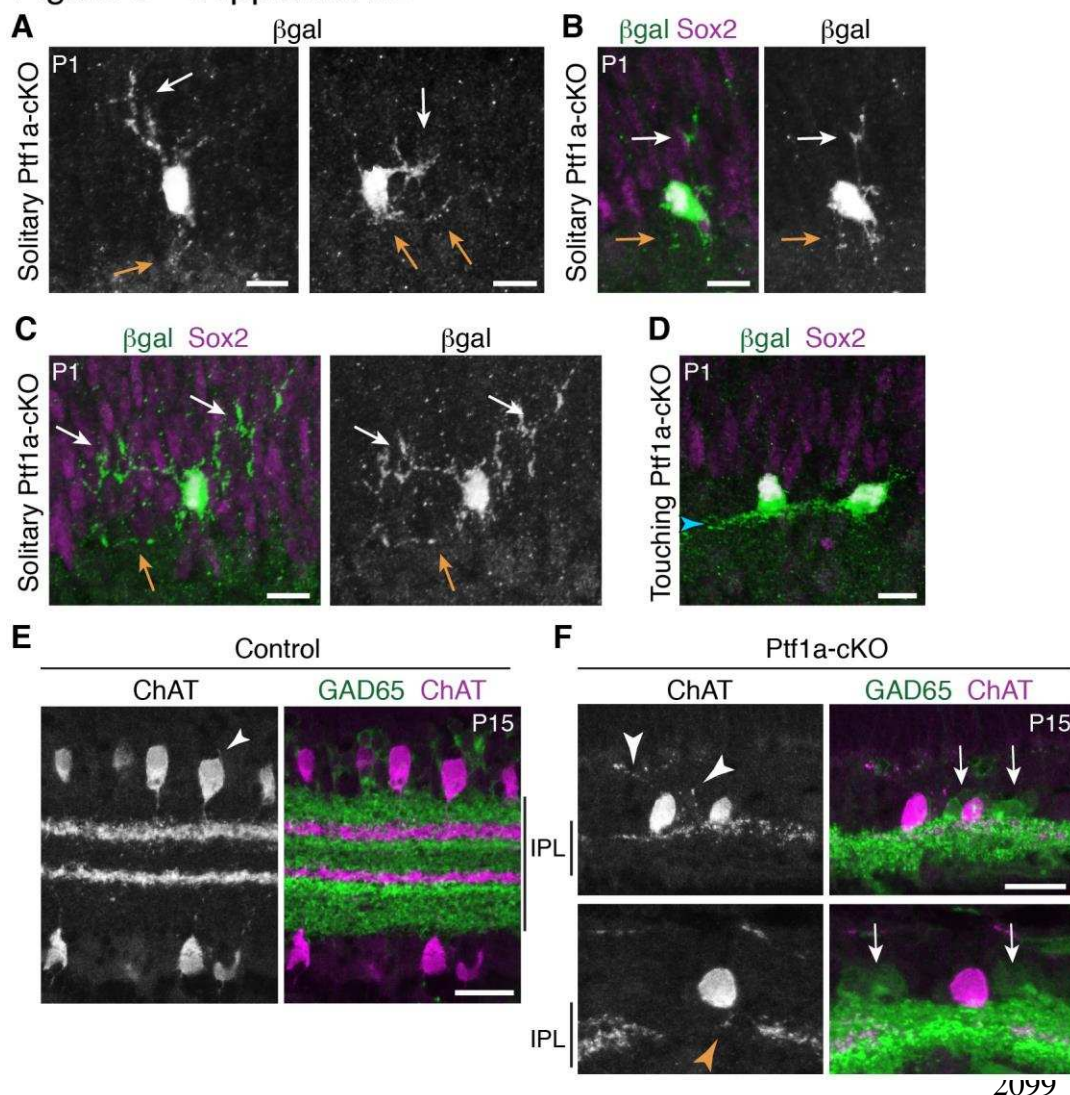
**Figure 3-Supplement 1: Retinal cell types in *Ptf1a*-cKO mutants.**

**A:** Immunostaining with pan-amacrine marker AP2 $\alpha$  (green) and pan-bipolar marker Chx10 (red), in littermate control and *Ptf1a*-cKO retinal cross sections. Blue, Hoechst nuclear counterstain. Top panels: low-power view illustrating center-peripheral differences in amacrine number that arise due to Cre expression pattern (see Fig. 3A-C). Bottom panels: Higher magnification views of mid-peripheral retina. AP2 $\alpha$ <sup>+</sup> cells are completely eliminated from *Ptf1a*-cKO central retina. Some amacrine cells that have escaped Cre recombination (see Fig. 3C) are produced in the periphery, albeit at lower density than controls. Arrow marks central-most amacrine cells. Bipolar cell number is not obviously different between genotypes. Asterisks, non-specific staining, due to anti-mouse secondary antibody, in blood vessels and sclera. Note that sclera became detached from control section prior to imaging.

**B:** Cross-sections through central retina of littermate control and *Ptf1a*-cKO mutant, stained for pan-RGC marker RBPMS (red) and Sox2 (green) to mark SACs. Blue, Hoechst nuclear counterstain (nuc). Optic nerve head (onh) marks center of retina. In *Ptf1a*-cKO mice, SACs are entirely absent from central retina, but Sox2<sup>+</sup> astrocytes (a) in nerve fiber layer are present in normal numbers. RGC cell number appears to be increased, consistent with previous observations in embryonic retina of *Ptf1a* null mice (Fujitani et al., 2006; Nakhai et al., 2007).

Scale bars: 200  $\mu$ m (A top); 100  $\mu$ m (A bottom, B).

Figure 3 - Supplement 2

**Figure 3-Supplement 1:**  
**SAC anatomy in Ptf1a-cKO mutants.**

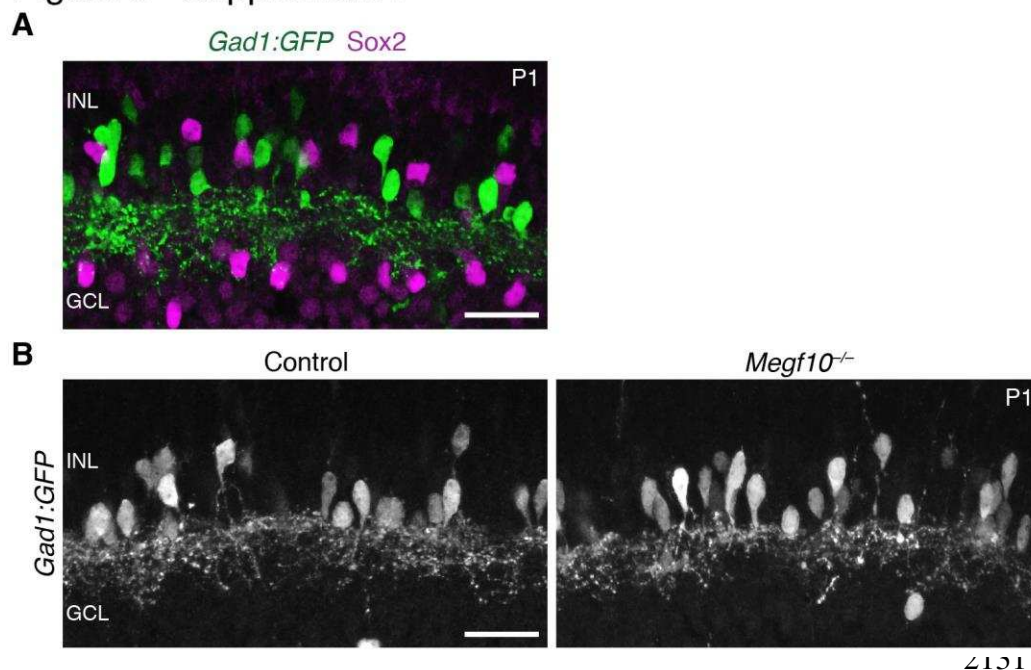
**A-D:** Additional representative examples of SACs in Ptf1a-cKO retinal cross-sections, from dataset used to compile graph in Fig. 3G. Neurons were validated as SACs by co-expression of *Megf10*: $\beta$ gal and Sox2. Touching SACs (D) stratify their arbors normally (arrowhead). Note that the right-hand cell appears to be polarized towards the left-hand cell, suggesting asymmetric growth towards the side with homotypic contact and away from the side lacking it. Representative solitary SACs are shown in A-C. A depicts same cells as Fig. 3F ( $\beta$ gal channel only) in grayscale

to highlight arbor morphology. Two cells (A, left; B) are examples of the class that failed to project to the IPL. The other cells (A, right; C) exemplify the class that sends only abnormal unbranched, unstratified arbors into the IPL. The cell in C also has particularly exuberant arbors in the INL that were much larger than those seen in any cells that touched their neighbors (e.g. D; also see Fig. 3D,E). White arrows, soma-layer arbors. Orange arrows, IPL arbors.

**E,F:** SAC errors in Ptf1a-cKO mutants persist to maturity. P15 littermate control (E) and mutant (F) retinal cross-sections stained for anti-ChAT to label SACs (red) and anti-GAD65 to label a broad non-SAC amacrine population (green). Control SACs no longer have soma layer arbors at this age; the only processes not directed toward the IPL were very short and minimal (E, arrowhead). In mutant retina, SACs from low-density regions often innervated the INL (F, white arrowheads), or failed to innervate gaps in the SAC IPL network (F, orange arrowhead). SACs that made errors likely interacted in the IPL with GAD65<sup>+</sup> amacrine cell arbors (F, arrows) because these arbors completely filled the IPL in the region innervated by the SAC dendrites. This suggests that generic amacrine contacts are not sufficient to prevent SAC errors. Instead, because these SACs had few homotypic neighbors, the errors were likely due to paucity of SAC-SAC interactions.

Scale bars: 10  $\mu$ m (A-D); 25  $\mu$ m (E,F).

## Figure 5 - Supplement 1



controls carrying *Gad1-GFP*. Unlike SACs (Fig. 5A), *Gad1-GFP*<sup>+</sup> amacrine cells innervated the INL normally in *Megf10* mutants, and did not make exuberant projections within the INL.

Scale bars: 25 μm

## Figure 6 - Supplement 1

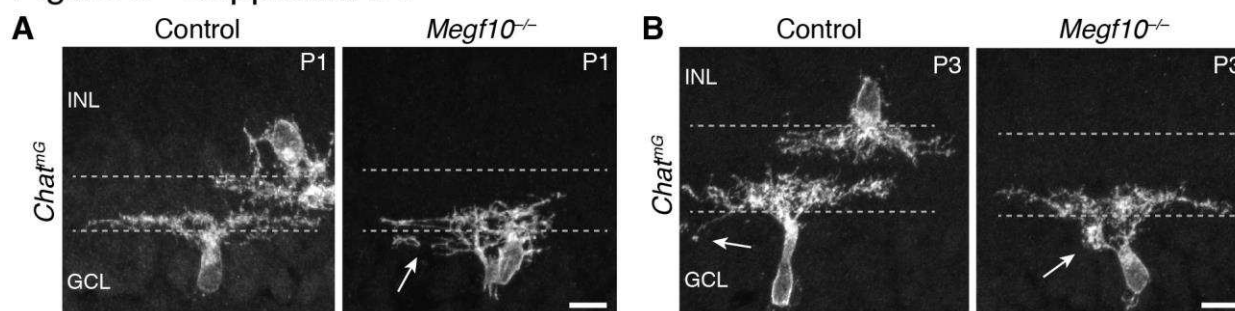


**Figure 6-Supplement 1: ON SACs also make exuberant soma-layer projections in *Megf10* mutants.**

**A,B:** Examples of P1 (B) and P3 (C) *Chat*<sup>mG</sup>-labeled ON SACs that were part of the dataset used to generate graphs in Fig. 6E. At P1 (B) many mutant ON cells are bi-laminar, with projections in both IPL and GCL (arrow, GCL arbor). IPL projections were underdeveloped relative to controls, and not sufficient to generate a clear sublayer (Fig. 5A). C: P3 control and mutant ON SACs, both of which project to the GCL. The control cell sends a single arbor to the GCL (left, arrow), typical of those few SACs that still project to the soma layers at this age. The mutant cell (right) makes a dense dendritic arborization in the GCL (right, arrow), which was never seen in P3 controls.

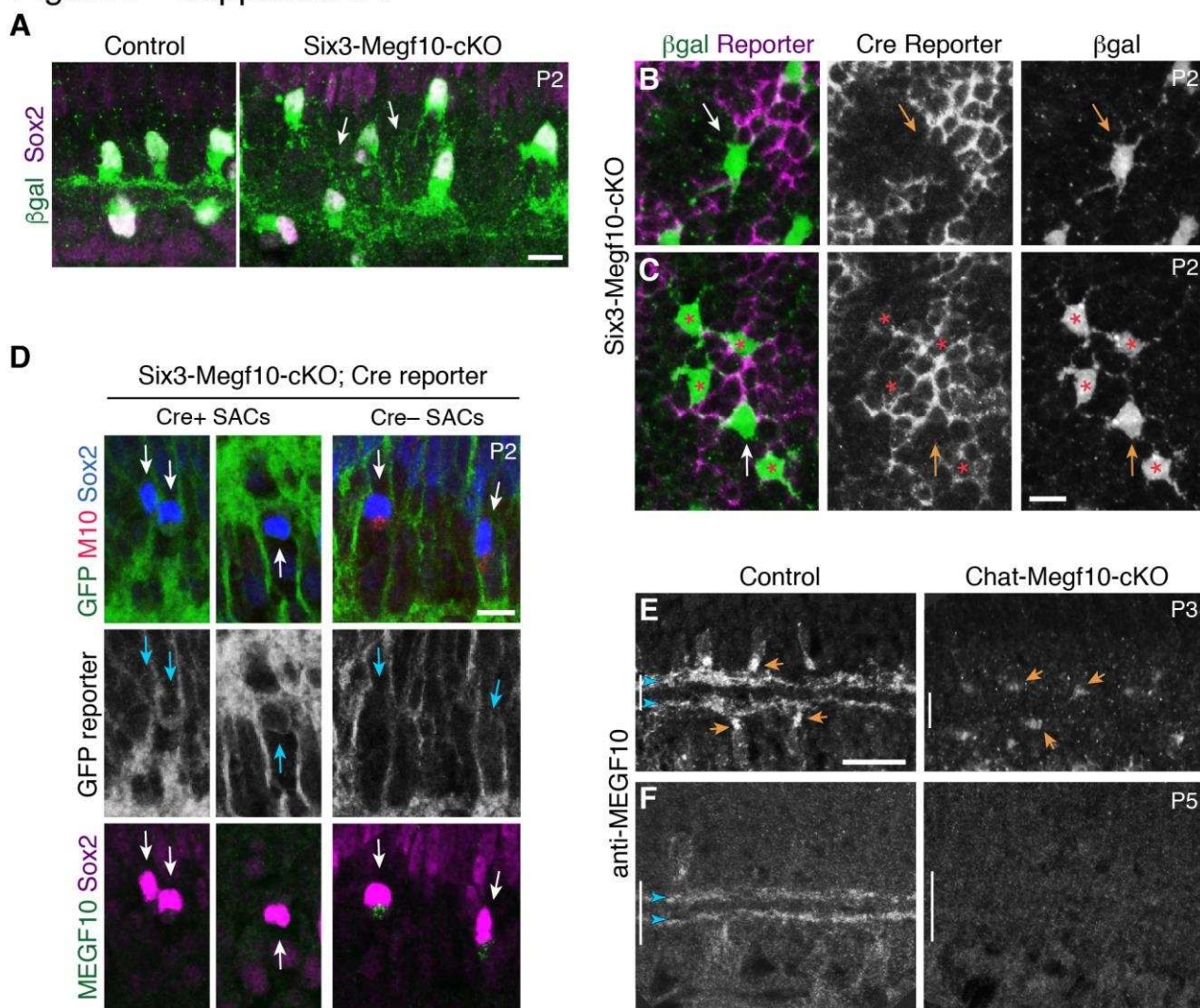
Scale bars: 10 μm.

**Figure 5-Supplement 1:**  
*Gad1-GFP*<sup>+</sup> amacrine cells show normal dendrite projections in *Megf10* mutants.

**A:** Retinal cross-sections from P1 mice carrying *Gad1-GFP* transgene. GFP labels a large subset of amacrine cells in INL. *Sox2*<sup>+</sup> SACs do not express GFP. Therefore, the GFP<sup>+</sup> cells constitute a broad non-SAC amacrine population.

**B;** Retinal cross-sections from P1 *Megf10* mutants and littermate (*Megf10*<sup>+/-</sup>)

## Figure 7 - Supplement 1

**Figure 7-Supplement 1: *Megf10* cell autonomy: Characterization of conditional mutant mice**

**A:** Six3-Megf10-cKO mice phenocopy SAC sublayer formation errors seen in null mutants. Cross-sections through central retina of P2 Six3-Megf10-cKO and littermate control mice. Immunostaining for *Megf10*: βgal and Sox2 revealed SAC morphology. Control SACs (left) have formed IPL sublayers by P2 and they rarely project to soma layers. In Six3-Megf10-cKO mice (right), sublayers are absent and SACs project exuberantly to soma layers (arrows).

**B:** The same Six3-Megf10-cKO Cre-negative SAC from Fig. 6B (arrow). βgal and GFP (Cre reporter) channels are shown separately (middle, bottom) to demonstrate lack of GFP expression in this cell.

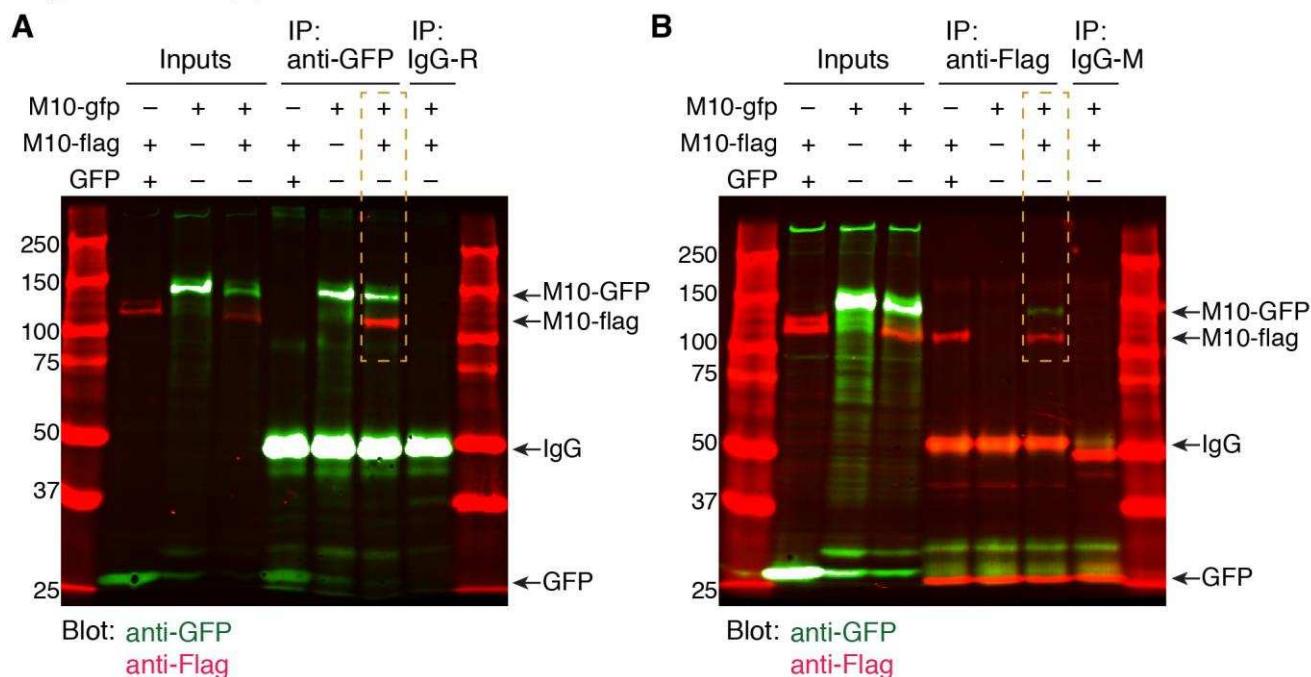
**C:** Another example of a Cre reporter-negative Six3-Megf10-cKO SAC (arrow) surrounded by mutant Cre-positive cells (asterisks). All 5 cells, including the unrecombined one, participate in an aberrant INL dendritic network (bottom).

**D:** GFP Cre reporter is a reliable proxy for MEGF10 protein expression status in Six3-Megf10-cKO mice. Cre<sup>+</sup> SACs (left, center panels) express the GFP reporter and lack MEGF10 immunoreactivity. Cre<sup>-</sup> SACs lack GFP reporter expression and retain MEGF10 immunoreactivity. Arrows, Sox2<sup>+</sup> SACs (or their position).

**E,F:** Timing of MEGF10 protein loss in Chat-Megf10-cKO mice. At P3 (E), MEGF10 immunoreactivity is much lower in mutants (right) than in littermate controls (*Chat*<sup>Cre</sup>; *Megf10*<sup>flox/+</sup>, left), but most SACs still express

some protein (arrows indicate examples of MEGF10-positive cells). At P5 (F), MEGF10 immunoreactivity is virtually absent in mutants but readily detectable in controls. Arrowheads, SAC IPL strata. Vertical bar, IPL. Scale bars: 10  $\mu\text{m}$  (A-D); 25  $\mu\text{m}$  (E,F). Scale bar in C applies to B, and bar in E applies to F.

Figure 7 - Supplement 2

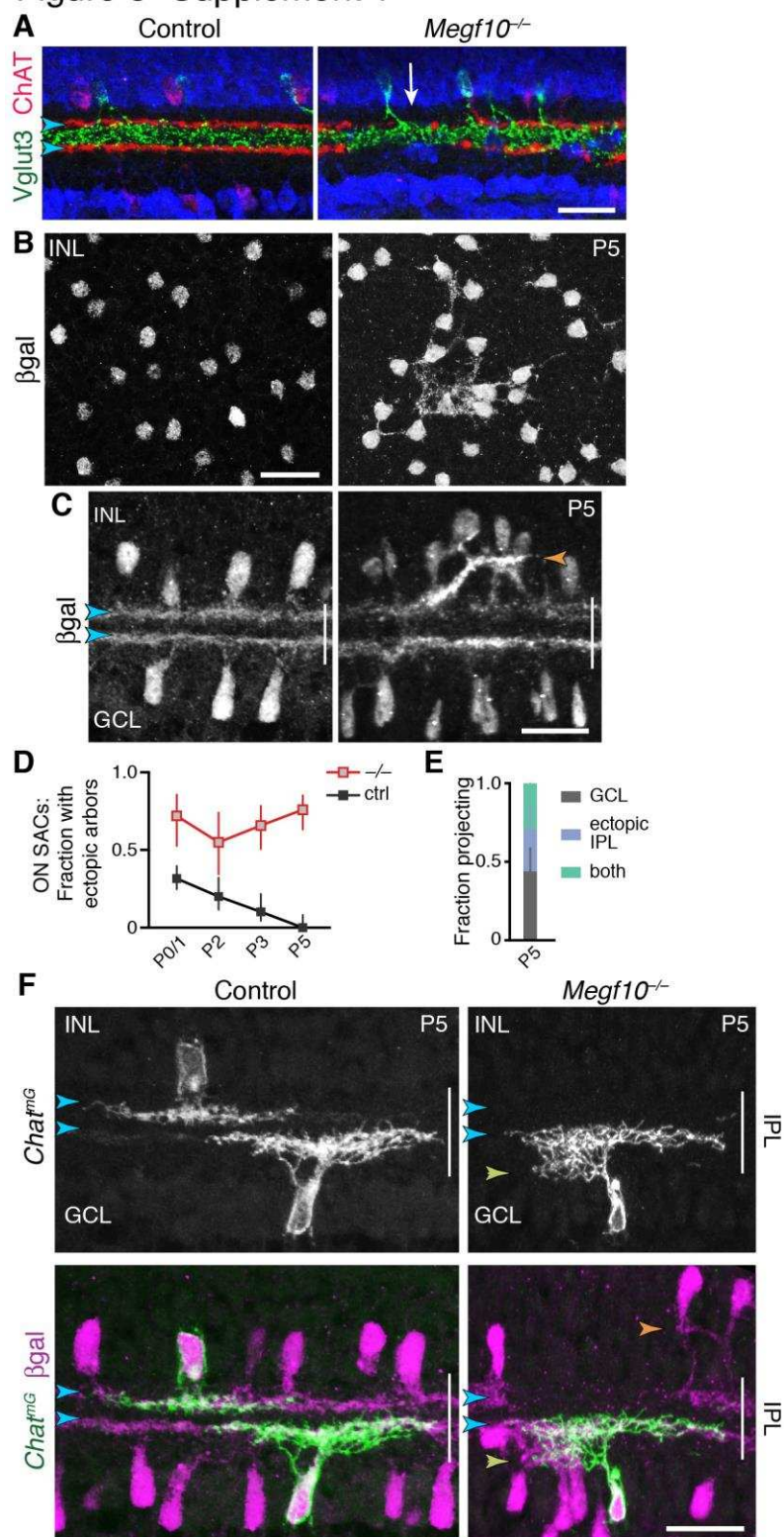


**Figure 7-Supplement 2: MEGF10 co-immunoprecipitation experiments**

**A:** Uncropped blot image for co-IP experiment depicted in Fig. 6J. Anti-GFP was used for pull-down. Blot was stained for anti-GFP (green) and anti-Flag (red). Orange box indicates the condition in which cells were transfected with both MEGF10- $\Delta$ ICD constructs. In this condition, pull-down with anti-GFP precipitated both MEGF10- $\Delta$ ICD-GFP and MEGF10- $\Delta$ ICD-Flag constructs, demonstrating that they interact. Ladder markings in kDa. Expected sizes for MEGF10- $\Delta$ ICD constructs, GFP, and IgG are indicated (arrows). R, rabbit IgG control. See Fig. 6I for illustration of in MEGF10- $\Delta$ ICD construct design.

**B:** Independent replicate of MEGF10- $\Delta$ ICD co-IP experiment, using anti-Flag for pull-down. Labels as in F. IP with anti-Flag co-precipitated both GFP and Flag-tagged MEGF10- $\Delta$ ICD constructs (orange box). Mouse (M) IgG control did not precipitate MEGF10 constructs, and MEGF10- $\Delta$ ICD-Flag did not co-precipitate with GFP alone.

## Figure 8- Supplement 1

**Figure 8-Supplement 1: SAC phenotypes in *Megf10* mutants at P5 and at maturity.**

**A:** Specificity of *Megf10<sup>-/-</sup>* SAC IPL innervation phenotype. The same cross-sections from Fig. 8A are shown here, overlaid with anti-Vglut3 staining (green) to label amacrine cells that project to an IPL sublayer between the SAC strata (arrowheads). Regions of mutant IPL not innervated by SACs (arrow) are still innervated by Vglut3<sup>+</sup> amacrine cells, demonstrating that absence of ChAT<sup>+</sup> arbors is not due to histology artifact and that impaired IPL innervation is a SAC-specific phenotype.

**B,C:** Anatomy of mutant SAC ectopic network at P5 provides further evidence that it shifts from INL to IPL. *Megf10*: $\beta$ gal staining seen *en face* at level of INL (B), and in cross-section (C). Mutant SAC arbors are aggregated and fascicular by P5; this contrasts with P3 when exuberant INL arbors are more diffuse (Fig. 6). Unlike later stages (Fig. 8A), when fascicles are only found in IPL, P5 fascicles could be located in the INL (B). Some arbor fascicles crossed the INL-IPL boundary at P5 (C, orange arrowhead). This was not seen at earlier or later ages (Fig. 6A; Fig. 8A), suggesting P5 is a transitional age in the INL-to-IPL shift.

**D,E:** ON SAC ectopic projections transition to the IPL at P5 in *Megf10* mutants, similar to OFF SAC projections (Fig. 8F,G). Frequency of mutant ectopic ON SAC projections does not decline over development (D), even though arbor anatomy changes by P5 (E). P0-3 data in D replotted from Fig. 6E, with both control groups combined. E: As with mutant OFF SACs, ON SACs can make ectopic projection errors either within the GCL or the IPL at P5.

**F:** *Megf10* mutant ON SAC phenotype at P5, revealed using *Chat<sup>mG</sup>* to label single cells and

*Megf10*: $\beta$ gal to label the full SAC population. Control SACs (left panels) are monostratified within the DS circuit IPL sublayers (blue arrowheads). Right: Example of a mutant ON SAC that makes an ectopic projection to inappropriate IPL sublayer (yellow arrowhead) while also projecting to the expected DS circuit sublayer (blue arrowheads). OFF SACs in this same field of view make ectopic projections within the INL (orange arrowhead), illustrating the simultaneous soma-layer and IPL ectopias observed only at P5.

Scale bars: 25  $\mu$ m.

## Figure 9 - Supplement 1

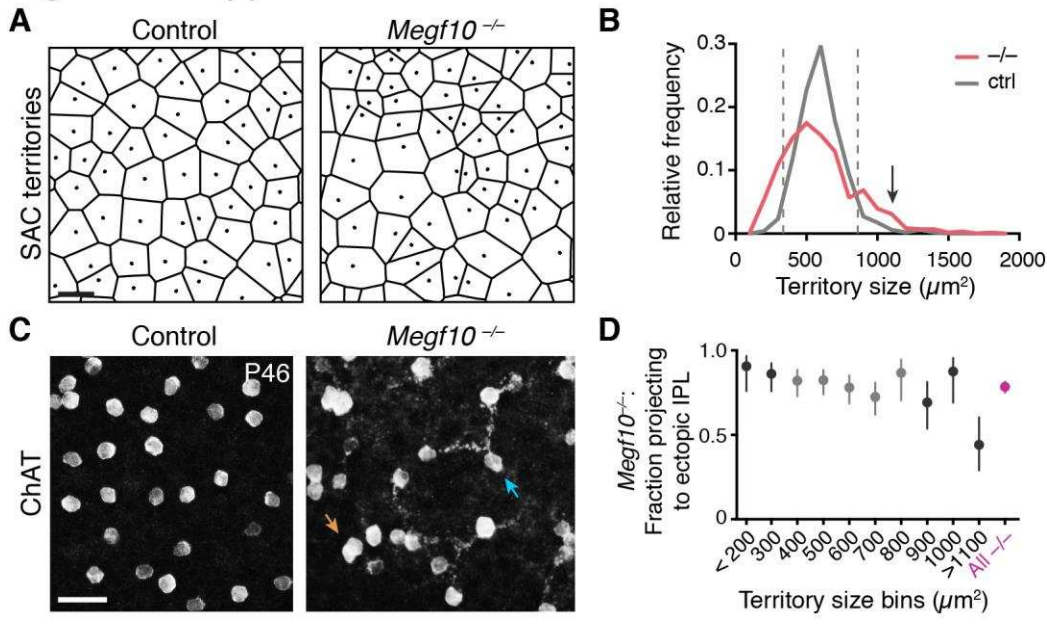


**Figure 9-Supplement 1:**  
Severity of *Megf10<sup>-/-</sup>* SAC mosaic phenotype does not correlate with IPL targeting error rate.

**A,B:** Strategy for quantifying severity of mosaic phenotype on single-cell level. The Voronoi domain (A; see Methods) is determined by the position of a cell relative to all its neighbors and therefore serves as a useful single-cell measure of local cell positioning (see Methods).

243 In control retina, the position of SACs relative to their neighbors is constrained by local cell-cell repulsion. This  
 244 can be seen in the uniform size distribution of their Voronoi territories: A, representative Voronoi domain  
 245 images (dots, cell body positions); B, histogram of SAC territory (i.e. Voronoi domain) sizes. Control  
 246 distribution (gray line) has a sharp peak.

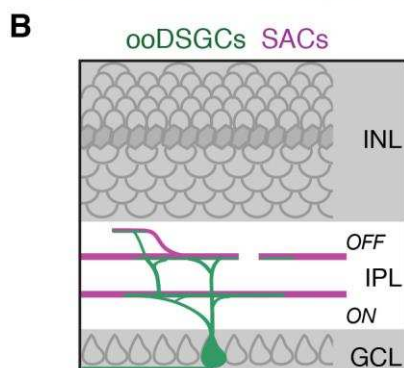
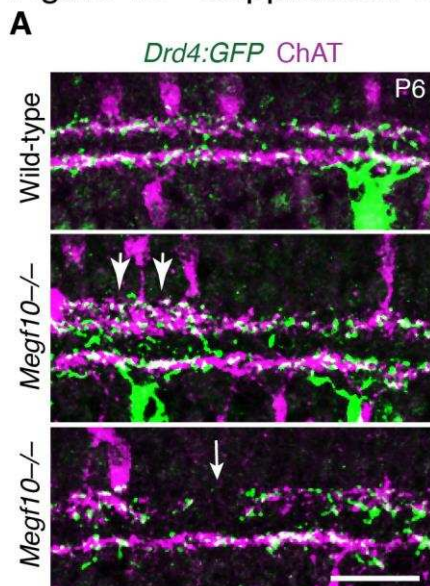
247 In *Megf10* mutants, the arrangement of SAC cell bodies is random; as a result, there are many mutant cells that,  
 248 by chance, are positioned quite normally relative to their neighbors, while other SACs are abnormally near or  
 249 far. This population-level phenotype manifests as a broader distribution of SAC territory sizes (B, red line). For  
 250 individual mutant SACs, their position along this size distribution curve can be used as a measure of mosaic  
 251 phenotype severity. Dashed lines (B), upper and lower 95% tolerance intervals of the control distribution.  
 252 Mutant cells outside these lines experience crowding or isolation rarely seen in control retina. Arrow in B  
 253 denotes largest bin in D. Bin size =  $100 \mu\text{m}^2$ . Sample sizes:  $n = 515$  cells from 2 littermate control (*Megf10<sup>+/-</sup>*)  
 254 mice;  $n = 584$  cells from 2 *Megf10<sup>-/-</sup>* mice.

255 **C:** No obvious correlation between a mutant cell's local neighborhood density and its projection to ectopic IPL  
 256 network. *En-face* view of SAC cell bodies and outer IPL, generated by Z-projecting part of a confocal stack  
 257 corresponding to these layers (Z distances: left,  $4.4 \mu\text{m}$ , right  $4.0 \mu\text{m}$ ). Controls lack SAC dendrites at this IPL  
 258 level. Arrows, examples of cells that are unusually far from their neighbors yet join the ectopic network (blue  
 259 arrow), or that are unusually crowded yet do not join (orange arrow).

260 **D:** Frequency of ectopic IPL projections for mutant SACs in each  $100 \mu\text{m}$  bin of histogram in D. Dark shading,  
 261 bins outside dashed lines in D. Smallest and largest bins were pooled to ensure adequate sample size ( $n \geq 24$   
 262 SACs per bin; see Methods for bin sizes). Across all bins except the largest one (denoted in B by arrow), error  
 263 rate was similar to the overall mutant error rate (red). Even in this last bin, SACs still made errors about 50% of  
 264 the time. These results demonstrate that ectopic IPL lamination errors are largely independent of soma  
 265 positioning errors. X values denote bin center (aside from pooled bins  $<200 \mu\text{m}^2$  and  $>1100 \mu\text{m}^2$ ). Error bars,  
 266 95% confidence intervals.

267 Scale bars,  $25 \mu\text{m}$ .

## Figure 10 - Supplement 1

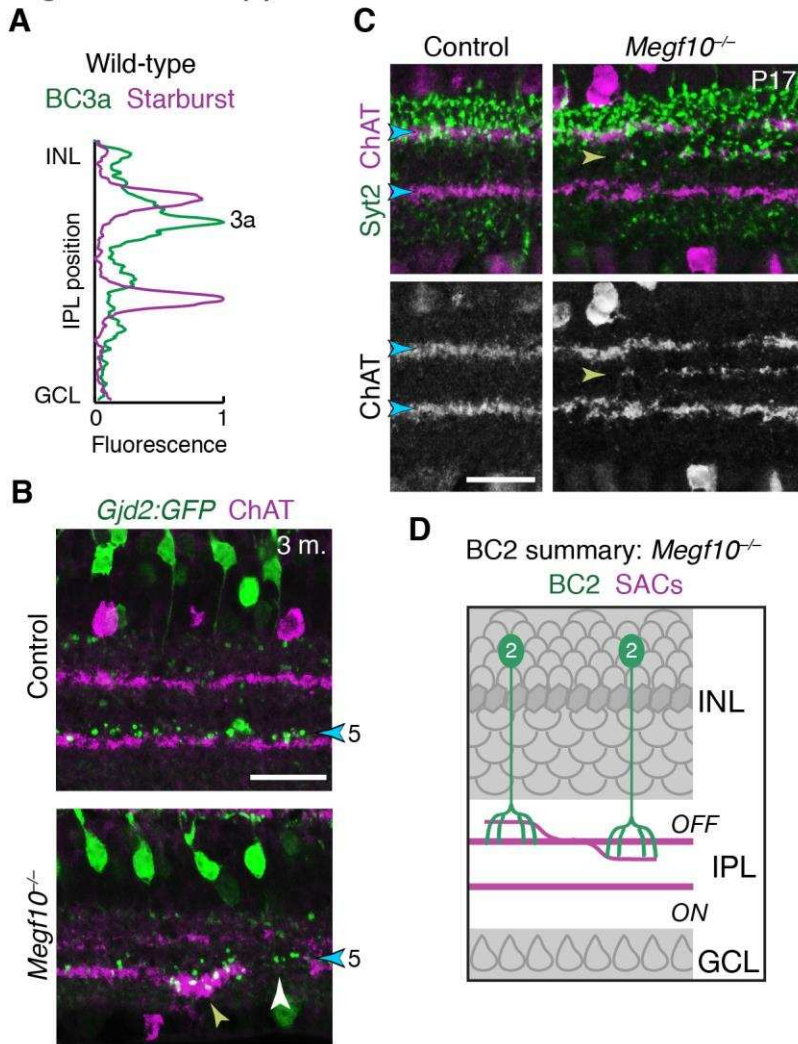
**Figure 10-Supplement 1: IPL innervation by ooDSGCs in *Megf10* mutants.**

**A:** *Drd4-GFP* mouse line was used to label a subset of ooDSGCs that is mutually exclusive with *Hb9-GFP*. IPL laminar targeting by *Drd4-GFP*<sup>+</sup> ooDSGCs was assessed in cross-sections of *Megf10*<sup>-/-</sup> and littermate control retinas, co-stained for ChAT to reveal SAC dendrites. In mutants, *Drd4-GFP*<sup>+</sup> cells made the same laminar targeting errors observed in the *Hb9-GFP* line (Fig. 10): When SACs projected to inappropriate laminar locations, ooDSGC dendrites were recruited to join them (center panel, large arrows). *GFP*<sup>+</sup> dendrites also failed to enter IPL regions not innervated by SACs (bottom panel, white arrow).

**B:** Summary of ooDSGC laminar targeting errors in *Megf10* mutants. Dendrites of ooDSGCs go to ectopic IPL locations when SACs do so, and fail to enter SAC IPL gaps.

Scale bar: 25  $\mu$ m

## Figure 11 - Supplement 1

**Figure 11-Supplement 1: IPL innervation by DS circuit bipolar cells in *Megf10* mutants.**

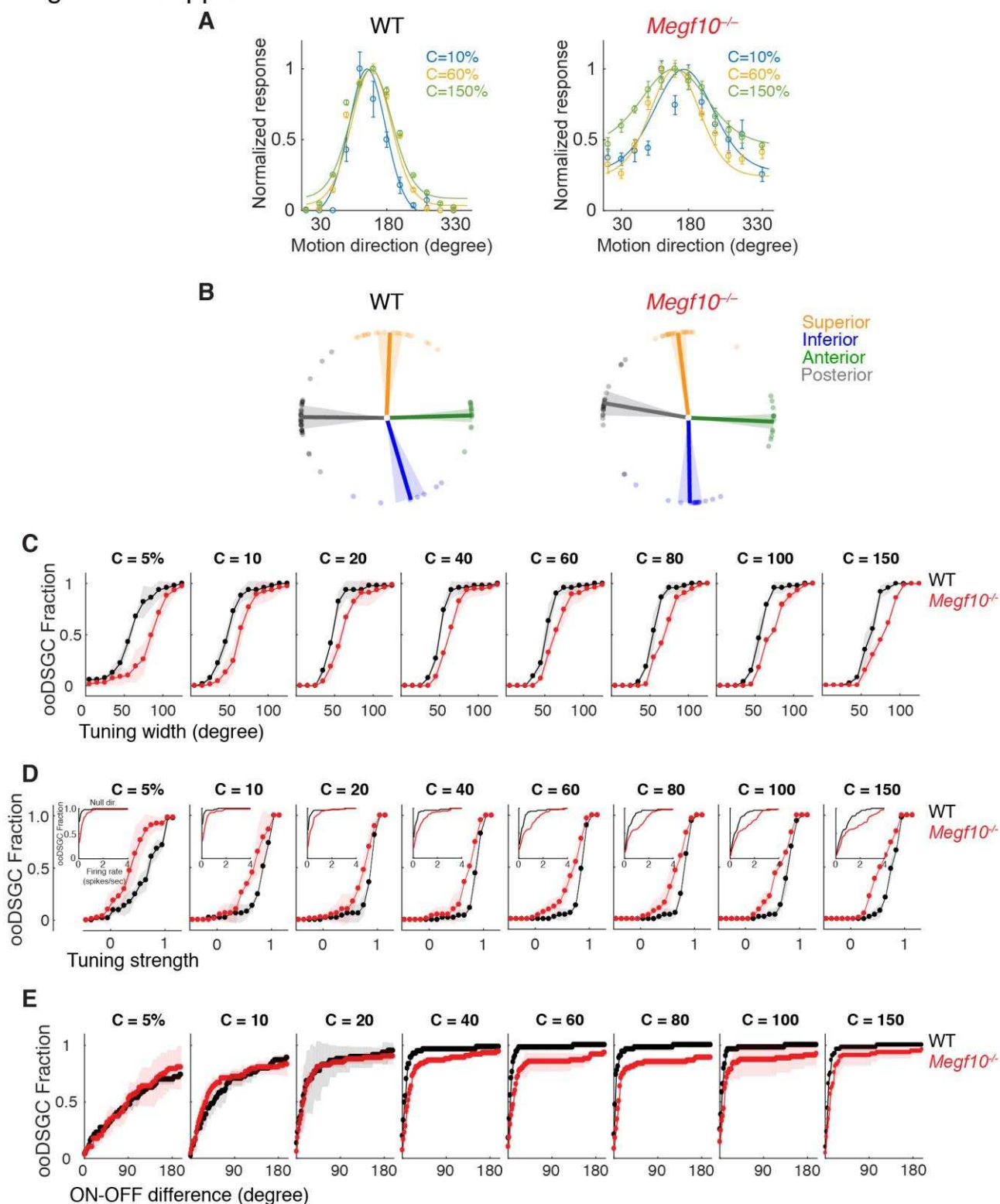
**A:** Fluorescence intensity plot across IPL obtained from a wild-type image similar to Fig. 11B – i.e. tissue stained with anti-ChAT (purple) and the BC3a marker HCN4 (green). BC3a arbors are excluded from the OFF SAC sublayer and arborize adjacent to it, similar to the behavior of BC5 and BC7 (Fig. 11D).

**B:** *Gjd2-GFP* mouse line was used as an independent marker of BC5 bipolar cells. In cross-sections of adult retinas stained for anti-GFP (green) and anti-ChAT (red), GFP was found to label BC5 neurons arborizing in their characteristic position adjacent to the ON SAC sublayer (blue arrowhead). Thus, unlike the *Kcng4<sup>mG</sup>* line in which both BC5 and BC7 were labeled, this line could be used to specifically assess BC5 phenotypes. In *Megf10* mutants, an ectopic SAC projection near the GCL border (yellow arrowhead) recruited BC5 terminals to an inappropriate IPL location. BC5 terminals are also seen innervating a gap in the SAC sublayer (white arrowhead). These phenotypes are similar to observations in *Kcng4<sup>mG</sup>* mice (Fig 11C-E).

2310 **C,D:** Laminar targeting errors by BC2 bipolar

311 cells in *Megf10* mutants. In control retina, BC2 axon terminals (stained with anti-Syt2, green) fill the entire IPL  
312 region between the INL border and the OFF SAC layer. This is the same region in which OFF SAC  
313 misprojection errors typically were found in mutants (e.g. Fig. 9A); therefore, most mutant errors did not probe  
314 whether BC2 axons could be recruited to new IPL regions. However, we did find a small number of cases, such  
315 as the one shown here, in which OFF SACs project inappropriately to central IPL regions where BC2 terminals  
316 are not normally found (yellow arrowhead). In these cases BC2 arbors are recruited to join SAC arbors in their  
317 abnormal laminar location. Thus, BC2 IPL projections are likely guided by similar SAC-derived cues as the  
318 other DS circuit-projecting bipolar cell types. D, summary of the BC2 projection phenotype in *Megf10* mutants,  
319 showing SAC errors that occurred within the normal BC2 domain (left) as well as those that recruited BC2  
320 arbors to new laminar positions. Scale bars: 25  $\mu$ m.

Figure 12-Supplement 1

**Figure 12-Supplement 1: Contrast-dependence of direction-tuning phenotypes in *Megf10*<sup>-/-</sup> ooDSGCs.**

**A:** Tuning curves from representative wild-type (WT) and *Megf10* mutant ooDSGCs measured at 3 contrasts (10, 60 & 150% Weber contrast). Circles show responses, solid lines show von Mises fits. Mutant tuning curves are broader than controls at all three contrasts.

**B:** Preferred directions of WT ooDSGCs (left) align to the four cardinal ocular axes: superior, inferior, anterior and posterior (Oyster and Barlow, 1967). K-means clustering was used to separate the recorded ooDSGC

328 population into these four subtypes (see Methods). Population mean (solid line) and standard deviation  
329 (shaded region) of preferred directions for each subtype is plotted; circles denote preferred direction of  
330 individual ooDSGCs. Preferred directions of *Megf10*<sup>-/-</sup> ooDSGCs (right) were also aligned to the cardinal axes,  
331 and there was no appreciable change in the fraction of ooDSGCs populating each subtype.

332 **C-E:** Cumulative distributions of tuning width (quantified by circular standard deviation; C), tuning strength  
333 (D), and ON-OFF preferred direction difference (E), measured at different bar contrasts (identified at the top of  
334 each plot) for WT and *Megf10*<sup>-/-</sup> ooDSGC populations. Insets (D) show responses to null direction stimuli. The  
335 analyzed RGC populations were the same as for data shown in Fig. 10 ( $n = 80$  WT and 74 mutant ooDSGCs,  
336 two retinas each genotype). The width and speed of the moving bar was 1200  $\mu\text{m}$  and 550  $\mu\text{m}/\text{sec}$ , respectively.  
337 Error bars/bands, S.E.M.

338

339